

**QUANTUM INFORMATION EXCHANGE
BETWEEN PHOTONS AND ATOMS**

WANG YIMIN

A THESIS SUBMITTED FOR

THE DEGREE OF DOCTOR OF PHILOSOPHY

**CENTRE FOR QUANTUM TECHNOLOGIES
NATIONAL UNIVERSITY OF SINGAPORE**

2013

*To my parents, my friends,
for all your love, care and encouragement.*

DECLARATION

I hereby declare that this thesis is my original work and it has been written by me in its entirety. I have duly acknowledged all the sources of information which have been used in the thesis.

This thesis has also not been submitted for any degree in any university previously.

Wang Yimin

WANG YIMIN

20 MARCH 2013

Acknowledgements

Working on the PhD in quantum physics has been a wonderful and often overwhelming experience to me. It would not have been possible to write this doctoral thesis without the help and support of the kind people around me. I own my thanks to many people for making my PhD an unforgettable experience.

First and foremost, I would like to express my sincere gratitude to my supervisor Prof. Valerio Scarani for his continuous advice throughout my four-year PhD study life; for guidance in my study and research; for his encouragement when I was frustrated; for his support on conference and research visits.

Besides my supervisor, I would like to thank the rest of The Academic Committee of my thesis work: Prof. Christian Kurtsiefer, Prof. Kwek Leong Chuan, and Prof. Chung Keng Yeow, for their insightful comments, and valuable questions.

I am very grateful to my colleagues Colin Teo, Jiří Minář, Gleb Maslennikov, Syed Abdullah Aljunid for their stimulating discussions, motivating comments and all the other help.

My special thanks also extend to the rest of my colleagues in ConneQt: Lana Sheridan, Daniel Cavalcanti, Jean-Daniel Bancal, Cai Yu, Yang Tzyh Haur, Rafael Rabelo, Melvyn Ho, Le Phuc Thinh, Law Yun Zhi, Wu Xing Yao, Le Huy Nguyen, Haw Jing Yan, Charles Lim. Thank you all for making my scientific journey productive and enjoyable.

I am also in gratitude to Prof. Li Chengzu, Prof. Chen Pingxing, Prof. Liang Linmei in my home university in China for enlightening me the first glance of research in quantum physics.

My sincere thanks also goes to my dear friends: Evon Tan, Han Rui, Wu Chunfeng, Li Wenhui for their care and precious friendship during my PhD life. I will never forget the nice

time when we had together. In particular, I am grateful to Evon Tan for helping me with all the administration to assist my PhD study.

I would also like to thank all the members of Centre for Quantum Technologies (CQT) as well as acknowledge support from CQT, for providing the right environment for science.

Finally, I take this opportunity to express the profound gratitude to my beloved parents, my brother and my boyfriend for their love and continuous support in my life.

Abstract

Quantum information processing tasks have been implemented in various physical platforms. In this thesis, we consider two specific implementations: Part **I** presents a detailed study of the interaction of a single atom with a light pulse. Part **II** examines the case of a quantum controlled-phase gate in circuit quantum electrodynamics in the ultrastrong coupling regime. They are both actively pursued by many research groups.

In Part **I**, we first present the framework for a single two-level atom interacting with the quantized electromagnetic field. The effect of temporal and spectral properties of the pulses on atomic excitation is studied for both Fock state and coherent state pulse. The detailed analysis of atomic excited state population is provided for single photon pulse with various temporal shapes.

The work is then extended to a more general case with two spatial-modes and multi-photon pulses. The difference between Fock state and coherent state pulse on atomic excitation is further investigated. We find that at few photon levels, the maximum atomic excitation probability is a monotonic function of photon number for the coherent state pulse, but not for the Fock state pulse. Furthermore, we show that the atomic dynamics can be controlled by the initial relative phase between the two counter-propagating coherent state pulses incident on the atom, which is not the case with two Fock state pulses.

The theoretical prediction is then compared with an experiment, where a single trapped ^{87}Rb atom interacts with coherent state pulses engineered in temporal shape of rising exponential and rectangular form.

Next, we propose a quantum memory setup based on a single two-level atom in a half cavity with a moving mirror. The efficiency of the quantum storage process is studied analytically and

we show that various temporal shapes of incident photon can be stored and read out with perfect efficiency by an appropriate motion of the mirror.

In Part II, we first give an overview of different coupling regimes in cavity & circuit quantum electrodynamics with rotating wave approximation and beyond. By taking into account the two counter-rotating terms in the Rabi Hamiltonian, we then investigate theoretically the performance of conventional two-qubit quantum gate schemes in the crossover from the strong to the ultrastrong coupling regime of light-matter interaction. Numerical results show that the fidelities of the gate operations are dropping down and novel schemes are required in order to implement quantum gates when increasing the normalized coupling strength.

We therefore propose an ultrafast quantum controlled phase gate scheme, which includes a suitable qubit-resonator ultrastrong interacting architecture and a gate operating on a time scale proportional to the inverse of the resonator frequency. Numerical simulation shows that this quantum gate can perform on subnanosecond time scales while keeping a fidelity of the gate operation above 99.5%.

Contents

Acknowledgements	iii
Abstract	v
1 Introduction	1
1.1 Quantum information processing (QIP)	1
1.1.1 Quantum computation	1
1.1.2 Quantum communication	2
1.1.3 Quantum network	3
1.2 Requirements and physical realizations for QIP	5
1.2.1 Quantum optics approach to QIP	6
1.2.2 Circuit QED approach to QIP	7
1.3 Overview of the thesis	8
I Atom-pulse interaction	11
2 Continuous-mode quantum optics	12
2.1 Three-dimensional continuous-mode quantum field	12
2.1.1 Continuous-mode field operators	13
2.1.2 Fock state wave-packets	14

2.1.3	Coherent state wave-packets	16
2.2	Two different mode one-dimensional wave-packets	17
2.2.1	Two-mode Fock state wave-packets	20
2.2.2	Two-mode coherent state wave-packets	20
2.3	The quantized atom-field interaction	20
2.3.1	The two-level atom	20
2.3.2	Interaction with a single two-level atom	22
2.4	Spontaneous emission in free space	22
3	Excitation of an atom by propagating pulses	28
3.1	Quantum Heisenberg-Langevin approach	28
3.2	Atomic state population	30
3.2.1	Revisit the atomic spontaneous emission	31
3.2.2	Atomic excitation with single-photon Fock state wave-packet	32
3.2.3	Atomic excitation with single-photon coherent state wave-packet	33
3.3	Numerical analysis of the temporal envelope	33
3.3.1	Special case: dipole pattern	33
3.3.2	Pulse bandwidth effects	34
3.3.3	Pulse shape effects	36
3.3.4	Damped Rabi oscillation	38
3.3.5	Discussion of realistic focusing	39
4	State-dependent atomic excitation by multi-photon pulses propagating along two spatial modes	40
4.1	Physical model	40
4.2	Atomic excitation by different pulses	42
4.2.1	Atomic excitation with Fock state pulses	42
4.2.2	Atomic excitation with coherent state pulses	45
4.2.3	Even- and odd-parity modes	46
4.3	Numerical simulation for different photon states	47
4.3.1	Single-photon excitation	48

4.3.2	Multi-photon excitation	50
4.3.3	Interference of pulses in two distinct spatial-modes	52
4.4	Experimental demonstration of atomic excitation with temporally shaped pulses	56
4.4.1	The experimental setup	56
4.4.2	The results	58
5	Quantum memory with a single two-level atom in a half cavity	63
5.1	The quantum memory model	63
5.1.1	General optical Bloch equations	63
5.1.2	Characteristics of the quantum memory setup	65
5.1.3	Write process: Absorption	67
5.1.4	Read process: Re-emission	69
5.2	Simulation with time-bin qubit	72
5.3	Implementations	74
II	Ultrafast gate in circuit QED	77
6	Quantum Electrical Circuits	78
6.1	Fundamental circuit elements	79
6.1.1	Capacitance	79
6.1.2	Inductance	79
6.2	Flux quantization and Josephson effect	80
6.2.1	Flux quantization	81
6.2.2	Josephson effect	81
6.3	Quantization of electrical circuits	85
6.3.1	The capacitance-matrix method	86
7	Strong coupling in QED: The rotating wave approximation and beyond	87
7.1	Cavity quantum electrodynamics	87
7.1.1	The general atom-cavity model	88
7.1.2	Rotating wave approximation and Jaynes-Cummings Model	89

7.2	Circuit quantum electrodynamics	91
7.2.1	Superconducting qubits as artificial atoms	91
7.2.2	Circuit QED with flux qubit	91
7.3	Different coupling regimes in cavity & circuit QED	93
7.3.1	The two dissipative processes	93
7.3.2	Weak coupling regime: The Purcell effect	95
7.3.3	Strong coupling regime: Damped Rabi oscillations	96
7.3.4	Beyond rotating wave approximation: The Rabi model	98
7.4	Validity of controlled-phase gates in the ultrastrong coupling regime	99
7.4.1	Two-qubit controlled-phase (CPHASE) gate	100
7.4.2	Analysis of the CPHASE gate performance for scheme I	100
7.4.3	Analysis of the CPHASE gate performance for scheme II	103
7.4.4	Discussion	105
8	Ultrafast Quantum Gates in Circuit QED	106
8.1	The design of a versatile flux qubit	106
8.1.1	The potential energy of the qubit	107
8.1.2	The kinetic energy of the qubit	109
8.2	The inhomogeneous transmission line resonator	109
8.2.1	The Lagrangian of the interrupted resonator	109
8.2.2	Normal modes decomposition	111
8.2.3	The enhanced phase biasing	112
8.2.4	Effect of boundary conditions	113
8.2.5	Quantization of transmission line resonator	115
8.2.6	Dispersion relation	116
8.3	The total qubit-resonator system	116
8.3.1	The Hamiltonian of the qubit-resonator system	117
8.3.2	Numerical analysis of the circuit	122
8.3.3	Characteristics of inhomogeneous transmission line resonator	122
8.3.4	Numerical simulation of the total Hamiltonian	124
8.4	The ultrafast two-qubit gate scheme	126

8.5 Discussion	129
9 Conclusion	131
Bibliography	134
List of Publications	151

Introduction

1.1 Quantum information processing (QIP)

Quantum information processing (QIP) is an interdisciplinary research field with the potential to cause revolutionary advances in the fields of computation and communication by exploiting information theory and computer science in physical systems governed by quantum mechanics. Quantum information processing has been a rapidly developing field in the past few decades and it can be formally split into two main areas — quantum computation and quantum communication. Quantum computation holds the promise of faster computation to solve certain difficult problems that can't be efficiently solved by classical computers [1]. Quantum communication has the potential to achieve secure long-distance communication [2]. Quantum network, which is composed of many quantum nodes that are connected through quantum channels, provides the bridge between quantum computation and quantum communication [3].

1.1.1 Quantum computation

The concept of quantum computation was originally put forward by R. P. Feynman in 1982 [4], who found that a computer running according to quantum mechanics could solve problems much faster than a classical one due to quantum parallelism. Later in 1985, D. Deutsch showed that any physical process can be in principle simulated by a universal quantum computer, which can be implemented by a universal set of quantum logic gates, which includes a series of single-qubit rotation gates and two-qubit controlled NOT gates [5]. Deutsch-Jozsa algorithm, which was

proposed in 1992, is the first example of a quantum algorithm that is exponentially faster than any possible deterministic classical algorithm [6]. Two years later, Peter Shor proposed a quantum algorithm to efficiently compute the prime factors of an integer [7]. In 1996, L. Grover proposed a quantum algorithm for searching an unsorted database with N entries in $\mathcal{O}(N^{1/2})$ time and using $\mathcal{O}(\log N)$ storage space [8], while classically the task scales as $\mathcal{O}(N)$.

It is clear that quantum computer performs certain algorithms exponentially faster than the conventional computers. The extra computational power comes from the two fundamental principles of quantum mechanics — *superposition and entanglement*. Superposition offers the possibility of processing many states in parallel. Entanglement coherently correlates several qubits and serves as a basis for multiple-qubit operations.

In a classical binary computer, the fundamental information unit is the classical binary bit usually denoted as 0 and 1. In a quantum computer, the information is encoded in qubits, or quantum bits. Any two-level quantum mechanical system can serve as a qubit, e.g., the electronic spin or the polarization state of light. The most distinguishing feature between a qubit and a classical bit is that the qubit can be in arbitrary superposition of the two states $|0\rangle$ and $|1\rangle$,

$$|\psi\rangle = \alpha |0\rangle + \beta |1\rangle, \quad \alpha, \beta \in \mathbb{C}, \quad |\alpha|^2 + |\beta|^2 = 1. \quad (1.1)$$

Quantum processors must be well isolated from the sources of noise in order to prevent decoherence. However, they inevitably interact with their surroundings, resulting in decoherence and hence in the decay of the quantum information stored in the device. Fortunately, quantum error correction that comes from the marriage of quantum mechanics with the classical theory of error correcting codes, provides us the tool to fight against decoherence and has been proved theoretically that it allows for quantum gate operations with near perfect accuracy and fidelity [1, 9, 10].

1.1.2 Quantum communication

Quantum communication is the art of transferring a quantum state from one location to another. Quantum cryptography or quantum key distribution (QKD) applies fundamental laws of quantum physics to guarantee secure long-distance quantum communication. It enables two legitimate users, commonly named Alice and Bob, to produce a shared secret random bit string, which can

be used as a key in cryptographic applications, such as message encryption and authentication. In contrast to conventional cryptography, whose security often relies on mathematical theory and computation power, QKD promises unconditional security based on the fundamental laws of quantum mechanics. The first quantum cryptography protocol was proposed by C. Bennett and G. Brassard in 1984 [11] and later in 1991, A. Ekert proposed another protocol based on entanglement [12]. Since then, tremendous progress has been made both theoretically [2] and experimentally [13–16]. The experimental record of quantum key distribution is 250 km for fiber-based quantum communication [15] and 144 km for free-space quantum communication [16], respectively.

1.1.3 Quantum network

Quantum network, which consists of many spatially separated nodes connected by quantum communication channels, plays an important role in the physical implementation of quantum communication protocols [3, 17, 18]. Quantum information is generated, processed and stored locally in quantum nodes. Information exchange between different nodes and entanglement distribution across the entire network is accomplished via quantum channels. Quantum network opens the possibility for more complex activities such as multi-party communication and distributed quantum computing.

A possible physical implementation of such a network could be done with the atoms(ions), which are linked by photons propagating e.g. in optical fibers, as shown in Fig.(1.1). The trapped atoms or ions represent the nodes, and optical fibers or free space provide the quantum channels. Atoms(ions), which have long coherence times, serve as “stationary qubits” in each node, where information is stored in the long-lived internal states and where one can perform

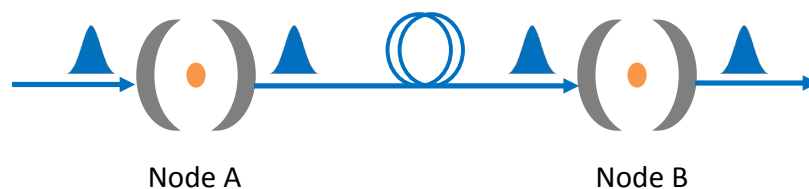


Figure 1.1: Sketch of quantum network: quantum state transfer from node A to node B is shown in the setting of cavity quantum electrodynamics.

local manipulations. Photons, as the elementary constituents of light, serve as “flying qubits” which are particularly well suited for fast and reliable communication over long distances.

Strong interaction between atoms(ions) and photons is thus of great interest and fundamental importance in quantum information sciences. Moreover, coherent control over the exchange between single quanta of light and matter remains as the main scientific challenge in the quest to distribute quantum states across a quantum network. In principle, the quality of quantum network is limited by the channel and the coupling loss (as well as source and detector inefficiencies), as those factors will degrade the quantum state that is being transmitted.

Quantum repeaters

The distribution of quantum states over long distances is essential for quantum information processing. In practice, the bottleneck for quantum communication between distant nodes is the scaling of the error probability with the length of the channel connecting the nodes. For example, for optical fibers the loss are typically 0.2 dB/km in the optimal wavelength range around 1.5 μm . Although the loss is remarkably low, it is finite, and scales exponentially with distance. Nevertheless, losses become very significant for communication over hundreds of kilometers or more. For classical communication, this problem is solved by repeated amplification of the light pulses that carry the information. Unfortunately, straightforward amplification is in general forbidden because of the no-cloning theorem [19] in quantum theory. Nevertheless, it turns out that the problem can be overcome using the so-called “quantum repeater” [20, 21]. The key idea of the quantum repeater is to distribute entanglement in each link and then swap between the

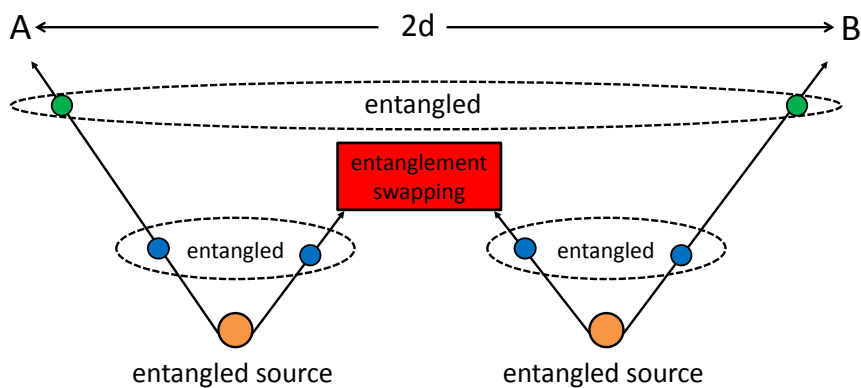


Figure 1.2: The concept of quantum repeater: distribution of entanglement over a long distance through local entanglement creation and successive entanglement swapping.

links, as shown in Fig.(1.2).

There are three essential requirements for the quantum repeater protocol.

- *Distribution of entanglement in the elementary link*: typically uses entangled photon pairs.
- *Quantum memories*: one has to be able to store the encoded information and the created entanglement in every elementary link.
- *Entanglement swapping*: one has to be able to perform local joint measurements to extend the range of the entanglement across the quantum repeater network.

The performance of a quantum repeater protocol is inherently limited by the time it takes to establish entanglement between nodes.

The well known DLCZ protocol is a highly influential proposal for realizing quantum repeaters [18], where the atomic ensembles are used as quantum memories, linear optical techniques in combination with photon counting to perform all the required operations. Many theoretical improvements [22–26] and experimental progresses [27–29] have been inspired by the DLCZ protocol. In addition to the atomic ensemble based quantum repeaters, remarkable achievements have been done in recent years with single atom system [30, 31], where elementary quantum network with single atom is demonstrated for the first time.

It is worth mentioning that, a very recent study presents an alternative approach to quantum communication that neither requires the establishment of entanglement between remote locations nor the use of long-lived quantum memories [32].

1.2 Requirements and physical realizations for QIP

In 2000, D. P. DiVincenzo listed out the five criteria for the implementation of quantum information processing [33]:

1. Scalable physical system with well characterised qubits.
2. Initialisation of the state of the qubits is possible.
3. Decoherence time of the qubit needs to be much longer than the gate operation time.
4. A universal set of quantum gates can be applied.

5. Qubit-selective measurement capability.

The above five requirements are sufficient for quantum computation tasks. However, two more criteria have to be fulfilled when long-distance quantum communication is required:

6. Ability to interconvert stationary and flying qubits.
7. Faithful and efficient transmission of flying qubits between specified locations.

Quantum information processing tasks can be implemented in various platforms. The typical information carriers are :

- *Optical and atomic-like systems:* photons [34, 35], trapped ions [36, 37], neutral atoms [3, 38], molecules [39];
- *Solid state systems:* superconducting qubits [40, 41], nitrogen-vacancy center [42], quantum dots [43], plasmon [44], spin qubit silicon [45–47];
- *Hybrid quantum systems:* a novel and promising approach for future quantum information hardware. It exploits particular features of various quantum platforms for enhanced quantum information capabilities [48–50]. Therefore, the hybrid quantum systems profit from the advantages of the individual systems: while some quantum systems, like atoms, are well suited for storing quantum information for extended periods of time, others, like solid state systems, exhibit strong interactions that allows one to implement fast quantum gates. Yet other quantum systems, like optical photons, are ideally suited for the transmission of quantum information over long-distance.

Motivated by recent experimental progress, in this thesis we will be particularly interested in the following two approaches to quantum information processing.

1.2.1 Quantum optics approach to QIP

Atom-light interaction at quantum level lies at the heart of quantum information science as well as being the fundamental process in quantum optics. The exchange of information between photons and atoms can be done by efficient absorption and emission of the photon by the atom [51–56].

Strong atom-light interaction has been realized at both many-atom and single-atom levels. In the first case, the interaction between the photon and the atoms is effectively enhanced due to a

high number of the atoms in the ensemble [18, 26]. On the other hand, it is still experimentally challenging to achieve strong and efficient coupling at a single atom - single photon level. There are two possibilities to achieve this goal:

- *Cavity quantum electrodynamics (cavity QED)*: a common approach to enhance the coupling strength is to place the atom into a high finesse cavity [57–59], where the electric field is dramatically increased by using optical cavities with small mode volumes.
- *High numerical aperture optics*: an alternative way is the recently developed free-space atom-light coupling approach, which uses the high numerical aperture optical elements to strongly focus the electric field to the single atom(ion) and thus give rise to reasonably strong interaction [60–62].

One of the main differences between the two approaches is that the photons are in the running wave in the free-space rather than in the standing wave as in cavity QED. The first part of this thesis (Part I) is triggered by and based on this free-space tight focusing configuration, and the interaction between the atom and propagating pulses is studied.

1.2.2 Circuit QED approach to QIP

The quantum electrodynamics of superconducting microwave circuits has been referred to as circuit quantum electrodynamics (circuit QED) by analogy to cavity QED in quantum optics, where the superconducting qubit acting as an artificial atom is electromagnetically coupled to a transmission line resonator acting as the cavity [63–65]. Those superconducting circuits based on Josephson junctions exhibit macroscopic quantum coherence and can behave like artificial atoms — controllable two-level systems. Different types of artificial atoms can be designed and fabricated depending on whether the Josephson energy E_J or the electrostatic Coulomb energy E_c dominates and determines the quantum mechanical behaviour of the Josephson junction circuit [40, 66]. The most common kinds of superconducting qubits are charge qubit [67], flux qubit [68] and phase qubit [69, 70]. Moreover, hybrid superconducting qubits are being investigated for long coherence time and better performance, such as transmon [71, 72] and fluxonium [73]. Whereas natural atoms are typically controlled using visible or microwave photons that transfer electrons from one state to another, the artificial atoms in these circuits are driven by currents, voltages and

microwave photons that excite the system from one quantum state to another.

Circuit QED is becoming arguably a prominent solid-state architecture for quantum information processing and considerable progresses have been achieved experimentally, such as: two-qubit gate and algorithms [74–78], three-qubit gate and entanglement generation [79–84], quantum error correction [85], as well as novel quantum phenomena in circuit QED such as dynamical Casimir effect [86], and the ultrastrong coupling regime of light-matter interaction [87–91].

In contrast to cavity QED with natural atoms, circuit QED offers many important advantages: the flexible tunability and controllability of the transition frequency and the coupling strength; the scalability with many qubits. Therefore, it serves as very promising candidate for quantum computation.

The second part of this thesis (Part II) is triggered by the experimental progress of achieving ultrastrong coupling regime in circuit QED [89, 90], and a realistic ultrafast two flux qubit quantum controlled-phase gate scheme is proposed.

1.3 Overview of the thesis

The thesis contains two main parts.

The first part (chapter 2, 3, 4, 5) analyses the interaction between a single two-level atom and propagating light pulses.

- In chapter 2, we present the basic theory of continuous-mode quantum optics — a general quantized model of the interaction between an atom and a propagating pulse in free space. This serves as a background for the first part of the thesis.
- In chapter 3, the dependence of the atomic excitation probability on the temporal and spectral features of propagating pulse is investigated theoretically. The quantum mechanical Heisenberg-Langevin formalism is introduced in Sec.(3.1) as a general tool to study atom and pulse interaction. The pulse temporal shape effect on single atomic excitation for both single photon Fock state and coherent state wave packets are theoretically analysed in Sec.(3.2), which is followed by numerical analysis in Sec.(3.3).
- In chapter 4, the dynamics of a more general case where a single two-level atom interacts with two spatial-modes multi-photon pulses is analysed. The theoretical model is described

in Sec.(4.1). The formalisms for atomic dynamics with two spatial-mode multi-photon pulses in Fock state and coherent state are given in Sec.(4.2) and numerical simulation for atomic dynamics with different photon states is done in Sec.(4.3). In Sec.(4.4), the theory is then compared to an experimental where a single ^{87}Rb atom interacts with the temporal shape controlled coherent state pulse in tight focusing configuration.

- In chapter 5, we propose a quantum memory setup based on a single two-level atom in a half cavity with a moving mirror. We show by explicit calculation in Sec.(5.1) that various temporal shapes of the input single photon pulse can be efficiently stored by the atom-mirror system, provided the motion of the mirror is optimized. We illustrate these results with an example of an input single photon time-bin qubit in Sec.(5.2) and discuss possible experimental realizations of the quantum memory scheme in Sec.(5.3).

The second part of the thesis (chapter 6, 7, 8) investigate the possibility of realizing an ultrafast gate in circuit QED.

- In chapter 6, a general introduction to the quantum mechanical description of electrical circuits is given.
- In chapter 7, we give a review of atom-photon interaction in cavity and circuit QED with the rotating wave approximation (RWA) and beyond. In Sec.(7.1), a general model is presented and followed by a discussion of the different coupling regimes, from weak coupling to strong coupling and up to ultrastrong and deep strong coupling regimes. The performance of two resonant controlled phase gate schemes, which are designed for the normal strong coupling regime is analyzed in ultrastrong coupling regime, where the rotating wave approximation breaks down. The experiment development of ultrastrong coupling techniques brings us the possibility of faster gate operations in circuit QED, but the dropped fidelity of those RWA-based gate schemes lead to the strong demand for new gate protocols, which is the motivation of our work in next chapter.
- In chapter 8, we propose a realistic ultrafast two-qubit quantum gate scheme, which includes a tunable ultrastrongly coupled qubit-resonator system (Sec.(8.3)) and a two-qubit controlled phase gate protocol that works in ultrastrong coupling regime (Sec.(8.4)).

Finally, the thesis ends with chapter 9 where the conclusion is presented.

Part I

Atom-pulse interaction

Continuous-mode quantum optics

A traditional use of discrete-mode quantum optics theory has been the description of quantum electrodynamics in a cavity, where the electromagnetic field is quantized in terms of a complete set of discrete eigenmodes with the appropriate boundary conditions applied. The well-known Jaynes-Cummings model, which describes the interaction between a single two-level atom with a single-mode in the cavity, is a popular example of the discrete-mode formalism. Although the discrete mode theory is quite suitable for cavity quantum electrodynamics experiments, a general process in free space requires continuous-mode description, such as photon detection in free space, travelling wave-packets.

2.1 Three-dimensional continuous-mode quantum field

Here, we present the quantized electromagnetic field theory in three-dimensional space with a set of eigenmodes characterized by a continuous wave vector and apply the continuous-mode quantum theory of the electromagnetic field to quantum electrodynamics.

2.1.1 Continuous-mode field operators

In Coulomb gauge, the electric and magnetic field can be expanded using monochromatic modes as [92, 93, p. 73],

$$\mathbf{E}(\mathbf{r}, t) = i \sum_{\lambda=1}^2 \int d^3 \mathbf{k} \sqrt{\frac{\hbar \omega_k}{(2\pi)^3 2\epsilon_0}} \boldsymbol{\epsilon}_{k,\lambda} \left[u_{k,\lambda}(\mathbf{r}) a_{k,\lambda} e^{-i\omega_k t} - u_{k,\lambda}^*(\mathbf{r}) a_{k,\lambda}^\dagger e^{i\omega_k t} \right], \quad (2.1)$$

$$\mathbf{B}(\mathbf{r}, t) = i \sum_{\lambda=1}^2 \int d^3 \mathbf{k} \sqrt{\frac{\hbar \omega_k}{(2\pi)^3 2\epsilon_0}} \left(\frac{\mathbf{k} \times \boldsymbol{\epsilon}_{k,\lambda}}{\omega_k} \right) \left[u_{k,\lambda}(\mathbf{r}) a_{k,\lambda} e^{-i\omega_k t} - u_{k,\lambda}^*(\mathbf{r}) a_{k,\lambda}^\dagger e^{i\omega_k t} \right], \quad (2.2)$$

where $\omega_k = c|\mathbf{k}| = ck$, c is the vacuum speed of light, ϵ_0 is the permittivity of the vacuum, $\boldsymbol{\epsilon}_k$ are unit polarization vectors satisfying,

$$\boldsymbol{\epsilon}_{k,\lambda} \cdot \boldsymbol{\epsilon}_{k,\lambda'} = \delta_{\lambda\lambda'}, \quad \boldsymbol{\epsilon}_{k,\lambda} \cdot \mathbf{k} = 0. \quad (2.3)$$

Energy conservation implies the normalization of the spatial mode functions $u_{k,\lambda}(\mathbf{r})$,

$$\int d^3 \mathbf{r} u_{k,\lambda}^*(\mathbf{r}) \cdot u_{k',\lambda'}(\mathbf{r}) = \delta(\mathbf{k} - \mathbf{k}') \delta_{\lambda\lambda'}. \quad (2.4)$$

For example, a popular and convenient mode decomposition basis for free-space field would be the monochromatic, plane-wave $u_{k,\lambda}(\mathbf{r}) = e^{i\mathbf{k}\cdot\mathbf{r}}$, which serves well for simple models.

The monochromatic annihilation $a_{k,\lambda}$ and creation operators $a_{k,\lambda}^\dagger$ obey the bosonic commutation relations

$$[a_{k,\lambda}, a_{k',\lambda'}^\dagger] = \delta(\mathbf{k} - \mathbf{k}') \delta_{\lambda\lambda'}, \quad (2.5)$$

$$[a_{k,\lambda}, a_{k',\lambda'}] = [a_{k,\lambda}^\dagger, a_{k',\lambda'}^\dagger] = 0. \quad (2.6)$$

The electromagnetic-field Hamiltonian operator is expressed as

$$H_f = \sum_{\lambda=1}^2 \int d^3 \mathbf{k} \hbar \omega_k a_{k,\lambda}^\dagger a_{k,\lambda}, \quad (2.7)$$

where the zero-point energy has been ignored. The corresponding wave-packet number operator

$$N = \sum_{\lambda=1}^2 \int d^3\mathbf{k} a_{\mathbf{k},\lambda}^\dagger a_{\mathbf{k},\lambda} \quad (2.8)$$

satisfies

$$[N, a_{\mathbf{k},\lambda}^\dagger] = a_{\mathbf{k},\lambda}^\dagger, \quad [N, a_{\mathbf{k},\lambda}] = -a_{\mathbf{k},\lambda}. \quad (2.9)$$

2.1.2 Fock state wave-packets

Any continuous-mode state that contains a finite number of photons must have the form of a pulse, or succession of pulses. Consider the photon wave-packet operator

$$A_p^\dagger = \sum_{\lambda=1}^2 \int d^3\mathbf{k} f_{\mathbf{k},\lambda} a_{\mathbf{k},\lambda}^\dagger, \quad (2.10)$$

with the normalized mode distribution function $f_{\mathbf{k},\lambda}$ satisfying

$$\sum_{\lambda=1}^2 \int d^3\mathbf{k} |f_{\mathbf{k},\lambda}|^2 = 1. \quad (2.11)$$

The commutator of the photon wave-packet operator satisfies the standard boson commutation relation, which can be obtained with the use of the Eqs.(2.5, 2.6)

$$[A_p, A_p^\dagger] = 1. \quad (2.12)$$

The continuous-mode photon Fock state can be defined as

$$|n_p\rangle = \frac{(A_p^\dagger)^n}{\sqrt{n!}} |0\rangle, \quad (2.13)$$

which has the properties that:

$$N |n_p\rangle = n |n_p\rangle, \quad (2.14)$$

$$A_p |n_p\rangle = \sqrt{n} |(n-1)_p\rangle, \quad (2.15)$$

$$A_p^\dagger |n_p\rangle = \sqrt{n+1} |(n+1)_p\rangle, \quad (2.16)$$

$$a_{\mathbf{k},\lambda} |n_p\rangle = \sqrt{n} f_{\mathbf{k},\lambda} |(n-1)_p\rangle, \quad (2.17)$$

and $\langle n_p | n_p \rangle = \langle 0 | 0 \rangle = 1$, where $|0\rangle$ is the continuous-mode vacuum state.

It is worth noting that, the continuous-mode photon Fock state $|n_p\rangle$ defined in Eq.(2.13) represents n independent photons in the same wave-packet, and it is **not** an eigenstate of the field Hamiltonian H as in the single mode case. For example, for single photon wave packet, we have

$$H |1_p\rangle = \sum_{\lambda=1}^2 \int d^3 \mathbf{k} \hbar \omega_{\mathbf{k}} f_{\mathbf{k},\lambda} a_{\mathbf{k},\lambda}^\dagger |0\rangle. \quad (2.18)$$

However, the expectation values of the electric field operator satisfies

$$\langle n_p | \mathbf{E}(\mathbf{r}, t) | n_p \rangle = 0, \quad (2.19)$$

which is identical to the property of the single mode Fock state.

The other useful commutators for the photon wave-packet operator are

$$[A_p, (A_p^\dagger)^n] = n (A_p^\dagger)^{n-1}, \quad [A_p^\dagger, A_p^n] = -n A_p^{n-1}, \quad (2.20)$$

$$[N, (A_p^\dagger)^n] = n (A_p^\dagger)^n, \quad [N, A_p^n] = -n A_p^n, \quad (2.21)$$

$$[a_{\mathbf{k},\lambda}, (A_p^\dagger)^n] = n f_{\mathbf{k},\lambda} (A_p^\dagger)^{n-1}, \quad [a_{\mathbf{k},\lambda}^\dagger, A_p^n] = -n f_{\mathbf{k},\lambda}^* A_p^{n-1}, \quad (2.22)$$

and for $F[A_p^\dagger]$ and $F[A_p]$ as functions of the wave-packet operators

$$[A_p, F[A_p^\dagger]] = \frac{d}{dA_p^\dagger} F[A_p^\dagger], \quad [A_p^\dagger, F[A_p]] = -\frac{d}{dA_p} F[A_p], \quad (2.23)$$

$$[N, F[A_p^\dagger]] = A_p^\dagger \frac{d}{dA_p^\dagger} F[A_p^\dagger], \quad [N, F[A_p]] = -A_p \frac{d}{dA_p} F[A_p], \quad (2.24)$$

$$[a_{k,\lambda}, F[A_p^\dagger]] = f_{k,\lambda} \frac{d}{dA_p^\dagger} F[A_p^\dagger], \quad [a_{k,\lambda}^\dagger, F[A_p]] = -f_{k,\lambda}^* \frac{d}{dA_p} F[A_p]. \quad (2.25)$$

2.1.3 Coherent state wave-packets

The continuous-mode coherent state wave-packet is given by [94, p.50]

$$|\alpha_p\rangle = e^{-\frac{1}{2}|\alpha_p|^2} \sum_{n=0}^{\infty} \frac{\alpha_p^n}{\sqrt{n!}} |n_p\rangle = e^{-\frac{1}{2}|\alpha_p|^2} \sum_{n=0}^{\infty} \frac{\alpha_p^n (A_p^\dagger)^n}{n!} |0\rangle = e^{-\frac{1}{2}|\alpha_p|^2} e^{\alpha_p A_p^\dagger} |0\rangle, \quad (2.26)$$

which can also be defined as [95, 96, p. 245]

$$|\alpha_p\rangle = D(\alpha_p) |0\rangle, \quad (2.27)$$

with the continuous-mode displacement operator

$$D(\alpha_p) = \exp[\alpha_p A_p^\dagger - \alpha_p^* A_p]. \quad (2.28)$$

The main properties of the continuous-mode coherent states are,

$$A_p |\alpha_p\rangle = \alpha_p |\alpha_p\rangle, \quad (2.29)$$

$$a_{k,\lambda} |\alpha_p\rangle = \alpha_p f_{k,\lambda} |\alpha_p\rangle. \quad (2.30)$$

And the continuous-mode displacement operator $D(\alpha_p)$ acts as

$$D^\dagger(\alpha_p) A_p D(\alpha_p) = A_p + \alpha_p, \quad (2.31)$$

$$D^\dagger(\alpha_p) A_p^\dagger D(\alpha_p) = A_p^\dagger + \alpha_p^*, \quad (2.32)$$

$$D^\dagger(\alpha_p) a_{k,\lambda} D(\alpha_p) = a_{k,\lambda} + \alpha_p f_{k,\lambda}, \quad (2.33)$$

$$D^\dagger(\alpha_p) a_{k,\lambda}^\dagger D(\alpha_p) = a_{k,\lambda}^\dagger + \alpha_p^* f_{k,\lambda}^*. \quad (2.34)$$

The mean photon number \bar{n} in the coherent state wave-packet is given by

$$\bar{n} = \langle \alpha_p | N | \alpha_p \rangle = |\alpha_p|^2. \quad (2.35)$$

The expectation value of the Hamiltonian equals the energy of the coherent state, as expected

$$\begin{aligned} \langle \alpha_p | H | \alpha_p \rangle &= \left\langle 0 \left| D^\dagger(\alpha_p) \sum_{\lambda=1}^2 \int d^3 k \hbar \omega_k a_{k,\lambda}^\dagger a_{k,\lambda} D(\alpha_p) \right| 0 \right\rangle, \\ &= \left\langle 0 \left| \sum_{\lambda=1}^2 \int d^3 k \hbar \omega_k [a_{k,\lambda}^\dagger + \alpha_p^* f_{k,\lambda}^*] [a_{k,\lambda} + \alpha_p f_{k,\lambda}] \right| 0 \right\rangle, \\ &= \bar{n} \sum_{\lambda=1}^2 \int d^3 k \hbar \omega_k |f_{k,\lambda}|^2. \end{aligned} \quad (2.36)$$

2.2 Two different mode one-dimensional wave-packets

So far we have presented the standard quantized electromagnetic field theory in three-dimensional infinite space. However, the arrangement of a typical optical or microwave experiment makes it feasible to introduce simplifications while retaining realistic properties of the physical system. Most importantly, with a single light beam traveling along a straight line, e.g. in an optical fiber or a waveguide, when transverse effects are unimportant it is advantageous to take a quantization axis of infinite extent parallel to the beam direction and to retain a finite cross-sectional area \mathcal{A} which is determined by the fiber mode or the geometry of the experiment. Also, a laser pulse propagating in the $+z$ direction with a carrier wave vector of k_0 and a slowly varying envelope $f(\omega)$ can be assumed to propagate with a small diffraction angle so that the paraxial approximation $\left| \frac{\partial^2 \Psi}{\partial z^2} \right| \ll k_0 \left| \frac{\partial^2 \Psi}{\partial z} \right|$ for the wave function is valid. A natural description for such a pulse is as a superposition of Gaussian beams with a well defined transverse area \mathcal{A} in the $x - y$ plane, each with wave number $k_0 + \Delta k$, where $\Delta k \ll k_0$ analogous to a narrow-band wave packet of Fourier modes in one dimension. The x and y wave-vector components are thus restricted to discrete values and the three-dimensional integral in Eqs.(2.1,2.2) is converted according to [95]

$$\int d^3 k \rightarrow \frac{(2\pi)^2}{\mathcal{A}} \sum_{k_x, k_y} \int dk_z. \quad (2.37)$$

The summation in Eq.(2.37) can be removed since we only consider field excitation with $k_x = k_y = 0$, and put $k_z = k = \omega/c$. The other required conversions are

$$\begin{aligned}\delta^3(\mathbf{k} - \mathbf{k}') &\rightarrow \frac{\mathcal{A}}{(2\pi)^2} \delta(k - k'), \\ a_{\mathbf{k},\lambda} &\rightarrow \frac{\sqrt{\mathcal{A}}}{2\pi} a_{\omega,\lambda}.\end{aligned}\quad (2.38)$$

The field operator Eq.(2.1) thus becomes

$$\mathbf{E}(z, t) = i \sum_{\lambda=1}^2 \int_0^\infty d\omega \left(\frac{\hbar\omega}{4\pi\epsilon_0 c \mathcal{A}} \right)^{1/2} e^{ikz} \left[e^{-i\omega t} a_{\omega,\lambda} - e^{i\omega t} a_{\omega,\lambda}^\dagger \right], \quad (2.39)$$

with the new commutator being

$$[a_{\omega,\lambda}, a_{\omega',\lambda'}^\dagger] = \delta_{\lambda,\lambda'} \delta(\omega - \omega'). \quad (2.40)$$

In the following, we consider the electric and magnetic field operator in both the left and right propagating modes

$$\begin{aligned}\mathbf{E}(z, t) &= \mathbf{E}_r(z, t) + \mathbf{E}_l(z, t) \\ &= i \int_0^\infty d\omega \left(\frac{\hbar\omega}{4\pi\epsilon_0 c \mathcal{A}_r} \right)^{1/2} e^{ikz} \left[e^{-i\omega t} a_{\omega,r} - e^{i\omega t} a_{\omega,r}^\dagger \right] \\ &\quad + i \int_0^\infty d\omega \left(\frac{\hbar\omega}{4\pi\epsilon_0 c \mathcal{A}_l} \right)^{1/2} e^{-ikz} \left[e^{-i\omega t} a_{\omega,l} - e^{i\omega t} a_{\omega,l}^\dagger \right],\end{aligned}\quad (2.41)$$

$$\begin{aligned}\mathbf{B}(z, t) &= \mathbf{B}_r(z, t) + \mathbf{B}_l(z, t) \\ &= i \int_0^\infty d\omega \left(\frac{\hbar\omega}{4\pi\epsilon_0 c^3 \mathcal{A}_r} \right)^{1/2} e^{ikz} \left[e^{-i\omega t} a_{\omega,r} - e^{i\omega t} a_{\omega,r}^\dagger \right] \\ &\quad + i \int_0^\infty d\omega \left(\frac{\hbar\omega}{4\pi\epsilon_0 c^3 \mathcal{A}_l} \right)^{1/2} e^{-ikz} \left[e^{-i\omega t} a_{\omega,l} - e^{i\omega t} a_{\omega,l}^\dagger \right],\end{aligned}\quad (2.42)$$

with $j = r, l$ stands for right, left, respectively. The energy content of a propagating field is conveniently expressed by its intensity or the normally ordered Poynting vector oriented parallel

to the z axis

$$\begin{aligned}
S(z, t) &= S_r(z, t) + S_l(z, t), \\
S_j(z, t) &= \frac{1}{\mu_0} \left[\mathbf{E}_j^-(z, t) \mathbf{B}_j^+(z, t) + \mathbf{B}_j^-(z, t) \mathbf{E}_j^+(z, t) \right], \\
&= \frac{\hbar}{2\pi\mathcal{A}_j} \int_0^\infty d\omega \int_0^\infty d\omega' \sqrt{\omega\omega'} a_{\omega,j}^\dagger a_{\omega',j} e^{i(\omega-\omega')(t\mp z/c)}. \tag{2.43}
\end{aligned}$$

The integration of Eq.(2.43) gives the total energy flow through a plane of constant z as

$$\begin{aligned}
H &= H_r + H_j, \\
H_j &= \int_0^\infty d\omega \hbar\omega a_{\omega,j}^\dagger a_{\omega,j} = \mathcal{A}_j \int_{-\infty}^\infty dt S_j(z, t). \tag{2.44}
\end{aligned}$$

It is convenient to introduce the Fourier-transformed field operators as

$$a_{t,j} = \frac{1}{\sqrt{2\pi}} \int d\omega a_{\omega,j} e^{-i\omega t}. \tag{2.45}$$

The corresponding one-dimensional photon wave-packet operator reads

$$A_j^\dagger = \int dt \xi_j(t) a_{t,j}^\dagger = \int d\omega f_j(\omega) a_{\omega,j}^\dagger, \tag{2.46}$$

where $\xi_j(t)$ is the temporal shape of the wave-packet and $f_j(\omega)$ is the spectral distribution function.

They are related by the Fourier transform

$$\xi_j(t) = \frac{1}{\sqrt{2\pi}} \int d\omega f_j(\omega) e^{-i\omega t}, \tag{2.47}$$

and the magnitudes are normalized according to

$$\int dt |\xi_j(t)|^2 = \int d\omega |f_j(\omega)|^2 = 1. \tag{2.48}$$

The corresponding photon number operator is

$$n_j = \int dt a_{t,j}^\dagger a_{t,j} = \int d\omega a_{\omega,j}^\dagger a_{\omega,j}. \tag{2.49}$$

2.2.1 Two-mode Fock state wave-packets

In this way, two spatial-mode photon Fock state is given by

$$|n_r, n_l\rangle = \frac{1}{\sqrt{n_r! n_l!}} (A_r^\dagger)^{n_r} (A_l^\dagger)^{n_l} |0_r, 0_l\rangle, \quad (2.50)$$

with the total photon number operator being

$$n = n_r + n_l. \quad (2.51)$$

2.2.2 Two-mode coherent state wave-packets

The corresponding two-mode coherent state wave-packets is given by

$$\begin{aligned} |\alpha_r, \alpha_l\rangle &= D_r(\alpha_r) D_l(\alpha_l) |0_r, 0_l\rangle \\ &= \prod_{j=r,l} \exp[\alpha_j A_j^\dagger - \alpha_j^* A_j] |0_r, 0_l\rangle, \end{aligned} \quad (2.52)$$

and the total mean photon number \bar{n} is

$$\bar{n} = \bar{n}_r + \bar{n}_l = |\alpha_r|^2 + |\alpha_l|^2. \quad (2.53)$$

2.3 The quantized atom-field interaction

In this section, we consider the interaction between a single two-level atom and the quantized radiation field.

2.3.1 The two-level atom

The Hamiltonian of an atomic system is given by

$$H_a = \sum_i E_i |i\rangle \langle i| = \sum_i E_i \sigma_{i,i}, \quad (2.54)$$

where $\{|i\rangle\}$ represents the complete set of atomic energy levels with the corresponding energy eigenvalues E_i , i.e., $H_a |i\rangle = E_i |i\rangle$ and $\sum_i |i\rangle \langle i| = 1$. Similarly, the atomic dipole operator \mathbf{d} can

be expressed in terms of the atom transition operators $\sigma_{ij} = |i\rangle\langle j|$,

$$\mathbf{d} = e\mathbf{r} = e \sum_{i,j} |i\rangle\langle i| \mathbf{r} |j\rangle\langle j| = \sum_{i,j} d_{i,j} \sigma_{i,j}, \quad (2.55)$$

where $d_{i,j} = e \langle i| \mathbf{r} |j\rangle$ is the electric-dipole transition matrix element.

We now proceed with the case of a single two-level atom with ground state $|g\rangle$ and excited state $|e\rangle$. The atomic Hamiltonian can be rewritten as

$$H_a = E_g |g\rangle\langle g| + E_e |e\rangle\langle e| = \frac{1}{2} \hbar\omega_a (\sigma_{ee} - \sigma_{gg}) + \frac{1}{2} (E_e + E_g), \quad (2.56)$$

where we use $E_e - E_g = \hbar\omega_a$ and $\sigma_{ee} + \sigma_{gg} = 1$. By using the following notation

$$\sigma_z = |e\rangle\langle e| - |g\rangle\langle g|, \quad (2.57)$$

$$\sigma_+ = |e\rangle\langle g|, \quad \sigma_- = |g\rangle\langle e|, \quad (2.58)$$

the atomic Hamiltonian Eq.(2.56) takes the form

$$H_a = \frac{1}{2} \hbar\omega_a \sigma_z. \quad (2.59)$$

Moreover, the atomic dipole operator \mathbf{d} in Eq.(2.56) has the form

$$\mathbf{d} = d(\sigma_+ + \sigma_-) \mathbf{e}_d, \quad (2.60)$$

for the reason that electric dipole transitions only have a non-vanishing matrix element between quantum states with different parity $d_{e,e} = d_{g,g} = 0$, and the scalar atomic dipole momentum d is defined as $d = d_{e,g} = d_{g,e}$, and \mathbf{e}_d is the unit dipole vector.

2.3.2 Interaction with a single two-level atom

With the help of Eqs.(2.59, 2.60, 2.1), the interaction between the radiation field and the single atom can be described by the following Hamiltonian in dipole approximation:

$$H = H_0 + H_{int} \quad (2.61)$$

$$\begin{aligned} H_0 &= H_a + H_f, \\ &= \frac{1}{2}\hbar\omega_a\sigma_z + \sum_{\lambda=1}^2 \int d^3\mathbf{k} \hbar\omega_k a_{\mathbf{k},\lambda}^\dagger a_{\mathbf{k},\lambda}, \end{aligned} \quad (2.62)$$

$$\begin{aligned} H_{int} &= -\mathbf{d} \cdot \mathbf{E}(\mathbf{r}_a), \\ &= -i\hbar \sum_{\lambda=1}^2 \int d^3\mathbf{k} [g_{\mathbf{k},\lambda}(\mathbf{r}_a) \sigma_+ a_{\mathbf{k},\lambda} - h.c.] \end{aligned} \quad (2.63)$$

where the coupling strength is given by

$$g_{\mathbf{k},\lambda}(\mathbf{r}_a) = d \sqrt{\frac{\omega_k}{(2\pi)^3 2\hbar\epsilon_0}} u_{\mathbf{k},\lambda}(\mathbf{r}_a) \mathbf{e}_d \cdot \boldsymbol{\epsilon}_{\mathbf{k},\lambda}. \quad (2.64)$$

Notably, the electric field operator is evaluated at the position of the point atom \mathbf{r}_a in dipole approximation.

In the interaction picture and rotating wave approximation [94, p.196], the dynamics of the system is described by the Hamiltonian

$$\begin{aligned} H_I &= e^{iH_0t/\hbar} H_{int} e^{-iH_0t/\hbar}, \\ &= -i\hbar \sum_{\lambda=1}^2 \int d^3\mathbf{k} [g_{\mathbf{k},\lambda}(\mathbf{r}_a) \sigma_+ a_{\mathbf{k},\lambda} e^{-i(\omega_k - \omega_a)t} - h.c.]. \end{aligned} \quad (2.65)$$

2.4 Spontaneous emission in free space

A direct application of the continuous mode theory is the free space atomic spontaneous emission model, where we assume that at initial time t_0 the atom is in the excited state $|e\rangle$ and the electric field in the vacuum state $|0\rangle$. A general state vector for this case is therefore

$$|\psi(t)\rangle = C_e(t) |e, 0\rangle + \sum_{\lambda=1}^2 \int d^3\mathbf{k} C_{g,\mathbf{k},\lambda}(t) |g, 1_{\mathbf{k},\lambda}\rangle, \quad (2.66)$$

with initial condition

$$C_e(t_0) = 1, \quad C_{g,k,\lambda}(t_0) = 0. \quad (2.67)$$

Substituting Eqs.(2.65,2.66,) into the Schrödinger equation

$$i\hbar \frac{\partial |\psi(t)\rangle}{\partial t} = H_I |\psi(t)\rangle, \quad (2.68)$$

and projecting onto the states $|e, 0\rangle$ and $|g, 1_{k,\lambda}\rangle$, we find the probability amplitude equations of motion

$$\dot{C}_e(t) = -i \sum_{\lambda=1}^2 \int d^3 \mathbf{k} g_{k,\lambda}^*(\mathbf{r}_a) e^{i(\omega_k - \omega_a)t} C_{g,k,\lambda}(t), \quad (2.69)$$

$$\dot{C}_{g,k,\lambda}(t) = -i g_{k,\lambda}(\mathbf{r}_a) e^{-i(\omega_k - \omega_a)t} C_e(t). \quad (2.70)$$

In order to get an equation that involves $C_e(t)$ only, we first integrate Eq.(2.70)

$$C_{g,k,\lambda}(t) = -i g_{k,\lambda}(\mathbf{r}_a) \int_{t_0}^t dt' e^{-i(\omega_k - \omega_a)t'} C_e(t'). \quad (2.71)$$

Substituting Eq.(2.71) into the Eq.(2.69), we obtain

$$\dot{C}_e(t) = - \sum_{\lambda=1}^2 \int d^3 \mathbf{k} |g_{k,\lambda}(\mathbf{r}_a)|^2 \int_{t_0}^t dt' e^{-i(\omega_k - \omega_a)(t-t')} C_e(t'). \quad (2.72)$$

By going to the spherical coordinates, see Fig.(2.1), we have

$$\dot{C}_e(t) = - \sum_{\lambda=1}^2 \int_0^{2\pi} d\phi \int_0^\pi d\theta \int_0^\infty d\omega_k \frac{\omega_k^2}{c^3} |g_{\omega_k,\lambda}(\phi, \theta)|^2 \int_{t_0}^t dt' e^{-i(\omega_k - \omega_a)(t-t')} C_e(t'), \quad (2.73)$$

which is still an exact expression.

To solve the integration, we make the *first Markov approximation* [97, 98, p.342], which gives two ways to proceed with this equation by making the integration in different orders with the corresponding different assumptions.

- We assume that the atom dominantly couples to a band of frequencies centered at ω_a with a width ϑ which is much smaller than the optical frequency ω_a [94, 97, p.207]. And inside

the frequency band $[\omega_a - \vartheta, \omega_a + \vartheta]$, ω_k is approximately constant thus $\omega_k \simeq \omega_a$ and $g_{\omega_k, \lambda}(\phi, \theta) \simeq g_{\omega_a, \lambda}(\phi, \theta)$. Thus the frequency integration can be understood as integrals of the form

$$\int_0^\infty d\omega_k \alpha(\omega_k) \dots \rightarrow \alpha(\omega_a) \int_{\omega_a - \vartheta}^{\omega_a + \vartheta} d\omega_k \dots \quad (2.74)$$

The remaining ω_k -integrals over the frequency band $[\omega_a - \vartheta, \omega_a + \vartheta]$ is

$$\int_{\omega_a - \vartheta}^{\omega_a + \vartheta} d\omega_k e^{-i(\omega_k - \omega_a)(t - t')} = 2 \frac{\sin \vartheta(t - t')}{(t - t')}, \quad (2.75)$$

which gives rise to the δ -function in the limit of $\vartheta \rightarrow \infty$

$$\lim_{\vartheta \rightarrow \infty} 2 \frac{\sin \vartheta(t - t')}{(t - t')} = 2\pi \lim_{\vartheta \rightarrow \infty} \frac{\sin \vartheta(t - t')}{\pi(t - t')} = 2\pi \delta(t - t'). \quad (2.76)$$

- In the second approach, we first deal with the integration over time by assuming that the coefficient $C_e(t')$ is a slowly varying function compared to the fast oscillating dephasing factor $e^{-i(\omega_k - \omega_a)(t - t')}$. Therefore, the integral will be different from zero only for $t' \approx t$, and we can indeed replace $C_e(t')$ by $C_e(t)$ and move it out of the integral.

In the long time limit,

$$\lim_{t \rightarrow \infty} \int_{t_0}^t dt' e^{-i(\omega_k - \omega_a)(t - t')} = \pi \delta(\omega_k - \omega_a) + i\mathcal{P}\left(\frac{1}{\omega_a - \omega_k}\right), \quad (2.77)$$

where \mathcal{P} denotes the principal value of the integral.

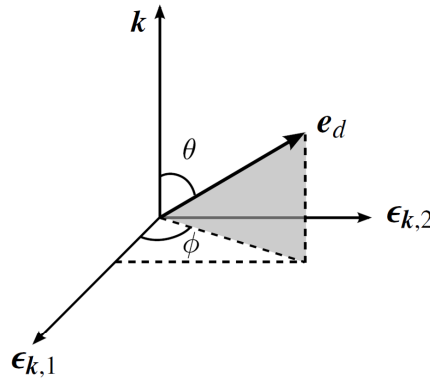


Figure 2.1: Diagram of coordinate system for running plane wave with wave vector \mathbf{k} and two transverse polarizations along the directions $\boldsymbol{\epsilon}_{k,1}$ and $\boldsymbol{\epsilon}_{k,2}$. The unit atomic dipole vector \mathbf{e}_d points in a direction at angle θ with respect to the propagation direction \mathbf{k} and ϕ with respect to $\boldsymbol{\epsilon}_{k,1}$.

It is worth mentioning that both approaches lead to the Weisskopf-Wigner prediction of the spontaneous emission [98, 99, p. 344]. However, the principal value part in the second approach gives the information about the energy level shift as well.

Put everything together, Eq.(2.72) can therefore be written as

$$\dot{C}_e(t) = -\left(\frac{\gamma_0}{2} + i\Delta\right)C_e(t), \quad (2.78)$$

with the *decay rate*

$$\gamma_0 = 2\pi \sum_{\lambda=1}^2 \int d^3\mathbf{k} |g_{\mathbf{k},\lambda}(\mathbf{r}_a)|^2 \delta(\omega_{\mathbf{k}} - \omega_a), \quad (2.79)$$

and the *level shift*

$$\Delta = \sum_{\lambda=1}^2 \int d^3\mathbf{k} |g_{\mathbf{k},\lambda}(\mathbf{r}_a)|^2 \mathcal{P}\left(\frac{1}{\omega_a - \omega_{\mathbf{k}}}\right). \quad (2.80)$$

If we choose plane wave decomposition $u_{\mathbf{k},\lambda}(\mathbf{r}_a) = e^{i\mathbf{k}\mathbf{r}_a}$ for the free space radiation field in the coupling strength Eq.(2.64) and substitute it into the decay rate Eq.(2.79), then we have the standard spontaneous decay rate in Weisskopf-Wigner theory [98, 99, p. 344].

$$\begin{aligned} \gamma_0 &= \frac{1}{2(2\pi)^2} \left(\frac{\omega_a}{c}\right)^3 \frac{d^2}{\hbar\epsilon_0} \int_0^{2\pi} d\phi \int_0^\pi d\theta \sum_{\lambda=1}^2 |e_a \cdot \epsilon_{\mathbf{k}_a,\lambda}|^2, \\ &= \frac{1}{2(2\pi)^2} \left(\frac{\omega_a}{c}\right)^3 \frac{d^2}{\hbar\epsilon_0} \int_0^{2\pi} d\phi \int_0^\pi d\theta \sin^3\theta |\sin^2\phi + \cos^2\phi|, \\ &= \frac{1}{3\pi} \left(\frac{\omega_a}{c}\right)^3 \frac{d^2}{\hbar\epsilon_0}, \end{aligned} \quad (2.81)$$

which predicts an irreversible exponential decay of the upper state population [99].

Moreover, the level shift in Eq.(2.80) reads

$$\Delta = \frac{d^2}{6\pi^2 c^3 \hbar \epsilon_0} \int d\omega_{\mathbf{k}} \mathcal{P}\left(\frac{\omega_{\mathbf{k}}^3}{\omega_a - \omega_{\mathbf{k}}}\right). \quad (2.82)$$

The expression in Eq.(2.82) can be used to understand the *Lamb shift*. The level shift in the

atomic level n is given by summing up all the intermediate atomic levels m

$$\begin{aligned}
\Delta_{Lamb} &= \sum_m \Delta_{mn} \\
&\rightarrow \frac{1}{6\pi^2 c^3 \hbar \epsilon_0} \sum_m d_{mn}^2 \int_0^{m_e c^2 / \hbar} d\omega_k \mathcal{P} \left(\frac{\omega_k^3}{\omega_{mn} - \omega_k} \right) \\
&\cong \frac{1}{6\pi^2 c^3 \hbar \epsilon_0} \sum_m d_{mn}^2 \omega_{mn}^3 \ln \left(\frac{m_e c^2}{|E_m - E_n|} \right), \\
&= \frac{2\alpha}{3\pi \hbar m_e^2 c^2} \sum_m |\mathbf{p}|_{mn}^2 (E_m - E_n) \ln \left(\frac{m_e c^2}{|E_m - E_n|} \right), \tag{2.83}
\end{aligned}$$

where α is the fine-structure constant. Here we introduced the high-frequency cutoff $\omega_f = m_e c^2 / \hbar$, made that approximation that $m_e c^2 \gg |E_m - E_n|$, and used that the canonical momentum $|\mathbf{p}|_{mn}^2 = m_e^2 d_{mn}^2 \omega_{mn}^2 / e^2$ [p.82-93] [100].

Following Bethe's method of replacing the logarithm by an average value, independent of m , as a first approximation [101]

$$\sum_m |\mathbf{p}|_{mn}^2 (E_m - E_n) = \frac{1}{2} \hbar^2 \int d^3 r |\psi_n(\mathbf{r})|^2 \nabla^2 V(\mathbf{r}), \tag{2.84}$$

where V is the binding potential. For the Coulomb potential $V = -Ze^2/r$, we have $\nabla^2 V = 4\pi Ze^2 \delta^3(\mathbf{r})$ and

$$\sum_m |\mathbf{p}|_{mn}^2 (E_m - E_n) = 2\pi \hbar^2 e^2 Z |\psi_n(0)|^2, \tag{2.85}$$

for a nuclear charge Z .

The *Lamb shift* in Eq.(2.83) then reads [p.88] [100].

$$\Delta_{Lamb} \cong \frac{4\alpha Z \hbar e^2}{m_e^2 c^2} |\psi_n(0)|^2 \ln \left(\frac{m_e c^2}{|E_m - E_n|_{avg}} \right), \tag{2.86}$$

For a state with the angular momentum $l = 0$,

$$|\psi_n(0)|^2 = \frac{1}{\pi} \left(\frac{Z}{na_0} \right)^3, \tag{2.87}$$

and the *Lamb shift*

$$\Delta_{Lamb} \cong \frac{8\alpha^3 Z^4}{3\pi n^3 \hbar} R_\infty \ln \left(\frac{m_e c^2}{|E_m - E_n|_{avg}} \right), \tag{2.88}$$

where n is the principal quantum number, a_0 is the Bohr radius, and R_∞ is the Rydberg unit of energy for infinite nuclear mass.

Now we consider the example of the ${}^2S_{1/2}$ and ${}^2P_{1/2}$ states of the hydrogen atom, which is found to be

$$\Delta_{Lamb} \cong 1040 \text{ MHz}, \quad (2.89)$$

and is very small compared to the optical transition frequency of about hundreds of THz. Here the average excitation energy $|E_m - E_n|_{avg}$ for ${}^2S_{1/2}$ state of the hydrogen has been replaced by $17.8R_\infty$ with numerical estimation [101].

Excitation of an atom by propagating pulses

In this chapter, we focus on the effect of the temporal-spectral features of the single photon pulse on the probability of finding the atom in the excited state starting from the ground state (“excitation probability”). We present the general formalism and apply it in two specific situations: excitation of the atom by single photon Fock state wave packets and coherent state wave packets.

3.1 Quantum Heisenberg-Langevin approach

We now introduce the quantum mechanical Heisenberg-Langevin formalism to gain more insight into the atom-pulse problem while taking into account the environment.

We apply Heisenberg equation of motion

$$\dot{O}(t) = \frac{1}{i\hbar} [O(t), H(t)] \quad (3.1)$$

to both field and atomic operators in the atom-field interaction Hamiltonian Eq.(2.65). Therefore we have a set of differential equations for the field operator

$$\dot{a}_{\mathbf{k},\lambda} = g_{\mathbf{k},\lambda}^*(\mathbf{r}_a) \sigma_- e^{i(\omega_{\mathbf{k}} - \omega_a)t}, \quad (3.2)$$

and the modified Heisenberg-Langevin equation for arbitrary atomic operator O

$$\begin{aligned} \dot{O} = & \left(\frac{\gamma'}{2} + i\Delta' \right) ([\sigma_+, O]\sigma_- + \sigma_+[O, \sigma_-]) + \zeta_O, \\ & + \sum_{\lambda=1}^2 \int d^3\mathbf{k} \left(g_{\mathbf{k},\lambda}(\mathbf{r}_a)[\sigma_+, O] a_{\mathbf{k},\lambda} e^{-i(\omega_{\mathbf{k}} - \omega_a)t} + g_{\mathbf{k},\lambda}^*(\mathbf{r}_a) a_{\mathbf{k},\lambda}^\dagger [O, \sigma_-] e^{i(\omega_{\mathbf{k}} - \omega_a)t} \right), \end{aligned} \quad (3.3)$$

where the decay term γ' , the frequency shift Δ' , and the noise operators ζ_O are introduced to account for the interaction of the atom with the environment.

By integrating Eq.(3.2), the field operator reads [102, p. 393]

$$a_{\mathbf{k},\lambda}(t) = a_{\mathbf{k},\lambda}(t_0) + g_{\mathbf{k},\lambda}^*(\mathbf{r}_a) \int_{t_0}^t dt' \sigma_-(t') e^{i(\omega_{\mathbf{k}} - \omega_a)t'}, \quad (3.4)$$

where the first part represents the initial ‘‘free field’’ and the second part is the ‘‘source field’’ which comes from the radiation of the atom.

We substitute Eq.(3.4) back into Eq.(3.3) and by making the first Markov approximation again [98, p.341], we have

$$\begin{aligned} \dot{O} = & \left(\frac{\gamma_0}{2} + i\Delta \right) ([\sigma_+, O]\sigma_- + \sigma_+[O, \sigma_-]) + \zeta_O \\ & + \sum_{\lambda=1}^2 \int d^3\mathbf{k} \left(g_{\mathbf{k},\lambda}(\mathbf{r}_a)[\sigma_+, O] a_{\mathbf{k},\lambda}(t_0) e^{-i(\omega_{\mathbf{k}} - \omega_a)t} + g_{\mathbf{k},\lambda}^*(\mathbf{r}_a) a_{\mathbf{k},\lambda}^\dagger(t_0) [O, \sigma_-] e^{i(\omega_{\mathbf{k}} - \omega_a)t} \right). \end{aligned} \quad (3.5)$$

Here the standard spontaneous decay rate in free space γ_0 has been split into two parts [103]:

$$\gamma_0 = \gamma' + \gamma_p, \quad (3.6)$$

the decay into the environment γ' , which is the non-pulse mode in our case, and the decay into the pulse mode γ_p

$$\begin{aligned} \gamma_p = & 2\pi \sum_{\lambda=1}^2 \int d^3\mathbf{k} |g_{\mathbf{k},\lambda}(\mathbf{r}_a)|^2 \delta(\omega_{\mathbf{k}} - \omega_a), \\ = & \frac{1}{2(2\pi)^2} \left(\frac{\omega_a}{c} \right)^3 \frac{d^2}{\hbar\epsilon_0} \Lambda = \gamma_0 \frac{\Lambda}{8\pi/3}. \end{aligned} \quad (3.7)$$

The spatial overlap parameter is given by

$$\Lambda = \sum_{\lambda=1}^2 \int d\Omega |u_{r_a,\lambda}(\mathbf{r}_a)|^2 |\mathbf{e}_d \cdot \boldsymbol{\epsilon}_{r_a,\lambda}|^2, \quad (3.8)$$

where the integration runs over the solid angle $d\Omega$ covered by the pulse mode and the indices k_a respect the condition $|\mathbf{k}_a| = k_a$ coming from the delta distribution. It is worth noting that by choosing plane wave $u_{k,\lambda}(\mathbf{r}_a) = e^{i\mathbf{k}\mathbf{r}_a}$ and performing the integration over the whole solid angle, the parameter reaches its maximum value $\Lambda = 8\pi/3$ and we have the well known free space spontaneous decay γ_0 in Eq.(2.79) [102, p. 530]. This is as well the maximum possible value for the pulse mode decay for a certain experimental setting

$$\gamma_p = \gamma_0 \frac{\Lambda}{8\pi/3}. \quad (3.9)$$

Thus the single parameter $\Lambda \in [0, 8\pi/3]$ describes the electric field polarization distribution weighted by the atomic dipole distribution in the solid angle covered by the pulse.

Similarly, the total frequency shift Δ also includes the contribution from the pulse mode Δ' and the non-pulse mode Δ_p .

3.2 Atomic state population

From Eq.(3.5), we find the following closed set of equations

$$\dot{\sigma}_z = -\gamma_0(\sigma_z + 1) - 2 \sum_{\lambda=1}^2 \int d^3\mathbf{k} [g_{k,\lambda}(\mathbf{r}_a)\sigma_+ a_{k,\lambda}(t_0)e^{-i(\omega_k - \omega_a)t} + h.c.] + \zeta_z, \quad (3.10)$$

$$\dot{\sigma}_- = -\frac{\gamma_0}{2}\sigma_- + \sigma_z \sum_{\lambda=1}^2 \int d^3\mathbf{k} g_{k,\lambda}(\mathbf{r}_a)a_{k,\lambda}(t_0)e^{-i(\omega_k - \omega_a)t} + \zeta_-, \quad (3.11)$$

The population $P(t)$ of the atom being in the excited state is given by the expectation value of atomic operator σ_z on the initial state of the total system $|\psi(t_0)\rangle$,

$$P(t) = \frac{1}{2} (\langle \psi(t_0) | \sigma_z(t) | \psi(t_0) \rangle + 1), \quad (3.12)$$

where $|\psi(t_0)\rangle = |\psi_a, \psi_p, 0_s\rangle$ is a product state of the atomic state, the pulse state, and the initial vacuum state of the environment.

Note that the Langevin-type noise operators ζ_O are determined directly in terms of the initial field operators of the environment $b_{\mathbf{k}', \lambda'}(t_0)$ [94, p. 273], for example,

$$\zeta_z = -2 \sum_{\lambda'} \int d^3 \mathbf{k}' [g_{\mathbf{k}', \lambda'}(\mathbf{r}_a) \sigma_+ b_{\mathbf{k}', \lambda'}(t_0) e^{-i(\omega_{\mathbf{k}'} - \omega_a)t} + h.c.], \quad (3.13)$$

$$\zeta_- = \sigma_z \sum_{\lambda'} \int d^3 \mathbf{k}' g_{\mathbf{k}', \lambda'}(\mathbf{r}_a) b_{\mathbf{k}', \lambda'}(t_0) e^{-i(\omega_{\mathbf{k}'} - \omega_a)t}, \quad (3.14)$$

where $g_{\mathbf{k}', \lambda'}(\mathbf{r}_a)$ is the corresponding coupling strength with the atom. Since for optical transitions, the black body radiation at room temperature is negligible and the environment is nearly in vacuum state, that the average values of the noise operators will vanish as $\langle \zeta_O \rangle = 0$.

Investigation of the atomic dynamics for different initial states of the total system can be done by using the general formalism in Sec.(3.1). With the help of Eqs.(3.10, 3.11), the expectation value of atomic operator $\langle \sigma_z(t) \rangle$ with the initial state of the total system $|\psi(t_0)\rangle = |\psi_a, \psi_p, 0_s\rangle$ will further depend on different state-dependent values of $\langle \sigma_{\pm}(t) \rangle$.

The complete set of equations can be schematically written as

$$\dot{\mathbf{S}}(t) = \mathbf{M} \mathbf{S}(t) + \mathbf{B}. \quad (3.15)$$

The form of the vectors \mathbf{S} , \mathbf{B} and the matrix \mathbf{M} depends upon the initial state and will be specified in the following different cases.

3.2.1 Revisit the atomic spontaneous emission

In this part, we revisit the atomic spontaneous emission problem in Sec.(2.4) by using the formalism developed above. By applying Eq.(3.10) to the initial state of the system $|\psi(t_0)\rangle = |e, 0_p, 0_s\rangle$ — the atom being in excited state with no photon in the pulse mode and the environment in the vacuum state, we therefore have

$$\langle \dot{\sigma}_z(t) \rangle = -\gamma_0 (\langle \sigma_z(t) \rangle + 1), \quad (3.16)$$

Thus we have

$$\dot{P}(t) = -\gamma_0 P(t), \quad (3.17)$$

$$P(t) = e^{-\gamma_0 t}, \quad (3.18)$$

which implies that the atom initially in the excited state $|e\rangle$ decays exponentially in time with the lifetime $\tau = 1/\gamma_0$ in vacuum.

3.2.2 Atomic excitation with single-photon Fock state wave-packet

In this part, we study the excitation probability of the atom from its initial ground state by the single-photon wave-packets as defined in Sec.(2.1.2)

$$|1_p\rangle = \sum_{\lambda} \int d^3 \mathbf{k} f_{\mathbf{k},\lambda}(\mathbf{r}_a) a_{\mathbf{k},\lambda}^{\dagger} |0\rangle \quad (3.19)$$

The explicit form of Eq.(3.15) can now be found with the initial state $|\psi(t_0)\rangle = |g, 1_p, 0_s\rangle$:

$$\mathbf{S}(t) = \begin{pmatrix} \langle g, 1_p, 0_s | \sigma_z(t) | g, 1_p, 0_s \rangle \\ \langle g, 1_p, 0_s | \sigma_+(t) | g, 0_p, 0_s \rangle \\ \langle g, 0_p, 0_s | \sigma_-(t) | g, 1_p, 0_s \rangle \end{pmatrix} \quad (3.20)$$

$$\mathbf{M} = \begin{pmatrix} -\gamma_0 & -2g(t) & -2g^*(t) \\ 0 & -\gamma_0/2 & 0 \\ 0 & 0 & -\gamma_0/2 \end{pmatrix}, \quad \mathbf{B} = \begin{pmatrix} -\gamma_0 \\ -g^*(t) \\ -g(t) \end{pmatrix}, \quad (3.21)$$

with initial condition

$$\mathbf{S}^T(t_0) = \begin{pmatrix} -1 & 0 & 0 \end{pmatrix}. \quad (3.22)$$

The effective time dependent coupling strength is

$$g(t) = \sum_{\lambda=1}^2 \int d^3 \mathbf{k} g_{k,\lambda}(\mathbf{r}_a) f_{k,\lambda}(\mathbf{r}_a) e^{-i(\omega_k - \omega_a)t}. \quad (3.23)$$

The excitation probability is then given by the first component of the vector \mathbf{S}

$$P(t) = \frac{1}{2}(s_1(t) + 1). \quad (3.24)$$

3.2.3 Atomic excitation with single-photon coherent state wave-packet

Let us now look into the pulse initially prepared in a continuous coherent state with $|\psi(t_0)\rangle = |g, \alpha_p, 0_s\rangle$. Again, we get a set of similar differential equations with the same initial condition, but different variables

$$\mathbf{S}(t) = \begin{pmatrix} \langle g, \alpha_p, 0_s | \sigma_z(t) | g, \alpha_p, 0_s \rangle \\ \langle g, \alpha_p, 0_s | \sigma_+(t) | g, \alpha_p, 0_s \rangle \\ \langle g, \alpha_p, 0_s | \sigma_-(t) | g, \alpha_p, 0_s \rangle \end{pmatrix}, \quad (3.25)$$

$$\mathbf{M} = \begin{pmatrix} -\gamma_0 & -2g(t) & -2g^*(t) \\ g^*(t) & -\gamma_0/2 & 0 \\ g(t) & 0 & -\gamma_0/2 \end{pmatrix}, \quad \mathbf{B} = \begin{pmatrix} -\gamma_0 \\ 0 \\ 0 \end{pmatrix}. \quad (3.26)$$

3.3 Numerical analysis of the temporal envelope

With the help of the presented general model, one can study the dependence of excitation probability $P(t)$ on both the spatial and temporal properties of the pulse. In the section, we would like to focus on the temporal and spectral effects of pulse.

3.3.1 Special case: dipole pattern

The pulse field distribution functions $f_{k,\lambda}(\mathbf{r}_a)$ can be written as

$$f_{k,\lambda}(\mathbf{r}_a) = g_{k,\lambda}^*(\mathbf{r}_a) f(\omega_k), \quad (3.27)$$

where the spatial and polarization distribution of the electrical field is included in the coupling strength $g_{k,\lambda}(\mathbf{r}_a)$ as in Eq.(2.64), and $f(\omega_k)$ is the spectral distribution of the pulse. The normalization condition is,

$$\sum_{\lambda=1}^2 \int d^3 \mathbf{k} |g_{k,\lambda}(\mathbf{r}_a)|^2 |f(\omega_k)|^2 = 1. \quad (3.28)$$

Once again with the help of the first Markov approximation, where we assume that the coupling $g_{k,\lambda}$ is constant for frequencies of interest centered around the atomic transition frequency ω_a , one finds that the effective coupling strength $g(t)$ in Eq.(3.23) becomes

$$g(t) = \sqrt{\gamma_p} \xi(t), \quad (3.29)$$

which is the product of the square root of the decay rate into the pulse mode and the normalized temporal envelope of the pulse. Since we are considering the on resonance interaction of the atom and the pulse, we put $\omega_0 = \omega_a$.

In the following, we assume that the pulse occupies the whole solid angle, which implies that $\gamma_p = \gamma_0$. We then discuss the pulse temporal and spectral effect on the excitation probability.

3.3.2 Pulse bandwidth effects

For a fixed pulse envelope, the excitation probability depends on the ratio between the pulse bandwidth Ω and the decay rate γ_0 of the atomic dipole. We take a single photon Fock state pulse with a Gaussian temporal shape as an example, and study the effects of different bandwidths on the excitation probability. The results are plotted in Fig.(3.1).

As we can see from Fig.(3.1), for single photon excitation with shorter pulses ($\Omega \gg \gamma_0$), the bandwidth is too broad for resonant absorption, which reduces the effective coupling strength. For longer pulses ($\Omega \ll \gamma_0$), the photon density in time is too low for efficient interactions [104].

In Fig.(3.2), we show the dependence of the maximum achievable resonant excitation probability on the pulse bandwidth for Gaussian-shaped single photon Fock state and coherent state pulse, where the mean photon number equals 1. We find out that the optimum pulse bandwidth maximizing the absorption with Gaussian-shaped pulses is $\Omega_0 = 1.5\gamma_0$ for a single photon Fock state pulse and $\Omega'_0 = 2.4\gamma_0$ for a single photon coherent state pulse.

For coherent state pulses, we studied the maximal excitation probability as a function of

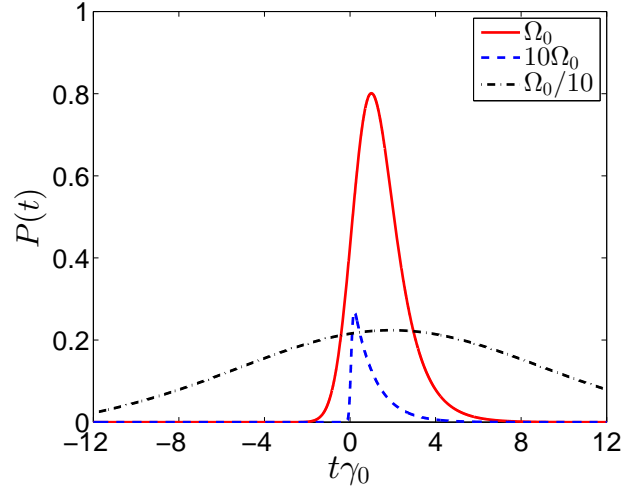


Figure 3.1: Excitation probability $P(t)$ as a function of time with the initial Gaussian pulse in single photon Fock state for different bandwidths. $\Omega_0 = 1.46\gamma_0$, which turns out to be the optimized bandwidth (c.f. Fig.3.2).

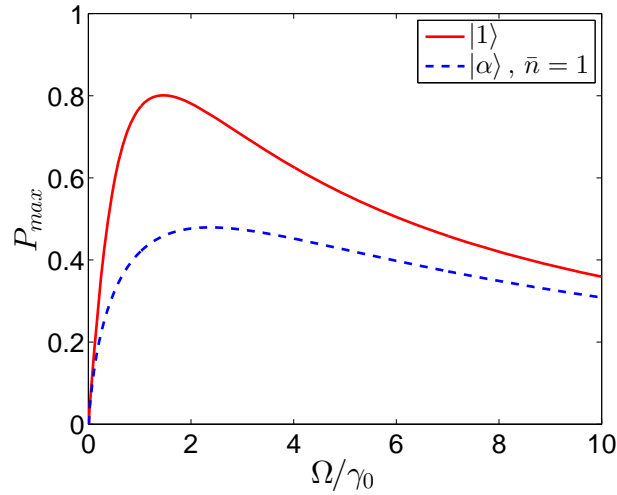


Figure 3.2: Dependence of maximum excitation probability P_{max} on the pulse bandwidth with Gaussian shape for single photon Fock state pulse and single photon coherent state pulse.

the mean number of photons \bar{n} for various choices of the bandwidth, shown in Fig.(3.3). As expected, the maximal excitation probability varies with \bar{n} . The saturation with large \bar{n} for all bandwidths is due to the fact that the effective coupling strength $g(t)$ decreases with the pulse length. Alternatively, this can be understood as the photons arrive more distributed in time. Note that, for large \bar{n} , it is better to choose short intense pulse with $\Omega \gg \Omega'_0 \sim \gamma_0$, which is used for population transfer.

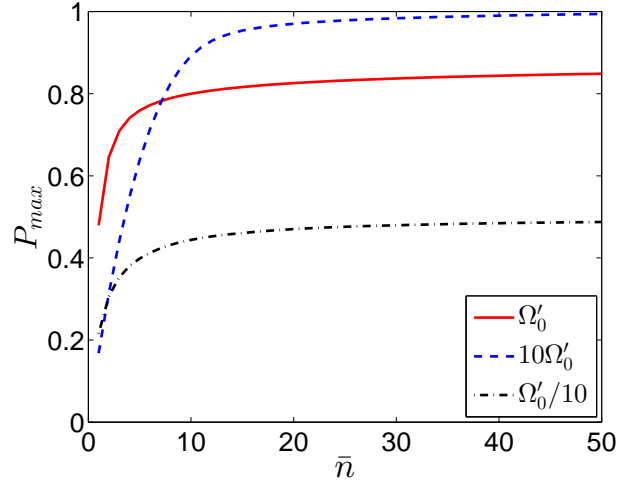


Figure 3.3: Maximum excitation probability P_{max} as a function of the mean photon number \bar{n} with the initial coherent state Gaussian pulse for different bandwidths. $\Omega'_0 = 2.37\gamma_0$ is the optimized bandwidth for a Gaussian pulse (c.f. Fig.(3.2)).

3.3.3 Pulse shape effects

In general, the excitation probability depends on the specific temporal shape of the input pulse.

Here we studied the following six pulse shapes, see Table.(3.1).

For single photon Fock state, the excitation probability has a peak value of about 0.8 with

Table 3.1: Definition of normalized pulse shapes

Type of pulse	Wave function for pulse
Gaussian pulse	$\xi(t) = \left(\frac{\Omega^2}{2\pi}\right)^{1/4} \exp\left(-\frac{\Omega^2}{4} t^2\right)$
Hyperbolic secant pulse	$\sqrt{\frac{\Omega}{2}} \operatorname{sech}(\Omega t)$
Rectangular pulse	$\xi(t) = \begin{cases} \sqrt{\frac{\Omega}{2}}, & \text{for } -\frac{2}{\Omega} \leq t \leq 0 \\ 0, & \text{else} \end{cases}$
Symmetric exponential pulse	$\xi(t) = \sqrt{\Omega} \exp(-\Omega t)$
Decaying exponential pulse	$\xi(t) = \begin{cases} \sqrt{\Omega} \exp\left(-\frac{\Omega}{2} t\right), & \text{for } t > 0 \\ 0, & \text{for } t < 0 \end{cases}$
Rising exponential pulse	$\xi(t) = \begin{cases} \sqrt{\Omega} \exp\left(\frac{\Omega}{2} t\right), & \text{for } t < 0 \\ 0, & \text{for } t > 0 \end{cases}$

optimum bandwidth for the first four pulse shapes, shown in Fig.(3.4) (a)-(d), indicating that the photon absorption is less sensitive to pulse shape effects such as discontinuities. For the

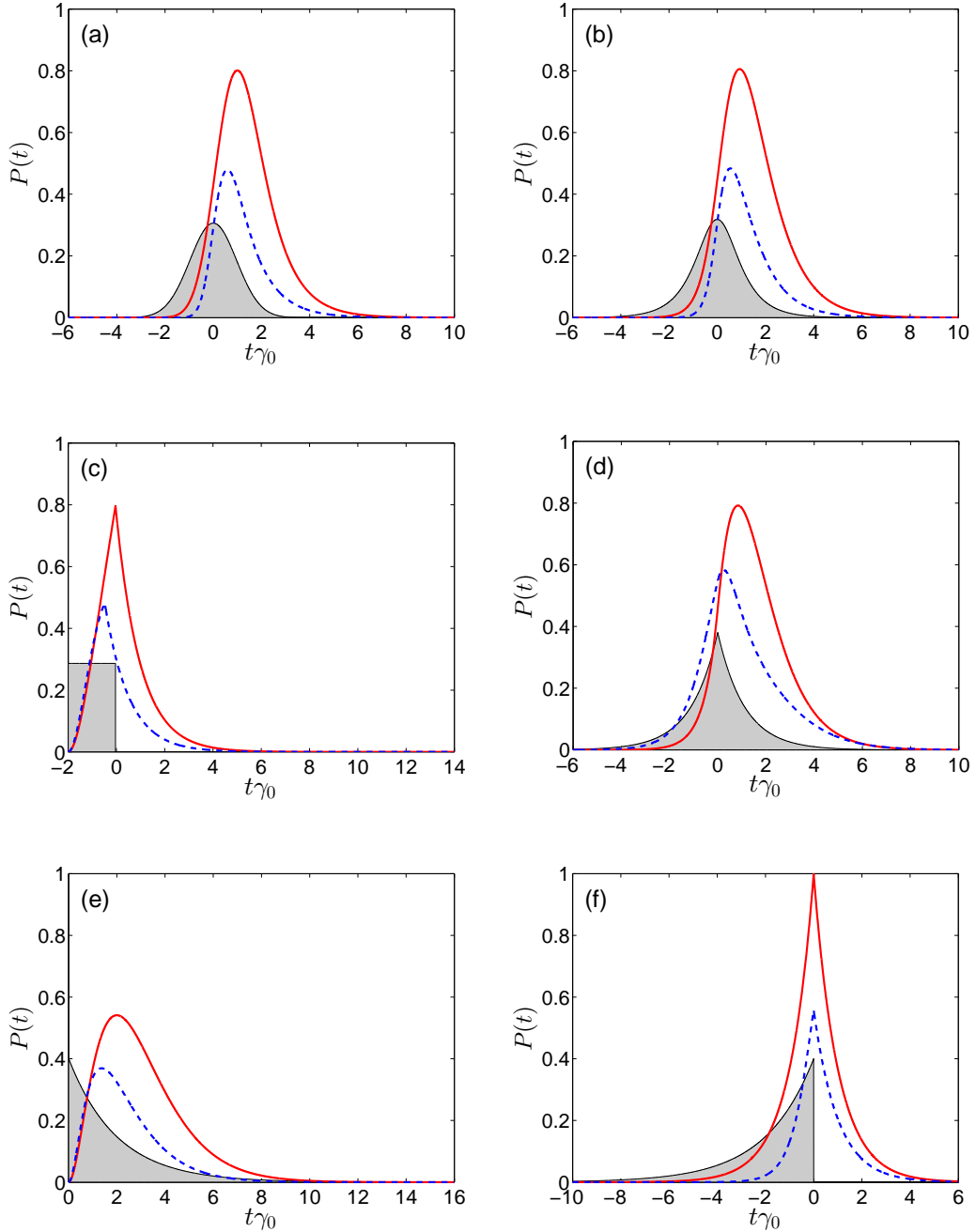


Figure 3.4: Excitation probability $P(t)$ as a function of time for various pulse shapes shown in Table.(3.1) with $\gamma_p = \gamma_0$ ($\Lambda = 8\pi/3$). The single photon Fock state pulse with optimal bandwidth is shown in grey; the corresponding excitation probability is given by the solid black line. The dashed blue line represents the excitation probability for a single photon coherent state pulse of a similar shape but different (optimized) bandwidth. (a) Gaussian pulse, (b) Hyperbolic secant pulse, (c) Rectangular pulse, (d) Symmetric exponential pulse, (e) Decaying exponential pulse and (f) Rising exponential pulse.

decaying exponential pulse, the maximum excitation probability is only 0.54, see Fig.(3.4(e)). A particularly interesting case may be that of the rising exponential single photon Fock state pulse, shown in Fig.(3.4(f)), for which the corresponding maximal excitation probability is 0.995 with a optimal bandwidth of $\Omega_0 = 1\gamma_0$. This agrees well with the prediction that for the aim of unit absorption probability, the incident photon must possess the time reversed properties of the spontaneously emitted photon. Since the spontaneous decay is exponential, the temporal envelope of the pulse has to be rising exponential [53, 55].

On the other hand, for an initial single photon coherent state pulse with optimum bandwidth, the maximum excitation probability is much lower, around 0.48 for the first four pulse shapes and 0.4 and 0.56 for the decaying and rising exponential pulse, respectively. Apparently the excitation is more efficient if exactly one photon is present instead of a distribution with mean one. This emphasizes the importance of generating single photon state rather than using attenuated laser pulse in applications where high absorption is desired.

For the explicit values of optimum bandwidth needed to achieve maximum excitation probability, see Table.(3.2).

Table 3.2: Optimum bandwidth and maximum excitation probability.

Tape of pulse	State	Optimum Ω/γ_0	Maximum $P(t)$
Gaussian pulse	$ \alpha\rangle$	2.37	0.48
	$ 1\rangle$	1.46	0.80
Hyperbolic secant pulse	$ \alpha\rangle$	2.03	0.48
	$ 1\rangle$	1.26	0.80
Rectangular pulse	$ \alpha\rangle$	0.66	0.48
	$ 1\rangle$	0.51	0.81
Symmetric exponential pulse	$ \alpha\rangle$	1.39	0.48
	$ 1\rangle$	0.90	0.79
Decaying exponential pulse	$ \alpha\rangle$	1.42	0.37
	$ 1\rangle$	1.00	0.54
Rising exponential pulse	$ \alpha\rangle$	1.86	0.56
	$ 1\rangle$	1.00	0.996

3.3.4 Damped Rabi oscillation

In Fig.(3.5), the probability of exciting the atom for an initial coherent state Gaussian pulse is evaluated for various mean photon numbers $\bar{n} = (1, 10, 50)$. For large mean photon number, damped Rabi oscillations are observed. In the limit of very large mean photon number, one

would recover the textbook predictions for classical light pulses [94, p. 151].

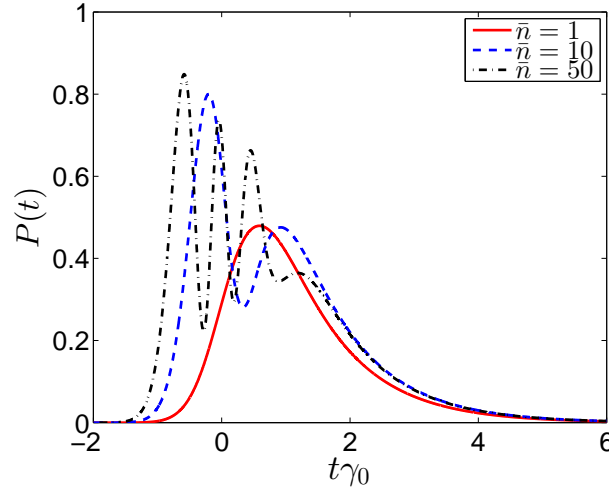


Figure 3.5: Excitation probability $P(t)$ as a function of time for initial coherent state Gaussian pulse with optimal bandwidth $\Omega'_0 = 2.37\gamma_0$ for different mean photon numbers \bar{n} .

3.3.5 Discussion of realistic focusing

Finally we present a brief review of ongoing experiments in order to consider the excitation probability in realistic tight focusing configurations.

In the case of a parabolic mirror with a half opening angle of 134° as it is used in the experiment described in Refs. [105, 106], the corresponding weighted solid angle can reach up to $\Lambda = 0.94 \times 8\pi/3$, and thus one may achieve a maximal excitation probability of 0.94 with rising exponential shape for a single photon Fock state pulse, 0.54 for a single photon coherent state pulse, 0.75 for a Gaussian single photon Fock state pulse and 0.46 for a single photon coherent state pulse.

In Ref. [60, 107], a high aperture lens with $NA = 0.55$ and $f = 4.5$ mm is used to focus a Gaussian beam. The weighted solid angle depends on the focusing strength $u := w_L/f$, where w_L is the beam waist. A maximum overlap of $\Lambda = 0.364 \times 8\pi/3$ is expected at focusing strength $u = 2.239$. With a rising exponential shape, we predict a maximal excitation probability of 0.36 for a single photon Fock state pulse and 0.27 for a single photon coherent state pulse. For a Gaussian shape, we predict a maximal excitation probability of 0.29 for a single photon Fock state pulse and 0.23 for a single photon coherent state pulse.

State-dependent atomic excitation by multi-photon pulses propagating along two spatial modes

In this chapter, we extend the single atom and single photon model described in chapter 3 to the multi-photon case of a single atom and two spatial modes. For simplicity, we reduce the three-dimensional description of the electric field to the case of one-dimensional geometry. It is worth noting that this model can also describe three-dimensional setups, in which the spatial overlap between the angular distribution of the light pulse and atomic dipole pattern is fixed [56]. The atomic dynamics is studied by numerical simulation for different photon states.

4.1 Physical model

As a model system, we consider a two-level atom interacting with one-dimensional photon wave-packets coming from the left, from the right, or from both directions as depicted in Fig.(4.1) (a). The dipole interaction Hamiltonian in the interaction picture and rotating wave approximation is given by [104]

$$H_I(t) = -i\hbar \sum_{j=r,l} \int d\omega g_{\omega,j} [\sigma_+ a_{\omega,j} e^{-i(\omega-\omega_a)t} - h.c.], \quad (4.1)$$

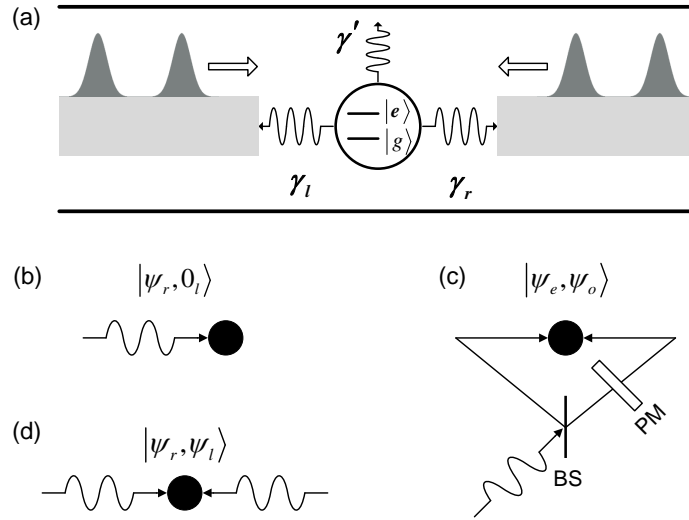


Figure 4.1: (a) Schematic picture of the system: a two-level atom is coupled to the right- and left-propagating pulses with the radiative decay rates γ_r and γ_l , respectively. γ' describes the decay rate into the environment. Simplified illustration of the pulse spatial-modes considered in this study: (b) single spatial-mode. (c) even- and odd-parity mode. (d) two distinct spatial-modes. The atom is indicated by the black circle and the arrows indicate the input pulses. BS: beam-splitter. PM: phase modulator.

where we used the one-dimensional continuum electric field in Eq.(2.41).

The coupling strength is

$$g_{\omega,r} = d \sqrt{\frac{\omega}{4\pi\hbar\epsilon_0 c \mathcal{A}_r}} e^{i\theta_r}, \quad g_{\omega,l} = d \sqrt{\frac{\omega}{4\pi\hbar\epsilon_0 c \mathcal{A}_l}} e^{i\theta_l} \quad (4.2)$$

with the phases $\theta_r = k z_a$, $\theta_l = -k z_a$, and we have assumed that the dipole moment is oriented parallel to the field polarization at the atomic position z_a yielding maximum coupling strength.

Using the formalism described in chapter 3, we have the following set of modified optical Bloch equations [104] by substituting the atomic operators σ_z, σ_- into Eqs.(3.5,3.6,3.7),

$$\dot{\sigma}_- = -\frac{\gamma_0}{2}\sigma_- + \zeta_- + \sigma_z \sum_{j=r,l} \sqrt{\frac{\gamma_j}{2\pi}} \int d\omega e^{i2\theta_j} e^{-i(\omega-\omega_a)t} a_{\omega,j}(t_0), \quad (4.3)$$

$$\begin{aligned} \dot{\sigma}_z = & -\gamma_0(\sigma_z + 1) + \zeta_z \\ & - 2 \sum_{j=r,l} \sqrt{\frac{\gamma_j}{2\pi}} \int d\omega e^{i2\theta_j} \left[e^{-i(\omega-\omega_a)t} \sigma_+ a_{\omega,j}(t_0) + h.c. \right], \end{aligned} \quad (4.4)$$

where the free space spontaneous decay rate is made up of three parts:

$$\gamma_0 = \gamma' + \gamma_r + \gamma_l, \quad (4.5)$$

the decay into the environment γ' , and the decay into the right (left) modes γ_r (γ_l), respectively. Using the Weisskopf-Wigner theory [94, p. 207], the frequency-dependent coupling strengths are approximately constant $|g_{\omega,j}| \approx |g_{\omega_a,j}|$, and thus the explicit formula of γ_j are given by

$$\gamma_j = 2\pi |g_{\omega_a,j}|^2. \quad (4.6)$$

It is convenient to introduce the Fourier-transformed field operators

$$a_{t,j} = \frac{1}{\sqrt{2\pi}} \int d\omega a_{\omega,j} e^{-i(\omega-\omega_a)t}, \quad (4.7)$$

with which the evolution of the atomic operators can be simplified into

$$\dot{\sigma}_- = -\frac{\gamma_0}{2}\sigma_- + \zeta_- + \sum_{j=r,l} \sqrt{\gamma_j} e^{i2\theta_j} \sigma_z a_{t,j}, \quad (4.8)$$

$$\dot{\sigma}_z = -\gamma_0(\sigma_z + 1) + \zeta_z - 2 \sum_{j=r,l} \sqrt{\gamma_j} e^{i2\theta_j} [\sigma_+ a_{t,j} + h.c.]. \quad (4.9)$$

4.2 Atomic excitation by different pulses

Investigation of the atomic dynamics as a function of the relative position of the atom and the incident light fields is certainly interesting and can be done using the general equations Eqs.(4.8, 4.9) developed in section 4.1. This can be achieved by changing either the atomic position z_a , or the initial positions of right and left pulses, or both. However, in this work we consider only the situation when the two pulses come symmetrically to the atom. We thus set, without loss of generality, the atomic position $z_a = 0$.

We again study the probability $P(t)$ of the atom excited by different kinds of photon wave-packets using Eq.(3.12), with the initial state of the total system being $|\psi(t_0)\rangle = |g, \psi_r, \psi_l, 0_s\rangle$, where the pulse states $|\psi_p\rangle = |\psi_r, \psi_l\rangle$. As a consequence of the initial vacuum state of the environment, the average values of the noise operators will vanish as $\langle \zeta \rangle = 0$.

4.2.1 Atomic excitation with Fock state pulses

In this part, we study the atomic excitation by multi-photon Fock state pulses with the help of Eqs.(4.8, 4.9) — the expectation value of atomic operator $\langle \sigma_z(t) \rangle$ with the initial state of the total

system $|g, n_r, n_l, 0_s\rangle$, which will further depend on different state-dependent values of $\langle\sigma_{\pm}(t)\rangle$.

Let us define the following variables

$$X_{n_r n_l, n_r n_l} = \langle g, n_r, n_l, 0_s | \sigma_z(t) | g, n_r, n_l, 0_s \rangle, \quad (4.10a)$$

$$Y_{n_r n_l, n_r n_l} = \langle g, n_r, n_l, 0_s | \sigma_-(t) | g, n_r, n_l, 0_s \rangle, \quad (4.10b)$$

$$Z_{n_r n_l, n_r n_l} = \langle g, n_r, n_l, 0_s | \sigma_+(t) | g, n_r, n_l, 0_s \rangle. \quad (4.10c)$$

Using the property of the action of the field operator on the Fock state

$$a_{i,j} |n_j\rangle = \sqrt{n_j} \xi_j(t) |n_j - 1\rangle, \quad (4.11)$$

and $\langle\zeta\rangle = 0$ as the environment is initially in the vacuum state, one finds a set of recursive differential equations,

$$\begin{aligned}\dot{X}_{n_r n_l, n_r n_l} &= -\gamma_0 (X_{n_r n_l, n_r n_l} + 1) \\ &\quad - 2\sqrt{\gamma_r n_r} \xi_r(t) (Y_{(n_r-1)n_l, n_r n_l} + Z_{n_r n_l, (n_r-1)n_l}) \\ &\quad - 2\sqrt{\gamma_l n_l} \xi_l(t) (Y_{n_r, (n_l-1), n_r n_l} + Z_{n_r n_l, n_r(n_l-1)}),\end{aligned}\quad (4.12a)$$

$$\begin{aligned}\dot{Y}_{(n_r-1)n_l, n_r n_l} &= -\frac{\gamma_0}{2} Y_{(n_r-1)n_l, n_r n_l} \\ &\quad + \sqrt{\gamma_r n_r} \xi_r(t) X_{(n_r-1)n_l, (n_r-1)n_l} \\ &\quad + \sqrt{\gamma_l n_l} \xi_l(t) X_{(n_r-1)n_l, n_r(n_l-1)},\end{aligned}\quad (4.12b)$$

$$\begin{aligned}\dot{Y}_{n_r, (n_l-1), n_r n_l} &= -\frac{\gamma_0}{2} Y_{n_r, (n_l-1), n_r n_l} \\ &\quad + \sqrt{\gamma_r n_r} \xi_r(t) X_{n_r, (n_l-1), (n_r-1)n_l} \\ &\quad + \sqrt{\gamma_l n_l} \xi_l(t) X_{n_r, (n_l-1), n_r(n_l-1)},\end{aligned}\quad (4.12c)$$

$$\begin{aligned}\dot{Z}_{n_r n_l, (n_r-1)n_l} &= -\frac{\gamma_0}{2} Z_{n_r n_l, (n_r-1)n_l} \\ &\quad + \sqrt{\gamma_r n_r} \xi_r(t) X_{(n_r-1)n_l, (n_r-1)n_l} \\ &\quad + \sqrt{\gamma_l n_l} \xi_l(t) X_{n_r, (n_l-1), (n_r-1)n_l},\end{aligned}\quad (4.12d)$$

$$\begin{aligned}\dot{Z}_{n_r n_l, n_r(n_l-1)} &= -\frac{\gamma_0}{2} Z_{n_r n_l, n_r(n_l-1)} \\ &\quad + \sqrt{\gamma_r n_r} \xi_r(t) X_{(n_r-1)n_l, n_r(n_l-1)} \\ &\quad + \sqrt{\gamma_l n_l} \xi_l(t) X_{n_r, (n_l-1), n_r(n_l-1)},\end{aligned}\quad (4.12e)$$

$$\vdots$$

$$X_{0,0_l,0,0_l} = -1, \quad (4.12f)$$

with the initial conditions

$$X_{n_r n_l, n_r n_l}(t_0) = -1, \quad (4.13a)$$

$$Y_{n_r n_l, n_r n_l}(t_0) = Z_{n_r n_l, n_r n_l}(t_0) = 0. \quad (4.13b)$$

4.2.2 Atomic excitation with coherent state pulses

Similarly, we can study the atomic evolution with two counter-propagating pulses in coherent state $|\alpha_r, \alpha_l\rangle$, which have the property that

$$a_{t,r} |\alpha_r\rangle = \alpha_r \xi_r(t) |\alpha_r\rangle, \quad (4.14a)$$

$$a_{t,l} |\alpha_l\rangle = \alpha_l \xi_l(t) |\alpha_l\rangle. \quad (4.14b)$$

Since we are interested only in the interference effect between two spatial-mode fields, the above expressions can be written with the following replacements,

$$\alpha_r = \sqrt{\bar{n}_r}, \quad \alpha_l = \sqrt{\bar{n}_l} \cdot e^{i\phi}, \quad (4.15)$$

where ϕ is the initial relative phase between the $|\alpha_r\rangle$ and $|\alpha_l\rangle$.

It is worth mentioning that, in principle, the temporal envelope of pulse $\xi_{r,l}(t)$ is a complex function. Here, we assume that the global phase factors are included in the coefficients $\alpha_{r,l}$ and $\xi_{r,l}(t)$ are real.

Again, by taking the average values of Eqs.(4.8, 4.9) on the initial state $|\psi(t_0)\rangle = |g, \alpha_r, \alpha_l, 0_s\rangle$, we have the following differential equations

$$\begin{aligned} \dot{X}_{\alpha_r, \alpha_l, \alpha_r, \alpha_l} &= -\gamma_0 (X_{\alpha_r, \alpha_l, \alpha_r, \alpha_l} + 1) \\ &\quad - 2\sqrt{\gamma_r \bar{n}_r} \xi_r(t) (Y_{\alpha_r, \alpha_l, \alpha_r, \alpha_l} + Z_{\alpha_r, \alpha_l, \alpha_r, \alpha_l}) \\ &\quad - 2\sqrt{\gamma_l \bar{n}_l} \xi_l(t) (e^{-i\phi} Y_{\alpha_r, \alpha_l, \alpha_r, \alpha_l} + e^{i\phi} Z_{\alpha_r, \alpha_l, \alpha_r, \alpha_l}), \end{aligned} \quad (4.16a)$$

$$\begin{aligned} \dot{Y}_{\alpha_r, \alpha_l, \alpha_r, \alpha_l} &= -\frac{\gamma_0}{2} Y_{\alpha_r, \alpha_l, \alpha_r, \alpha_l} \\ &\quad + \left(\sqrt{\gamma_r \bar{n}_r} \xi_r(t) + e^{i\phi} \sqrt{\gamma_l \bar{n}_l} \xi_l(t) \right) X_{\alpha_r, \alpha_l, \alpha_r, \alpha_l}, \end{aligned} \quad (4.16b)$$

$$\begin{aligned} \dot{Z}_{\alpha_r, \alpha_l, \alpha_r, \alpha_l} &= -\frac{\gamma_0}{2} Z_{\alpha_r, \alpha_l, \alpha_r, \alpha_l} \\ &\quad + \left(\sqrt{\gamma_r \bar{n}_r} \xi_r(t) + e^{-i\phi} \sqrt{\gamma_l \bar{n}_l} \xi_l(t) \right) X_{\alpha_r, \alpha_l, \alpha_r, \alpha_l}, \end{aligned} \quad (4.16c)$$

with

$$X_{\alpha_r, \alpha_l, \alpha_r, \alpha_l} = \langle g, \alpha_r, \alpha_l, 0_s | \sigma_z(t) | g, \alpha_r, \alpha_l, 0_s \rangle, \quad (4.17a)$$

$$Y_{\alpha_r, \alpha_l, \alpha_r, \alpha_l} = \langle g, \alpha_r, \alpha_l, 0_s | \sigma_-(t) | g, \alpha_r, \alpha_l, 0_s \rangle, \quad (4.17b)$$

$$Z_{\alpha_r, \alpha_l, \alpha_r, \alpha_l} = \langle g, \alpha_r, \alpha_l, 0_s | \sigma_+(t) | g, \alpha_r, \alpha_l, 0_s \rangle, \quad (4.17c)$$

and the initial conditions

$$X_{\alpha_r, \alpha_l, \alpha_r, \alpha_l}(t_0) = -1, \quad (4.18a)$$

$$Y_{\alpha_r, \alpha_l, \alpha_r, \alpha_l}(t_0) = Z_{\alpha_r, \alpha_l, \alpha_r, \alpha_l}(t_0) = 0. \quad (4.18b)$$

4.2.3 Even- and odd-parity modes

For better understanding of the atomic dynamics with two spatial-mode pulses, let us introduce even- and odd-parity mode operators as the combination of the right- and left-propagating modes

$$b_{\omega, e}^\dagger = \frac{a_{\omega, l}^\dagger + a_{\omega, r}^\dagger}{\sqrt{2}}, \quad b_{\omega, o}^\dagger = \frac{a_{\omega, l}^\dagger - a_{\omega, r}^\dagger}{\sqrt{2}}. \quad (4.19)$$

The Fock state pulse in the even-mode is thus given by

$$|n_e\rangle = \frac{1}{\sqrt{n_e!}} (B_e^\dagger)^{n_e} |0_r, 0_l\rangle, \quad (4.20)$$

where the wave-packet creation operator for the even-mode is

$$B_e^\dagger = \int dt \xi_e(t) b_{t, e}^\dagger = \int d\omega f_e(\omega) b_{\omega, e}^\dagger. \quad (4.21)$$

Accordingly, the coherent state pulse in the even-mode is

$$\begin{aligned}
|\alpha_e\rangle &= D_e(\alpha_e) |0_r, 0_l\rangle \\
&= \exp[\alpha_e B_e^\dagger - \alpha_e^* B_e] |0_r, 0_l\rangle \\
&= \exp\left[\frac{\alpha_e A_r^\dagger - \alpha_e^* A_r}{\sqrt{2}}\right] \exp\left[\frac{\alpha_e A_l^\dagger - \alpha_e^* A_l}{\sqrt{2}}\right] |0_r, 0_l\rangle \\
&= \left| \frac{1}{\sqrt{2}}\alpha_e, \frac{1}{\sqrt{2}}\alpha_e \right\rangle.
\end{aligned} \tag{4.22}$$

For a specific case of single-photon in the even-mode, we have

$$|1_e\rangle = B_e^\dagger |0_r, 0_l\rangle = \frac{1}{\sqrt{2}} (|1_r, 0_l\rangle + |0_r, 1_l\rangle), \tag{4.23}$$

for Fock state pulse and

$$|\alpha_e\rangle = \left| \frac{1}{\sqrt{2}}\alpha_e, \frac{1}{\sqrt{2}}\alpha_e \right\rangle, \quad \bar{n}_e = |\alpha_e|^2 = 1, \tag{4.24}$$

for coherent state pulse.

Since we consider only the situation when the two pulses come symmetrically to the atom, and set $z_a = 0$, the interaction Hamiltonian Eq.(4.1) can thus be rewritten as

$$\hat{H}_I(t) = -i\hbar \sqrt{\frac{\gamma_r}{\pi}} \int d\omega [\sigma_+ b_{\omega,e} e^{-i(\omega-\omega_a)t} - h.c.], \tag{4.25}$$

where we have used the property of $|g_{\omega,j}\rangle \approx |g_{\omega_a,j}\rangle = \sqrt{\frac{\gamma_r}{2\pi}} = \sqrt{\frac{\gamma_l}{2\pi}}$ under Weisskopf-Wigner approximation and the assumption of equivalent decay into the right and left channels. It can be seen from Eq.(4.25) that when the right and left pulses are incident symmetrically to the atom located at $z_a = 0$, only photons in the even-mode interact with the atom and thus contribute to the atomic inversion process, and the odd-mode photons are interaction-free.

4.3 Numerical simulation for different photon states

In this section, we will use the above formalism for Fock state pulses Eq.(4.12) and coherent state pulses Eq.(4.16) to study the interaction between the two spatial-mode pulses incident on

the atom. For this purpose, we consider three distinct cases:

- (i) *single-photon excitation* — total photon excitation number is one for different spatial-modes;
- (ii) *multi-photon excitation* — arbitrary n -photon in the even-mode;
- (iii) *two spatial-mode pulses interference* — n -photon in two distinct spatial-modes.

Numerical simulation is done with specific pulse temporal shapes — the rectangular shape and rising exponential shape as defined in Table.(3.1). For simplicity, we assume a symmetric two spatial-mode structure — no decay to the environment $\gamma' = 0$ and equivalent decay to the right and left channel $\gamma_r = \gamma_l = \gamma_0/2$.

4.3.1 Single-photon excitation

In this part, we consider atomic excitation with total photon number one for both Fock state and coherent state pulses in two cases: (a) single-photon in single spatial-mode — $|1_r, 0_l\rangle$ and $|\alpha_r, 0_l\rangle$ with $\bar{n}_r = 1$, as seen in Fig.(4.1)(b). (b) single-photon in the even-mode, $|1_e\rangle$ and $|\alpha_e\rangle$ with $\bar{n}_e = 1$, as in Fig.(4.1)(c).

In Fig.(4.2), we show the dependence of the maximum achievable excitation probability P_{max} on the pulse bandwidth Ω for different photon states with a rising exponential temporal shape. We find out that for Fock state pulse $|1_r, 0_l\rangle$ (red solid curve), the maximum excitation probability $P_{max} = 0.5$, and it goes up to $P_{max} = 1$ for a single-photon in the even-parity mode $|1_e\rangle$ (black solid curve), with the same optimum pulse bandwidth $\Omega = \gamma_0$. This is not surprising since the photon in the single spatial-mode (left or right) has half probability of being in the odd-mode, which doesn't interact with the atom. Another explanation is that the photon in single spatial-mode cannot cover the whole dynamics in this two spatial-mode description of the atom-pulses interaction, because of the atomic relaxation into the other channel. This observation simply agrees with the time-reversed spontaneous emission argument. The sufficient condition for a two-level atom to be fully excited by a single-photon is that the single-photon has to be rising-exponentially shaped in Fock state in addition to perfect spatial-mode matching with the atomic dipole [56].

For single-photon coherent state (dashed curves), the maximum excitation probability is $P_{max} = 0.37$ for the photon being in a single spatial-mode $|\alpha_r, 0_l\rangle$ with the optimum bandwidth being $\Omega = 1.36\gamma_0$ (red dashed curve) and $P_{max} = 0.56$ for the photon being in the even-mode $|\alpha_e\rangle$

with $\Omega = 1.9\gamma_0$ (black dashed curve). The atomic excitation $P(t)$ as a function of time for rising exponential pulse with optimum bandwidth is given in Fig.(4.3). One can see that for Fock and coherent state pulses, it takes almost the same time — on the order of atomic lifetime to achieve the maximum atomic excitation.

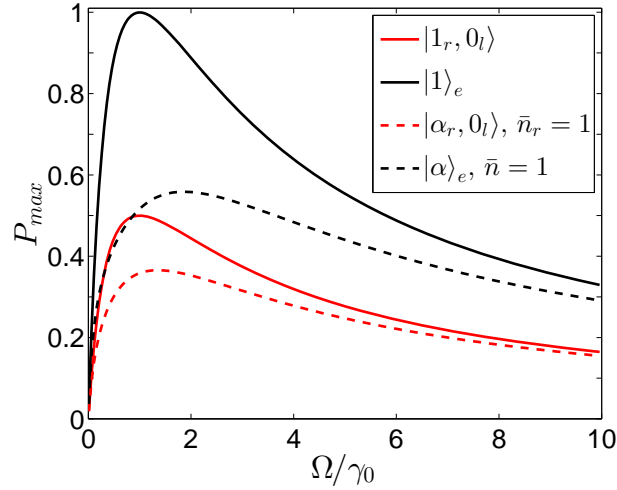


Figure 4.2: Dependence of maximum excitation probability P_{max} on pulse bandwidth with initial rising exponential shape for single-photon Fock state (solid curves) and coherent state (dashed curves) in the right-propagating mode (red curves) and the even-mode (black curves), respectively. Full atomic excitation by single-photon pulse can only be realized when it is rising-exponential shaped in the even-parity mode Fock state $|1_e\rangle$. The excitation probability is bounded by 0.5 if the single-photon only occupies single spatial-mode $|1_r, 0_l\rangle$.

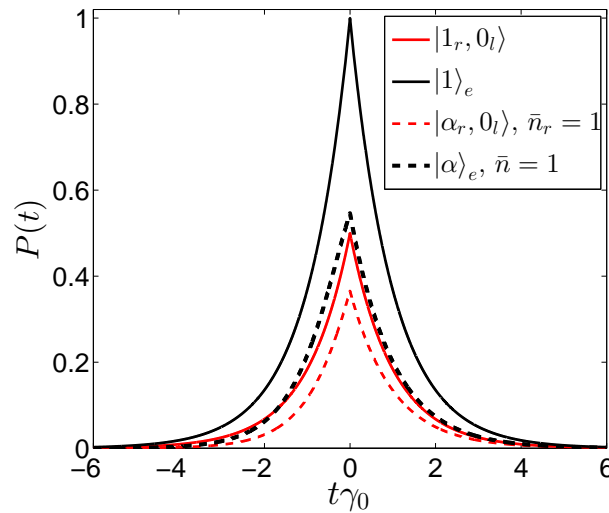


Figure 4.3: Atomic excitation probability $P(t)$ as a function of time with initial rising exponential pulses prepared in their optimum bandwidths for Fock state (solid curves) and coherent state (dashed curves) in the right-propagating mode (red curves) and the even-mode (black curves), respectively.

4.3.2 Multi-photon excitation

Here we consider the case of n photons in the even parity-mode interacting with the atom, schematically shown in Fig.(4.1)(c). We perform a numerical study for both Fock state and coherent state pulses with photon number ranging over $n \in [1, 10]$.

In Fig.(4.4), excitation probability as a function of time with initial rectangular-shaped pulses in the even-mode for different bandwidths $\Omega/\gamma_0 = \{0.1, 0.8, 1.5, 10\}$ and with photon numbers $n = \{1, \dots, 5\}$ is plotted. As expected, higher excitation is obtained with bandwidth close to the atomic linewidth $\Omega \approx \gamma_0$ and it takes shorter time to reach the maximum excitation for broader pulses. It is interesting to compare the Fock state cases (left column) and coherent state cases (right column) in Fig.(4.4). For bandwidth set $\Omega/\gamma_0 = \{0.1, 0.8, 1.5, 10\}$, maximum excitation probability P_{max} is always ordered by photon number for coherent state pulses. But for Fock state pulses, P_{max} is ordered by photon number only for narrow and broad bandwidths $\Omega/\gamma_0 = \{0.1, 10\}$, not for the intermediate bandwidths $\Omega/\gamma_0 = \{0.8, 1.5\}$. For $\Omega/\gamma_0 = 0.8$, single-photon yields a better atomic excitation than higher photon number pulses and for $\Omega/\gamma_0 = 1.5$, two-photon excitation is better than the others. This effect can be seen more clearly from Fig.(4.5), where the maximum excitation probability versus photon number for different bandwidths $\Omega/\gamma_0 = \{0.1, 0.8, 1.5, 10\}$ is plotted. For Fock state pulse with bandwidths $\Omega/\gamma_0 = \{0.1, 10\}$, P_{max} increases monotonically with the photon number n , as shown in Fig.(4.5(a)). This is not true for $\Omega/\gamma_0 = \{0.8, 1.5\}$, where one can see a dip or peak at $n = 2$ in the corresponding curves. For coherent state pulses shown in Fig.(4.5(b)), P_{max} increases monotonically with the average photon number \bar{n} . It can also be seen from Fig.(4.4) that for both cases, atomic excitation increases faster for broader bandwidth ($\Omega/\gamma_0 = 10$) before saturation. This can be understood from the fact that in a short-pulse limit — pulse with duration far shorter than atomic lifetime, the spontaneous emission effect can be ignored. It is worth mentioning that Rabi oscillation can be seen with higher photon numbers in both cases.

We further study the optimum bandwidth for different photon-number pulses. Numerical simulation with rectangular-shaped pulse is shown in Fig.(4.6) for $n \in [1, 5]$. As expected, in the Fock state case Fig.(4.6(a)), there are several crossings between lines for different photon numbers contrary to the coherent state case Fig.(4.6(b)) with no line-crossings. For Fock state pulse with a given bandwidth, there is indeed a preferred photon number that maximizes the

excitation probability and vice versa. But for coherent state pulses, higher photon number always gives higher maximal excitation probability before saturation.

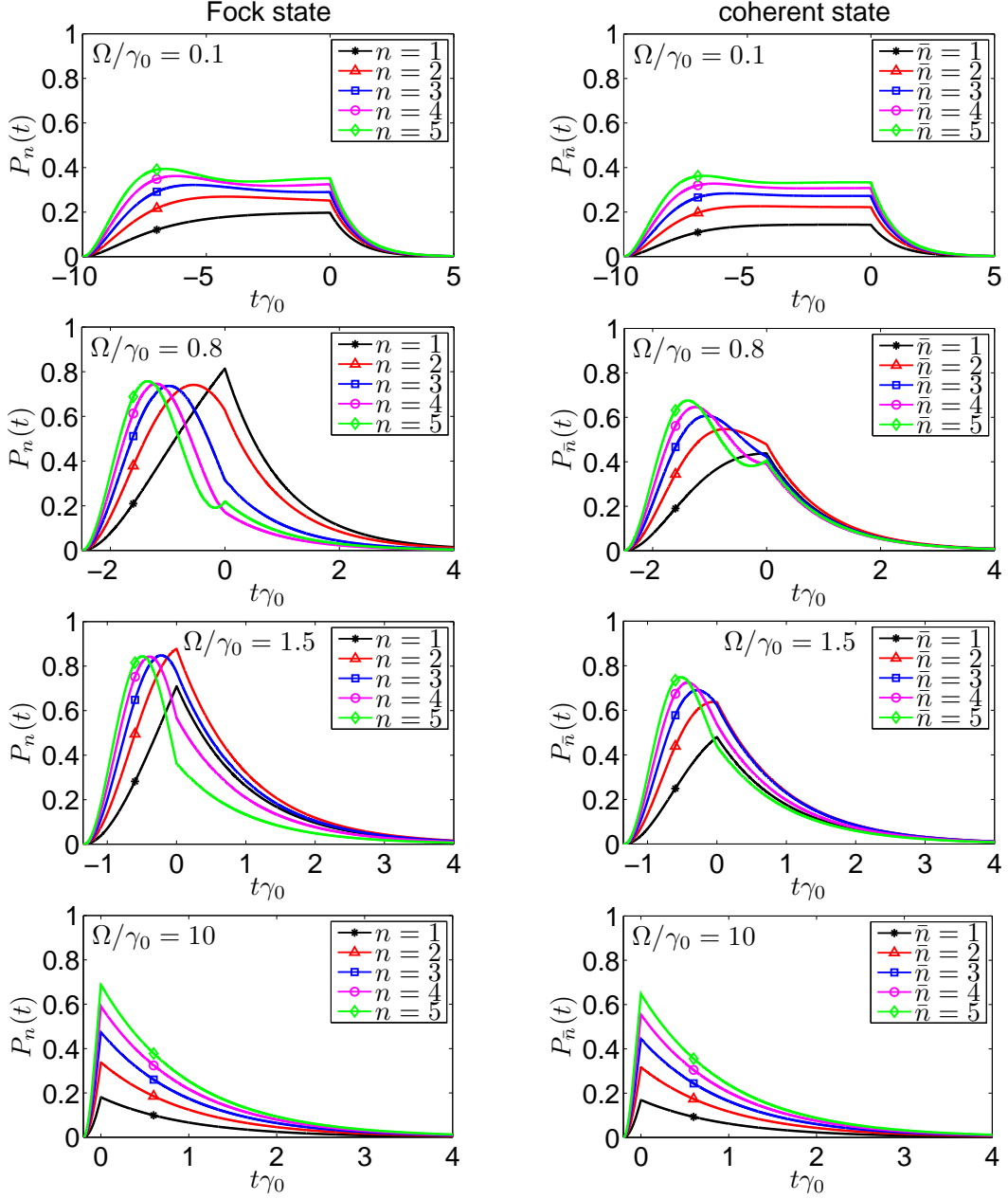


Figure 4.4: Atomic excitation probability $P(t)$ as a function of time with the initial rectangular-shaped pulse for different bandwidths $\Omega/\gamma_0 = \{0.1, 0.8, 1.5, 10\}$ and different photon numbers $n, \bar{n} \in [1, 5]$ in the even-mode. For coherent state pulses (right column), the maximum excitation probability P_{max} is always ordered by average photon number \bar{n} for arbitrary bandwidth. This is not the case for Fock state (left column) in general, namely for bandwidths $\Omega/\gamma_0 = \{0.8, 1.5\}$.

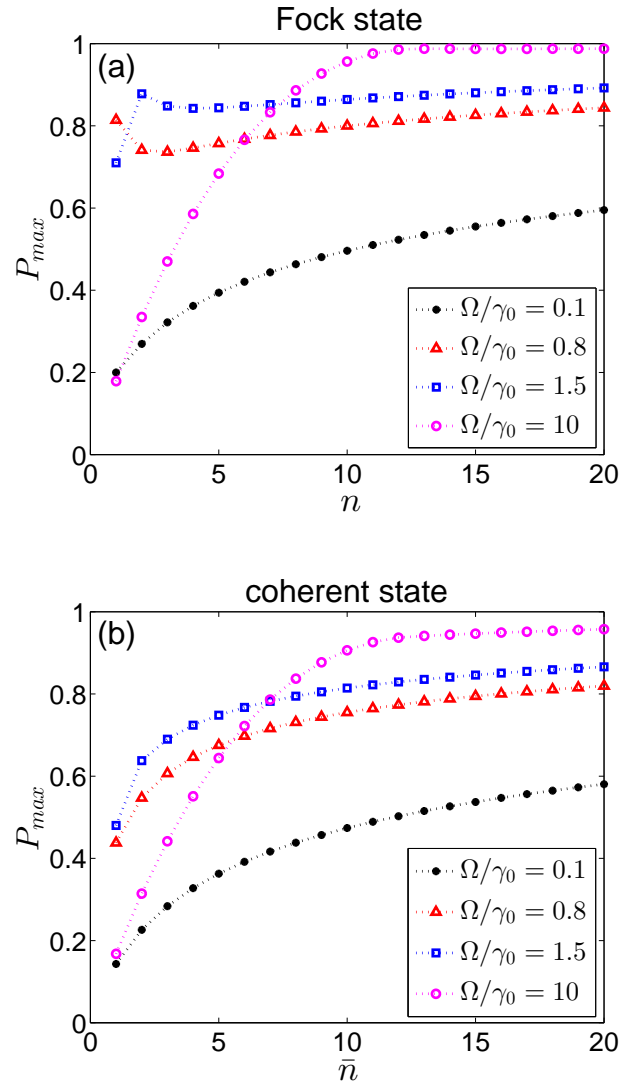


Figure 4.5: Maximum excitation probability P_{max} as a function of photon number with initial rectangular-shaped pulses in (a) Fock state (b) coherent state for different bandwidths $\Omega/\gamma_0 = \{0.1, 0.8, 1.5, 10\}$, respectively. P_{max} increases monotonically with the photon number \bar{n} for coherent state case (b). This is not the case for Fock state pulses with bandwidths $\Omega/\gamma_0 = 0.8$ (1.5), where there is a dip (a peak) at $n = 2$.

4.3.3 Interference of pulses in two distinct spatial-modes

Let us consider two counter-propagating pulses incident simultaneously on a two-level atom, schematically shown in Fig.(4.1)(d). We consider the pulses being either in Fock state or in coherent state.

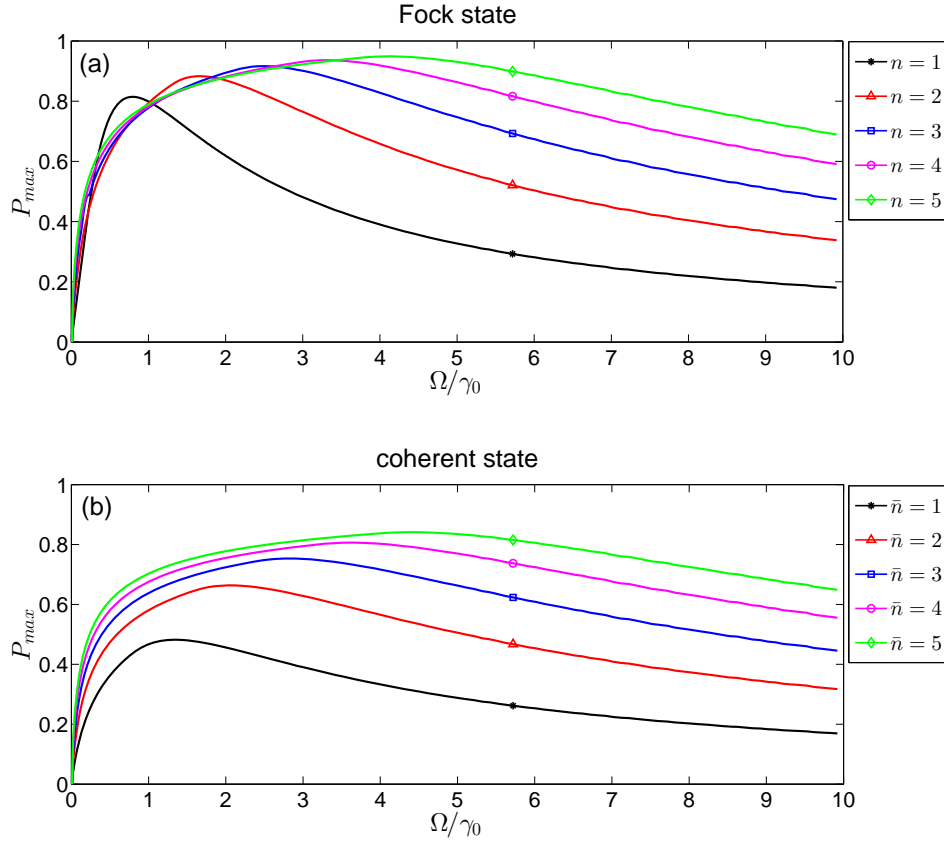


Figure 4.6: Maximum atomic excitation probability P_{max} as a function of bandwidth Ω/γ_0 with initially rectangular-shaped pulse in the even-mode for different photon numbers. The crossings in Fock state case (a) implies that for a given bandwidth there is a optimal photon number which maximizes the excitation probability. For coherent state pulses (b), higher photon number always yields higher P_{max} for arbitrary bandwidths before saturation.

Two-mode Fock state pulse

Firstly, we consider the action of two single-photon Fock state pulses incident on the two-level atom. This corresponds to an initial state $|\psi(t_0)\rangle = |g, 1_r, 1_l, 0_s\rangle$ of the total system. We assume the same rectangular temporal shape for the two pulses. The relative phase for Fock state pulses is undefined in the sense that the global phases of the two Fock state pulses don't have any effect on the atomic dynamics [108, 109, p.73]. An interesting consequence is that in the case of two single photon Fock state pulses, a small change of the atomic position doesn't influence the atomic dynamics. By small change, we mean a change in the atomic position on the order of $m\lambda$ with m being integer, provided it is much smaller than the typical length of the Fourier limited pulse, such that $m\lambda \ll l_c$. This means that the two pulses are still incident onto the atom in an almost perfectly symmetrical way (i.e. the two pulses are still indistinguishable to the atom).

This is in contrast to the two coherent state pulses where a small change on the order of λ in the atomic position change the atomic dynamics significantly due to the constructive or destructive interference (see also next paragraph). The dependence of atomic excitation on pulse bandwidth is given in Fig.(4.7(a)), and the excitation probability with time is given in Fig.(4.7(b)). We can see that two counter-propagating pulses with identical rectangular shape give slightly better excitation than the single-photon with the same shape, but the excitation is still bounded by 0.5 — which we verified using two counter-propagating rising-exponentially shaped pulses with optimal bandwidth. This can be easily understood since

$$|1_r, 1_l\rangle = \frac{|2_e, 0_o\rangle - |0_e, 2_o\rangle}{\sqrt{2}}, \quad (4.26)$$

which means there is a probability one half of no photon in the even-mode. This also explains

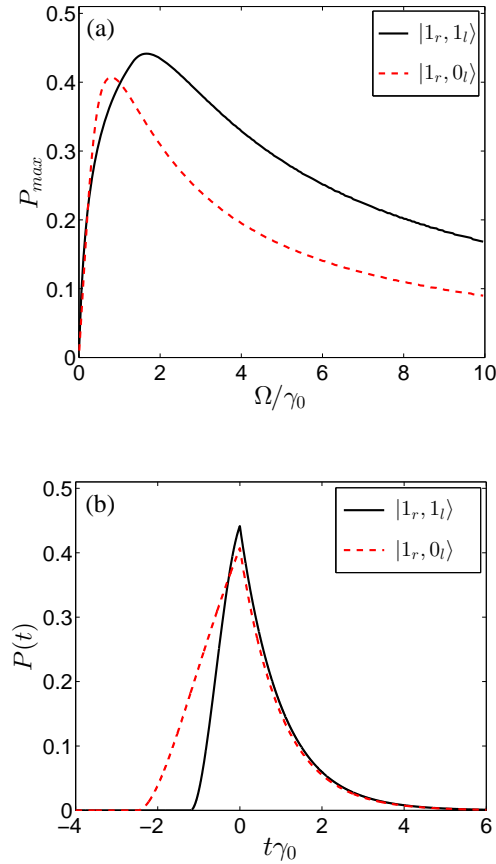


Figure 4.7: Atomic excitation with initially rectangular-shaped Fock state pulses in different states. (a) dependence of P_{max} on the pulse bandwidth. (b) time evolution of $P(t)$ for pulses with optimized bandwidth. The black solid line corresponds to the state $|1_r, 1_l\rangle$, and the red dashed line to the state $|1_r, 0_l\rangle$.

the faster excitation by the state $|1_r, 1_l\rangle$ (Fig.(4.7(b))) due to the simultaneous presence of the two photons instead of one as in state $|1_r, 0_l\rangle$. It is worth mentioning that, the state

$$\frac{|2_r, 0_l\rangle + |0_r, 2_l\rangle}{\sqrt{2}} = \frac{|2_e, 0_o\rangle + |0_e, 2_o\rangle}{\sqrt{2}}, \quad (4.27)$$

gives the same atomic excitation as the state $|1_r, 1_l\rangle$, which is clear because those two states have the same even-mode component, which is the only component contributing to the atomic excitation.

Two-mode coherent state pulse

It is easy to recognize from Eqs.(4.16) that for coherent state pulses, the appearance of the relative phase ϕ between the counter-propagating pulses gives rise to interference effects. To have better excitation of the atom, the counter-propagating pulses must interference constructively. In a particular case, for the two pulses with the same average photon number $\bar{n}_r = \bar{n}_l$ and relative phase difference $\phi = \pi$, the atom looks transparent to the two pulses, which propagate freely and won't be affected by the atom.

A simple application of the coherent state pulses interference effect is that the atomic excitation can be controlled by not only the mean photon number $\bar{n}_{r,l}$ but also the relative phase ϕ . The maximum excitation probability P_{max} varies as a function of the mean photon number \bar{n}_r in the right-propagating mode for different relative phases $\phi = \{0, \pi, \pi/2\}$ as shown in Fig.(4.8) with

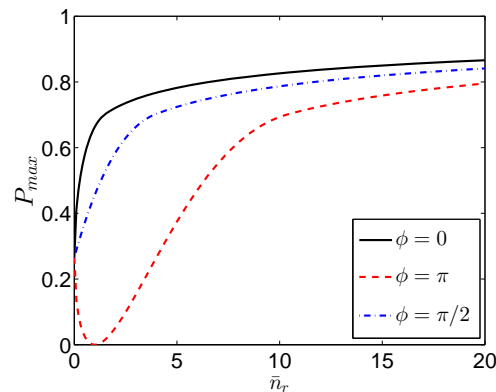


Figure 4.8: Maximum excitation probability P_{max} as a function of mean photon number \bar{n}_r in the right-propagating mode for different relative phases $\phi = \{0, \pi, \pi/2\}$ with average photon number one $\bar{n}_l = 1$ in the left-propagating mode. The two pulses have the same rectangular shape with $\Omega = 2\gamma_0$, which is the optimum bandwidth for $\bar{n}_r = \bar{n}_l = 1$.

$\bar{n}_l = 1$. For two pulses with the same phase $\phi = 0$ (black solid line), P_{max} increases monotonically with the photon number in the right-propagating mode; for two pulses with the opposite phase $\phi = \pi$ (blue dashed line), a completely destructive interference happens for the same average photon number in the two spatial-modes $\bar{n}_r = \bar{n}_l = 1$; for a phase difference of $\phi = \pi/2$ between the two pulses, a reduction of atomic excitation is observed (blue dash-dot line).

4.4 Experimental demonstration of atomic excitation with temporally shaped pulses

In this section, our theoretical prediction of the pulse effect on atomic excitation is examined by an experimental done in Christian Kurtsiefer's group in Centre for Quantum Technologies, Singapore. They experimentally investigate the effect of temporally shaped coherent state light pulses on the excitation probability of a closed cycling two-level transition in a single ^{87}Rb atom. The experiment is done with coherent states pulses generated from a continuous wave (CW) laser using an optical modulator.

4.4.1 The experimental setup

In the following, we give a brief description of the experiment setup and the detailed experimental procedures can be found in [110,111]. The experimental setup is schematically shown in Fig.(4.9). A single atom is trapped at the focus of two confocally positioned aspheric lenses in a far-off resonant optical dipole trap (FORT), which is loaded from a magneto-optical trap (MOT) holding $\approx 10^4$ atoms. The collision blockade mechanism ensures that either zero or one atom is in a trap at any instance [112].

The temporally shaped probe pulse is focused onto the atom and thus gives rise to strong atom-pulse interaction, as demonstrated from the CW laser extinction measurement experiment in 2008 [60] as well as the phase shift measurement experiment in 2009 [113]. Two typical pulse shapes used in this experiment are in the rectangular and rising exponential form. Full description of the generation of the temporal shape controlled coherent state pulses can be found in [114]. The parameters that are varied in this experiment were the average photon number per pulse and the bandwidth for both rectangular and exponential pulse shapes. The average photon number

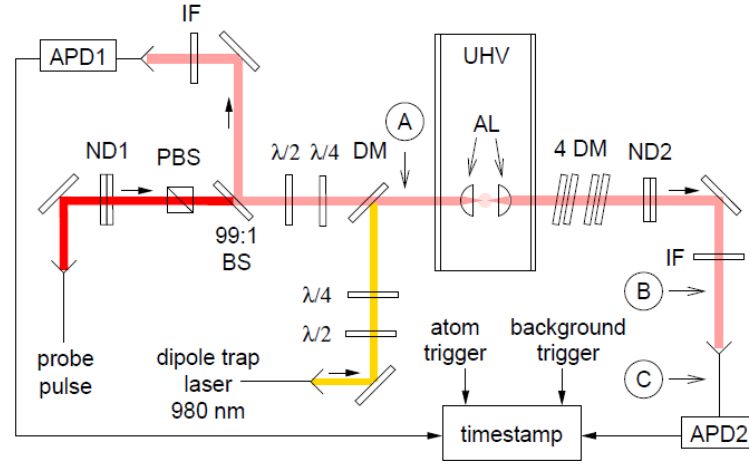


Figure 4.9: Setup for the pulsed excitation experiment. UHV: ultra high vacuum chamber, AL: aspheric lenses with full $NA = 0.55$ and focal length $f = 4.51$ mm, PBS: polarizing beam splitter, ND1(2): stacks of neutral density filters, λ/n : wave plates, DM: dichroic mirrors, IF: interference bandpass filters centered at 780 nm, FWHM 1 nm.

per pulse is controlled by the calibrated neutral density filters (ND1).

The two avalanche photodiode APD1 and APD2 are operating in photon counting mode to collect the backward and forward scattered light, respectively. Both photodiode signals, and a reference signal for the optical excitation pulses are time-stamped with a resolution below 1 ns for further analysis.

The two-level system in a rubidium atom

The ^{87}Rb is an isotope of rubidium with atomic number 37, mass of 86.9 amu and nuclear spin $I = 3/2$. In the spectroscopic notation, an atomic level is described as

$$n^{2S+1}L_J |F, m_F\rangle, \quad (4.28)$$

where n is the principal quantum number; L and S are the electronic orbital and spin angular momentum, respectively; $J = L + S$ is the total nuclear angular momentum; $F = J + I$ is the total angular momentum quantum number for the hyperfine structure that arises from the coupling between the magnetic moment of the electron and the nuclear magnetic moment; m_F is the magnetic quantum number.

For the dipole allowed transitions in ^{87}Rb , the states $|g_{\pm}\rangle = 5S_{1/2} |F = 2, m_F = \pm 2\rangle$ and $|e_{\pm}\rangle = 5P_{3/2} |F = 3, m_F = \pm 3\rangle$ can serve as a closed cycling two-level system with a life time of

$1/\gamma_0 = 26.29 \pm 0.05$ ns, as shown in Fig.(4.10).

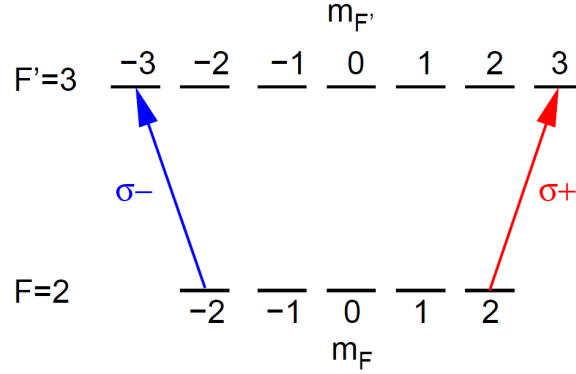


Figure 4.10: Energy structure of the ^{87}Rb atom used in the pulsed excitation experiment.

4.4.2 The results

To compare with the formalism in Sec.(4.2.2), the experiment is designed to investigate the atomic excitation with rising exponential shape

$$\xi_{exp}(t) = \begin{cases} \sqrt{\Omega} \exp\left(\frac{\Omega}{2} t\right), & : \text{ for } t < 0 \\ 0, & : \text{ for } t > 0 \end{cases} \quad (4.29)$$

and rectangular shape

$$\xi_{rect}(t) = \begin{cases} \sqrt{\Omega}, & : \text{ for } -\frac{1}{\Omega} \leq t \leq 0 \\ 0, & : \text{ else} \end{cases} \quad (4.30)$$

where Ω is the frequency bandwidth of the pulses.

With a two-level atom, the excited state population is directly related to the atomic scattering, which is detected in the backwards direction with detector APD1 in this experiment. The photo-detection events is sorted into time bins of widths $\Delta t = 1$ ns with respect to the pulses edge while the excitation pulse passes along the atom for a number of N_T pulses with confirmed presence of the atom in the focus.

In the following, we show the experiment results with comparison to theoretical predications in terms of three quantities: the excited state population as a function of time — $P(t)$; the maximum excited state population during the whole excitation process — P_{max} , and the excited state population when the pulse is finished — $P(t_e)$.

The excited state population — $P(t)$

The excited state probability $P(t)$ can be directly assessed by the probability $P_d(t)$ of detecting an event in backwards direction with APD1 in time bin Δt per trigger

$$P_d(t) = \frac{N_d(t)}{N_T} = \gamma_p P(t) \Delta t \eta_f, \quad (4.31)$$

where $N_d(t)$ is the number of detected events in the time bin t , $\gamma_p P(t)$ is the corresponding rate at which the atom scatters photons into the solid angle extended by the collection optics; $\eta_f = 0.3 \pm 0.02$ is a product of the detector APD1 efficiency and the transmission from the atom through all optical components to detector APD1. Thus the excited state probability reads

$$P(t) = \frac{N_d(t)}{\gamma_p \Delta t \eta_f N_T}, \quad (4.32)$$

where γ_p is proportional to the spontaneous emission rate γ_0 as $\gamma_p = \eta_p \gamma_0$. In this particular experimental configuration, the spatial overlap factor η_p has been studied and expressed in terms of the scattering ratio R_{sc} , which further depends on the focusing strength $u := w_L/f$ as [107]

$$\eta_p = \frac{\Lambda}{8\pi/3} = \frac{R_{sc}}{4} = \frac{3}{16u^3} e^{2/u^2} \left[\Gamma\left(-\frac{1}{4}, \frac{1}{u^2}\right) + u \Gamma\left(\frac{1}{4}, \frac{1}{u^2}\right) \right]^2, \quad (4.33)$$

where w_L is the input beam waist, f is the focal distance of the coupling lens, and $\Gamma(a, b) = \int_b^\infty t^{a-1} e^{-t} dt$ is the incomplete gamma function. For the focusing strength of $u = 0.22$ in our experiment, the spatial overlap is $\eta_p \approx 0.03$.

In Fig.(4.11), we show the dynamics of atomic excited state probability $P(t)$ as a function of time for both rising exponential (dashed-blue line) and rectangular shaped pulses (solid-red line) with a characteristic time of $\Omega^{-1} = 15\text{ns}$ and average photon number of $\bar{n} \simeq 1300$. The dotted-green lines are the theoretical curves obtained by numerically solving differential equations in Eq.(4.16). Rabi oscillations are clearly visible in the figures.

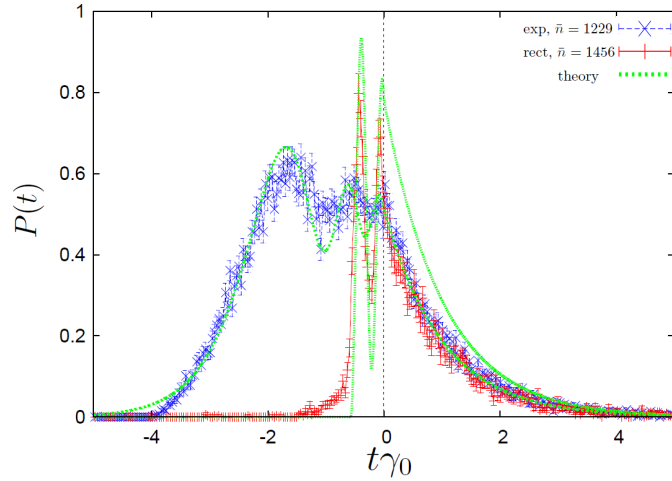


Figure 4.11: Excitation probability $P(t)$ as a function of time for pulses with a characteristic time of 15 ns and average photon number of $\bar{n} \approx 1300$.

The maximum excited state population — P_{max}

To further compare the atomic excitation with rising exponential and rectangular shaped pulses, the maximal excitation probability

$$P_{max} = \max_t P(t), \quad (4.34)$$

is plotted with respect to the average photon number \bar{n} for different bandwidths in Fig.(4.12).

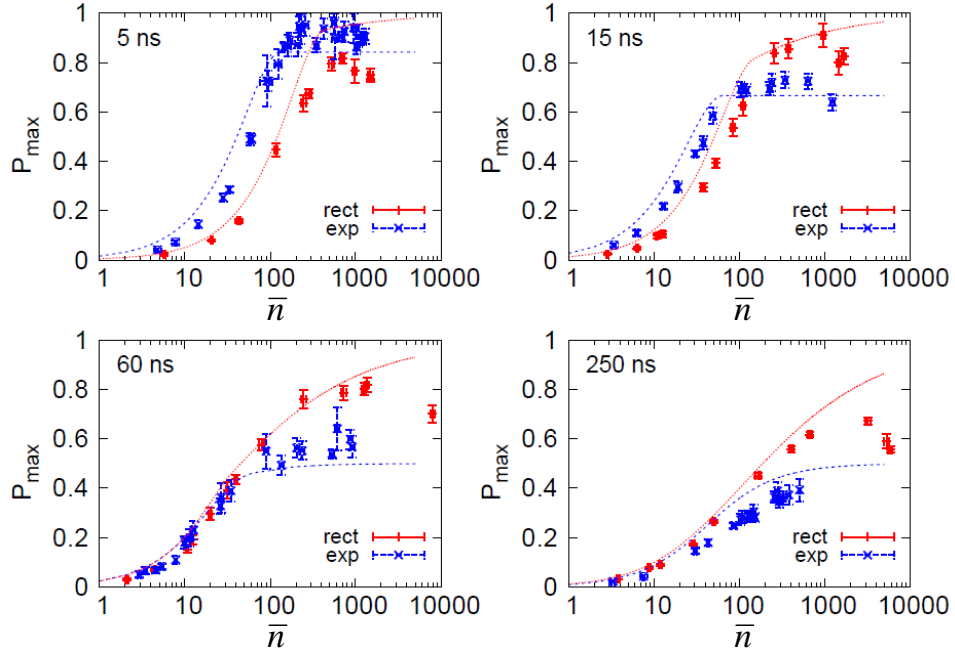


Figure 4.12: Maximal excitation probability P_{max} versus the average photon number for exponential (blue crosses) and rectangular (red circles) pulses with different pulse durations. The red and blue dashed lines corresponds to the theoretical plots.

It can be seen that, for shorter pulses of $\Omega^{-1} = 5, 15$ ns (broader frequency bandwidth) with smaller average photon number, the rising exponential pulse gives higher maximal excitation probability than the rectangular pulse in atomic excitation because the rising exponential pulse has a larger temporal/frequency overlap with the atomic emission pattern. For longer pulses $\Omega^{-1} = 60, 250$ ns (narrower frequency bandwidth) with smaller average photon number, there is not much difference between rising exponential and rectangular pulses. This is because when pulses are long enough, both pulses resemble the CW laser to the atom, and the atom cannot distinguish between the pulse shapes.

We can also see from the figure that as the pulses getting longer, it takes more photons to transfer the atom to the excited state. This is not surprising since the excited state population is determined by two competing effects — the excitation and the emission processes. For pulses with the same total energy, the power (energy/time) is smaller for longer pulses (vice versa) and thus result in weaker excitation compared with the shorter pulse with the same total energy. This also accounts for the another notable difference between the two pulse shapes on atomic excitation — with larger average photon numbers, the rectangular pulse always wins over the rising exponential pulse. For rising exponential pulse, it has a longer tail compared with the rectangular pulse, which means the atomic excitation process is weaker and slower. Longer spontaneous emission happens with the rising exponential pulse excitation. Comparably the rectangular pulse has a sharp edge, so that the beginning of the pulse is always sufficient to excite the atom with a large population. Much more obvious difference is expected with Fock state pulses and increased spatial overlap.

The excited state population when the pulse is finished — $P(t_e)$

The excitation probability $P(t_e)$ at time t_e , when the pulse is finished, can be extracted by summing up all the discrete bins from t_e to ∞ with time step of Δt ,

$$P(t_e) = \gamma_0 \Delta t \sum_{i=0}^{\infty} P_i. \quad (4.35)$$

To have a better insight into the atomic dynamics with various parameters of the pulses, we

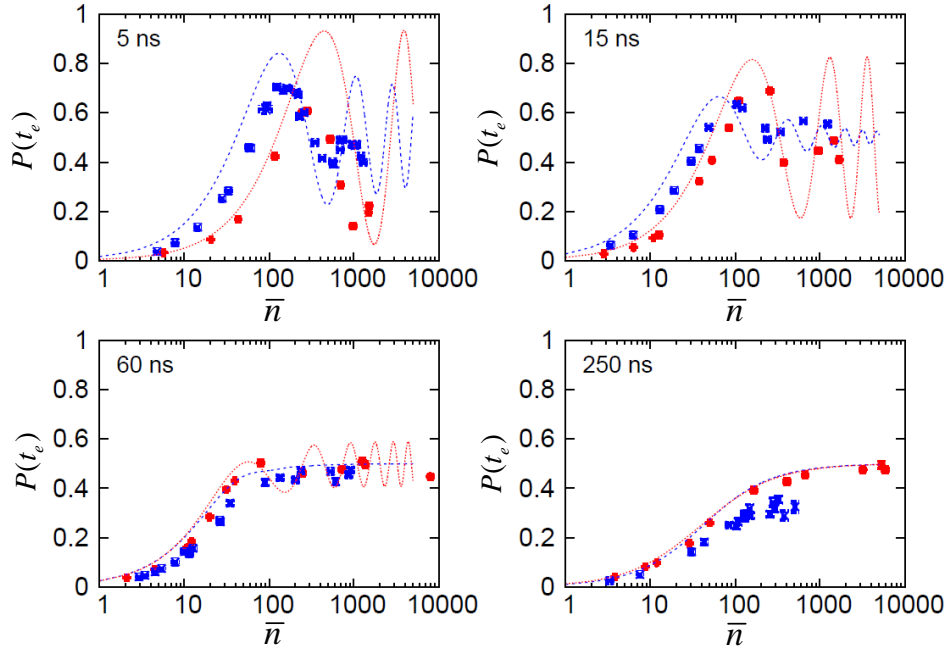


Figure 4.13: Excitation probability $P(t_e)$ versus the average photon number for exponential (blue crosses) and rectangular (red circles) pulses with different pulse durations. The red and blue dashed lines correspond to the theoretical plots.

plot $P(t_e)$ as a function of average photon number \bar{n} for both rising exponential and rectangular shaped pulses with different bandwidths in Fig.(4.13). Although the datapoints do not fit precisely to the theoretical curves, the trend of the experimental data points is clearly similar to that of theory. Oscillations are clearly visible for both rising exponential and rectangular pulses for shorter pulses (large bandwidths). For longer pulses ($\Omega^{-1} = 60$ ns and $\Omega^{-1} = 250$ ns), the magnitude of the coherent oscillations is getting smaller and especially for $\Omega^{-1} = 250$ ns pulses, no oscillations are visible for the reason that the longer pulses resemble the CW laser and the atom is getting saturated around $P(t_e) = 0.5$.

Quantum memory with a single two-level atom in a half cavity

In this chapter, we propose a setup for quantum memory based on a single two-level atom in a half cavity with a moving mirror. We show that various temporal shapes of incident photon can be efficiently stored and readout by an appropriate motion of the mirror without the need for additional control laser or atomic level.

5.1 The quantum memory model

5.1.1 General optical Bloch equations

We study a single two-level atom placed in front of a moving mirror, as seen in Fig.(5.1). The incident pulse propagates along the z -axis and first interacts with the atom. The positive frequency part of the continuum electric field operator in the standing wave basis reads [95, 104, 115]

$$\mathbf{E}^{(+)}(z, t) = i \sum_{\lambda=1}^2 \int_0^{\infty} d\omega \mathcal{A}(\omega) \boldsymbol{\epsilon}_{\omega, \lambda} \sin(kz) e^{-i\omega t} a_{\omega}(t), \quad (5.1)$$

where $k = \omega/c$, $\boldsymbol{\epsilon}_{\omega, \lambda}$ with $\lambda = \{1, 2\}$ denotes the unit polarization of mode ω and the coefficient $\mathcal{A}(\omega)$ accounts for the correct normalization of the electric field. We denote the initial distance between the atom and the mirror by L . The main goal of this chapter is to investigate the dynamics of a two-level atom and a pulse in front of a moving mirror. The dynamics is given by the

time-dependent decay rate, which reaches its minimal value 0 for an atom sitting at the node and maximal value $2\gamma_0$ for the atom at the antinode of the cavity, a well known result from quantum cavity electrodynamics. We describe the motion of the mirror by a time-dependent function $l(t)$, such that the atom-mirror distance is given by $L - l(t)$ for any time t .

The dipole interaction Hamiltonian in the interaction picture, after making the rotating wave approximation, is given by

$$H_I(t) = -i\hbar \sum_{\lambda=1}^2 \int d\omega [g_{\omega,\lambda} \sigma_+ a_\omega \sin [k(L - l(t))] e^{-i(\omega - \omega_a)t} - h.c.]. \quad (5.2)$$

In the following, we assume that the atomic dipole \mathbf{e}_d is oriented parallel to the polarization of the field $\boldsymbol{\epsilon}$ and thus yielding the maximized coupling

$$g_\omega \equiv g_{\omega,\lambda} = \frac{d \mathcal{A}(\omega)}{\hbar}. \quad (5.3)$$

The Heisenberg equations of motion of the field and atomic operators are

$$\dot{a}_\omega = g_\omega^* \sin [k(L - l(t))] e^{i(\omega - \omega_a)t} \sigma_-, \quad (5.4)$$

$$\dot{\sigma}_- = -\frac{\gamma'}{2} \sigma_- + \zeta_- + \sigma_z \int d\omega g_\omega a_\omega \sin [k(L - l(t))] e^{-i(\omega - \omega_a)t}, \quad (5.5)$$

$$\dot{\sigma}_z = -\gamma'(\sigma_z + 1) + \zeta_z - 2 \int d\omega \sin [k(L - l(t))] [g_\omega \sigma_+ a_\omega e^{-i(\omega - \omega_a)t} + h.c.], \quad (5.6)$$

in which the decay term γ' and the noise operators ζ are introduced to account for the interaction of the atom with the environment. The explicit form of the noise operator is discussed in

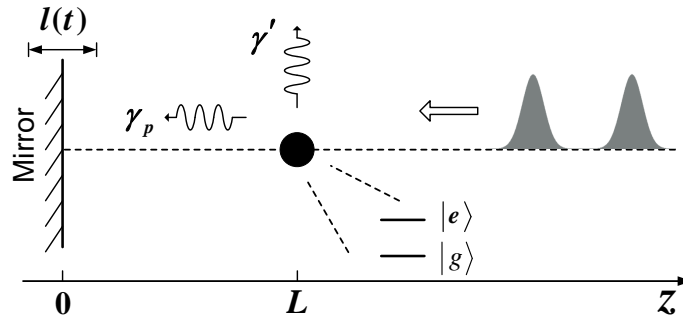


Figure 5.1: Sketch of the quantum memory setup: an arbitrary single photon wave packet interacts with a two-level atom which has a initial distance L from the movable mirror, whose motion is described by $l(t)$. γ_p and γ' describe the decay rates into the pulse mode and the environment, respectively (remark: in the implementation that we consider, the pulse durations are much longer than L/c).

Eqs.(3.13, 3.14) in Sec.(3.2). Moreover, as a consequence of our initial conditions, the noise operators do not come into play, as explained further in Sec.(3.2) as well. Again by integrating Eq.(5.4), we can separate the field operator into two parts:

$$a_\omega(t) = a_\omega(t_0) + \int_{t_0}^t dt' g_\omega^* \sin[k(L - l(t'))] e^{i(\omega - \omega_a)t'} \sigma_-(t'), \quad (5.7)$$

where again the first term refers to the initial field having evolved freely from t_0 to t and the second term is the field created by the atomic dipole during the time period $t - t_0$.

After substituting Eq.(5.7) into Eq.(5.5) and Eq.(5.6), we get the modified optical Bloch equations

$$\begin{aligned} \dot{\sigma}_-(t) = & -\frac{\gamma'}{2}\sigma_-(t) + \zeta_- \\ & + \sigma_z(t) \int d\omega g_\omega \sin[k(L - l(t))] e^{-i(\omega - \omega_a)t} a_\omega(t_0) \\ & + \sigma_z(t) \int_{t_0}^t dt' \int d\omega |g_\omega|^2 \sigma_-(t') \sin[k(L - l(t))] \sin[k(L - l(t'))] e^{-i(\omega - \omega_a)(t-t')}, \end{aligned} \quad (5.8)$$

$$\begin{aligned} \dot{\sigma}_z(t) = & -\gamma'(\sigma_z(t) + 1) + \zeta_z \\ & - 2 \int d\omega \sin[k(L - l(t))] (g_\omega \sigma_+(t) a_\omega(t_0) e^{-i(\omega - \omega_a)t} + h.c.) \\ & - 2 \int_{t_0}^t dt' \int d\omega |g_\omega|^2 \sin[k(L - l(t))] \sin[k(L - l(t'))] (e^{-i(\omega - \omega_a)(t-t')} \sigma_+(t) \sigma_-(t') + h.c.). \end{aligned} \quad (5.9)$$

5.1.2 Characteristics of the quantum memory setup

We will now focus on the quantum memory application of the considered setup and qualitatively discuss some characteristics the system should meet. One can thus make further assumptions which in turn enable to simplify the above equations.

Let's denote a round-trip time of the light between the atom and the mirror as $\tau = 2L/c$. In the ideal case we wish to absorb a photon by the atom, where the maximum coupling reaches $2\gamma_0$, as discussed earlier in this section, and indicates a relevant timescale (lower limit) for the photon duration.

(i) Markov approximation: $\gamma_0\tau \ll 1$ — to prevent losses due to spontaneous emission during

the write process.

- (ii) $l(t) \approx \lambda$ — the coupling can be tuned between its maximal and minimal value by changing the atom-mirror distance on the order of the wavelength λ , thus changing the position of the atom between nodes and antinodes at will.

Typically, $c\tau$ can be of the order of many wavelengths, so $\tau \gg l(t)/c$. With these arguments, we neglect the change in the operators on time scales smaller or equal to τ , so that $\sigma(t \pm \tau) \approx \sigma(t \pm l(t)/c) \approx \sigma(t)$. On the other hand, one must keep such dependence in all phases present in the equations in order to preserve the interferences. Then the atomic operators evolve as

$$\begin{aligned} \dot{\sigma}_-(t) = & -\gamma(t) \sigma_-(t) + \zeta_- \\ & + \sigma_z(t) \int d\omega g_\omega \sin[k(L - l(t))] e^{-i(\omega - \omega_a)t} a_\omega(t_0), \end{aligned} \quad (5.10)$$

$$\begin{aligned} \dot{\sigma}_z(t) = & -\gamma^z(t) (\sigma_z(t) + 1) + \zeta_z \\ & - 2 \int d\omega \sin[k(L - l(t))] (g_\omega \sigma_+(t) a_\omega(t_0) e^{-i(\omega - \omega_a)t} + h.c.). \end{aligned} \quad (5.11)$$

The time-dependent decay rates $\gamma(t)$ and $\gamma^z(t)$ are functions of the motion of the mirror $l(t)$

$$\gamma(t) = \frac{\gamma'}{2} + \frac{\gamma_p}{2} \left(1 - e^{i\omega_a \left(\tau - \frac{2l(t)}{c} \right)} \right), \quad (5.12)$$

$$\gamma^z(t) = \gamma' + \gamma_p \left(1 - \cos \left[\omega_a \left(\tau - \frac{2l(t)}{c} \right) \right] \right) = 2\text{Re}[\gamma(t)]. \quad (5.13)$$

Using again the first Markov approximation [98, p.341], the explicit formula for the decay into the pulse mode γ_p is given by $\gamma_p = \pi |g_{\omega_a}|^2$. We would like to note that in the derivation of the equations of motion Eqs.(5.10-5.11), various contributions to the level shifts are omitted (Lamb shift, Van der Waals and Casimir-Polder shifts). The reason is that for a typical atom-mirror distance $L \gg \lambda$, these level shifts are either negligible or constant [116]. The only relevant dynamical level shift, which is the imaginary part of $\gamma(t)$ Eq.(5.13) is included.

By inserting the Eq.(5.7) into the field operator Eq.(5.1), and again under the assumptions $\gamma_0\tau \ll 1$ and $l(t) \approx \lambda$, we have the simplified scattered field operator

$$E_{out}^{(+)}(z, t) = E_1^{(+)}(z, t) + E_2^{(+)}(z, t) \quad (5.14)$$

where

$$E_1^{(+)}(z, t) = i \int_0^\infty d\omega \mathcal{A}(\omega) \sin[k(z - l(t))] e^{-i\omega t} a_\omega(t_0), \quad (5.15)$$

is the free evolution electric field, and

$$\begin{aligned} E_2^{(+)}(z, t) = & -i \frac{\pi}{2} \mathcal{A}(\omega_a) g_{\omega_a} \\ & \times \left(e^{-i\omega_a \left(t - \left(\frac{\tau}{2} + \frac{z-2l(t)}{c} \right) \right)} \sigma_- \left(t - \frac{z}{c} \right) \Theta \left(t - \frac{z}{c} \right) \right. \\ & - e^{-i\omega_a \left(t - \left(\frac{z}{c} - \frac{\tau}{2} \right) \right)} \sigma_- \left(t - \frac{z}{c} \right) \Theta \left(t - \frac{z}{c} \right) \Theta \left(\frac{z-L}{c} \right) \\ & \left. - e^{-i\omega_a \left(t - \left(\frac{\tau}{2} - \frac{z}{c} \right) \right)} \sigma_- \left(t + \frac{z}{c} \right) \Theta \left(t + \frac{z}{c} \right) \Theta \left(\frac{L-z}{c} \right) \right). \end{aligned} \quad (5.16)$$

is the electric field scattered by the atom.

In Eq.(5.16), the usage of the *first Markov approximation* allows us to put $\mathcal{A}(\omega) \approx \mathcal{A}(\omega_a)$ out of the integration. Since we are only interested in the right propagating field in the region $z > L$ (see Fig.(5.1)), the step function $\Theta \left(\frac{L-z}{c} \right)$ implies that the third term in Eq.(5.16) does not contribute to the total field.

With the general equations for the atomic operators Eqs.(5.10-5.11) and the electric field operators Eqs.(5.14-5.16), it is now possible to study the dynamics of absorption, storage and retrieval of a single-photon wave packet. Since the absorption medium is a two-level system, we will consider in the following the storage process only of a single photon in Fock state [56, 96, p. 243] as defined from Eq.(2.46)

$$|1_p\rangle = \int d\omega f_p(\omega) a_\omega^\dagger |0\rangle = \int dt \xi_p(t) a_t^\dagger |0\rangle, \quad (5.17)$$

where $f_p(\omega)$, $p = \{in, out\}$ is the spectral distribution function and $\xi_p(t)$ is the temporal shape of the input and output wave-packets. Moreover, all the other considered quantities are labeled by w and r for the write and read process, respectively.

5.1.3 Write process: Absorption

During the write process, we wish to efficiently absorb the incoming photon and thus maximize the probability $P(t)$ that the atom gets excited, where ideally $P = 1$. Considering an incoming

photon which is nonzero only between times t_w and t_w^0 , which are the start and end time of the write process, the write efficiency is defined as

$$\eta_w = \frac{P(t_w^0)}{\int_{t_w}^{t_w^0} dt |\xi_{in}(t)|^2}. \quad (5.18)$$

In the case of single photon pulse, which satisfies the normalization condition $\int_{t_w}^{t_w^0} dt |\xi_{in}(t)|^2 = 1$, the write efficiency is then simply $\eta_w = P(t_w^0)$.

So far we have included the environmental decay channel described by the decay rate γ' and the related noise operators ζ . One important point is that when considering the initial state of the environment to be the vacuum state, the noise operators do not come into play, since $\langle \psi(t_w) | \zeta | \psi(t_w) \rangle = 0$. Although it is very challenging to achieve experimentally, in the following we assume that all modes of the field radiated by the atom to the mirror half-space (i.e. to the left of the atom in Fig.(5.1)) are covered by the mirror. This implies $\gamma' = 0$, $\gamma_p = \gamma_0$. It also enables us to separate the effect of the time-dependent coupling $\gamma(t)$ from the effect of the decay to the environment. It is then clear from Eq.(5.13) that the time-dependent decay rate $\gamma^z(t)$ changes between $[0, 2\gamma_0]$ depending on the position of the mirror.

The atomic excitation probability by single photon can be calculated from the formalism in Sec.(3.2.2) with the initial state of the total system $|\psi(t_w)\rangle = |g, 1_{in}, 0_e\rangle$. The solution of those equations gives us the absorption probability as

$$P(t_w^0) = \left| e^{-\Gamma_w(t_w^0)} \int_{t_w}^{t_w^0} dt e^{\Gamma_w(t)} g_w(t) \xi_{in}(t) \right|^2, \quad (5.19)$$

where we define

$$\Gamma_w(t) = \int_{t_w}^t dt' \gamma_w(t'), \quad (5.20)$$

with $\gamma_w(t)$ given by Eq.(5.12) and the subscript w indicates the write process in order to distinguish it from the read process which has in principle different decay function $\gamma_r(t)$. The effective time-dependent coupling strength reads

$$g_w(t) = \sqrt{2\gamma_0} \sin \left[\omega_a \left(\frac{\tau}{2} - \frac{l(t)}{c} \right) \right] = \sqrt{\gamma_w^z(t)}. \quad (5.21)$$

The goal is now to find the time-dependent $\gamma_w^z(t)$ that maximizes the write efficiency for a given input field $\xi_{in}(t)$, which can be done using Lagrange multiplier optimization [117, p. 169],

$$\frac{\delta}{\delta \xi_{in}^*(t)} \left[P(t_w^0) + \lambda \left(\int_{t_w}^{t_w^0} dt |\xi_{in}(t)|^2 - 1 \right) \right] = 0, \quad (5.22)$$

with the constraints of $\int_{t_w}^{t_w^0} dt |\xi_{in}(t)|^2 = 1$. Here λ is the Lagrange multiplier. We therefore find out that the optimum write process satisfies

$$\xi_{in}(t) = -\frac{1}{1 - e^{-\Gamma_w^z(t_w^0)}} e^{-\frac{\Gamma_w^*(t_w^0)}{2}} e^{\frac{\Gamma_w^*(t)}{2}} g^w(t). \quad (5.23)$$

Substitute Eq.(5.23) back into Eq.(5.19), we thus have the optimized write efficiency

$$\bar{\eta}_w = P(t_w^0) = 1 - e^{-\Gamma_w^z(t_w^0)}, \quad (5.24)$$

with $\Gamma_w^z(t) = \int_{t_w}^t dt' \bar{\gamma}_w^z(t')$, and the required time-dependent decay rate can be expressed as

$$\bar{\gamma}_w^z(t) = \begin{cases} \frac{\bar{\eta}_w |\xi_{in}(t)|^2}{(1-\bar{\eta}_w) + \bar{\eta}_w \int_{t_w}^{t_w^0} dt' |\xi_{in}(t')|^2} & : \bar{\gamma}_w^z(t) \leq 2\gamma_0; \\ 2\gamma_0 & : \bar{\gamma}_w^z(t) \geq 2\gamma_0, \end{cases} \quad (5.25)$$

where we have to account for the physical limitation of the system, $0 \leq \bar{\gamma}_w^z(t) \leq 2\gamma_0$.

After the absorption, the single photon is stored as the excitation of the atom for a time period T . During this period, the static mirror position is such that the atom sits at the node, i.e. $\gamma^z(t) = 0$, so that the atom remains in its excited state, which implies that $P(t_w^0 \leq t \leq t_r^0) = P(t_w^0)$ during the storage period.

5.1.4 Read process: Re-emission

For an on-demand readout of the stored single photon pulse, the atom-light interaction is turned on again at the starting time of the readout process $t_r^0 = t_w + T$. As discussed above, we consider no losses during the storage process, so that $P(t_r^0) = P(t_w^0) = \bar{\eta}_w$. In analogy to the write efficiency,

we define the efficiency of the readout process ending at time t_r as

$$\eta_r = \frac{\int_{t_r^0}^{t_r} dt |\xi_{out}(t)|^2}{P(t_r^0)}, \quad (5.26)$$

where $\xi_{out}(t)$ is the temporal shape of the outgoing pulse.

To find out the temporal shape of the output pulse after the readout process, we first study the c-number electric field of the input pulse

$$\langle 0 | E_1^{(+)}(z, t) | 1_{in} \rangle = -\sqrt{\frac{\pi}{2}} \mathcal{A}(\omega_0) [\xi(t - z/c) - \xi(t + z/c)], \quad (5.27)$$

where ω_0 is the carrier frequency of the input pulse, and again $\mathcal{A}(\omega) \approx \mathcal{A}(\omega_0)$ in Weisskopf-Wigner approximation. When the atom and pulse are in resonance with each other $\mathcal{A}(\omega_0) = \mathcal{A}(\omega_a)$, the total field is given by the interference of the right propagating pulse $\xi(t - z/c)$ and the left propagating pulse $\xi(t + z/c)$.

Similarly, the electric field contributing to the output pulse at the position of interest (i.e. outside the atom-mirror system, $z > L$), is only the right propagating part. In this case, the temporal shape of the output pulse is given by

$$\begin{aligned} \xi_{out}(z, t) &= \sqrt{\frac{2}{\pi}} \frac{1}{\mathcal{A}(\omega_a)} \langle \psi_0 | E_{out}^+(z, t) | \psi(t_r^0) \rangle \\ &= i \sqrt{\frac{2}{\gamma_0}} e^{-i\omega_a(t-z/c+\tau/2)} \gamma_r(t) \langle \psi_0 | \sigma_-(t - z/c) | \psi(t_r^0) \rangle, \end{aligned} \quad (5.28)$$

with $|\psi_0\rangle = |g, 0_{in}, 0_e\rangle$ and $|\psi(t_r^0)\rangle = |e, 0_{in}, 0_e\rangle$.

The evolution of the atomic operators can be also found using Eqs.(5.10-5.11)

$$\langle \psi_0 | \sigma_-(t - z/c) | \psi(t_r^0) \rangle = \sqrt{P(t_r^0)} e^{-\Gamma_r(t)}, \quad (5.29)$$

with $\Gamma_r(t) = \int_{t_r^0}^t dt' \gamma_r(t')$.

Since we are interested in the output pulse at certain position $z \geq L$, the temporal shape of the output pulse $\xi_{out}(t)$ reads

$$\xi_{out}(t) = \xi_{out}(z, t)|_{z=D \geq L} = i \sqrt{\frac{2 P(t_r^0)}{\gamma_0}} e^{-i\omega_a(t-D/c+\tau/2)} \gamma_r(t) e^{-\Gamma_r(t)}, \quad (5.30)$$

and the output pulse intensity profile reads

$$|\xi_{out}(t)|^2 = \bar{\eta}_w \gamma_r^z(t) e^{-\Gamma_r^z(t)}, \quad (5.31)$$

with $\Gamma_r^z(t) = \int_{t_r^0}^t dt' \gamma_r^z(t')$.

The integration of Eq.(5.31) gives

$$e^{-\Gamma_r^z(t)} = 1 - \frac{1}{\bar{\eta}_w} \int_{t_r^0}^t dt' |\xi_{out}(t')|^2, \quad (5.32)$$

and thus we have

$$-\Gamma_r^z(t) = \ln \left[1 - \frac{1}{\bar{\eta}_w} \int_{t_r^0}^t dt' |\xi_{out}(t')|^2 \right]. \quad (5.33)$$

The time-dependent read decay rate $\gamma_r^z(t)$ can be achieved by doing the time derivative on the above equation, which gives

$$\gamma_r^z(t) = \frac{|\xi_{out}(t)|^2}{\bar{\eta}_w - \int_{t_r^0}^t dt' |\xi_{out}(t')|^2}, \quad (5.34)$$

subjected to the constraint that $0 \leq \gamma_r^z(t) \leq 2\gamma_0$. This implies that the temporal shape of the output pulse can be adjusted by controlling the time-dependent read decay rate.

Plugging Eq.(5.30) into Eq.(5.26) one finds the expression for the read efficiency

$$\bar{\eta}_r = 1 - e^{-\Gamma_r^z(t_r)}. \quad (5.35)$$

The total quantum memory efficiency is given by

$$\bar{\eta} = \bar{\eta}_w \bar{\eta}_r = \left(1 - e^{-\Gamma_w^z(t_w^0)}\right) \left(1 - e^{-\Gamma_r^z(t_r)}\right). \quad (5.36)$$

So far we have derived an expression for the efficiency of the readout process as a function of a time-dependent readout decay rate $\gamma_r^z(t)$. We should however emphasize a simple reflection that, an atom in the excited state with a nonzero coupling to the field will necessarily decay. Typically, for a constant Γ_r , the decay will be exponential with η_r approaching 1 already for times of order $1/\Gamma_r$. The readout can be thus made simply by “waiting”.

In the following, we would rather require that the quantum memory device yields the maximum

fidelity $F = 1$. The memory fidelity is expressed in terms of the outgoing pulse's projection on the input pulse as

$$F = |\langle 1_{in} | 1_{out} \rangle|^2 = \frac{|\int dt \xi_{in}^*(t) \xi_{out}(t)|^2}{\int dt |\xi_{in}(t)|^2 \cdot \int dt |\xi_{out}(t)|^2}. \quad (5.37)$$

Obviously, the ideal fidelity is achieved when the output pulse has the same shape as the input pulse $\xi_{out}(t) = \sqrt{\bar{\eta}} \xi_{in}(t - T)$, which can be achieved by changing the read decay rate in the following way,

$$\bar{\gamma}_r^z(t) = \begin{cases} \frac{\bar{\eta}_r |\xi_{in}(t+(t_r^0-t_w^0))|^2}{1-\bar{\eta}_r \int_{t_r^0}^t dt' |\xi_{in}(t'+(t_r^0-t_w^0))|^2} & : \bar{\gamma}_r^z(t) \leq 2\gamma_0; \\ 2\gamma_0 & : \bar{\gamma}_r^z(t) \geq 2\gamma_0. \end{cases} \quad (5.38)$$

5.2 Simulation with time-bin qubit

With the help of Eqs.(5.25,5.38), we can now study the performance of the quantum memory as a function of the input light field. In the following, we consider a specific case of a normalized Gaussian-shaped time-bin single photon pulse described as

$$\xi_{in}(t) = \alpha e^{-\frac{(t-t_1)^2 \sigma^2}{2}} + \beta e^{i\phi} e^{-\frac{(t-t_2)^2 \sigma^2}{2}}, \quad (5.39)$$

where the real coefficients α, β satisfy $\alpha^2 + \beta^2 = 1$, $t_2 - t_1$ is the relative time delay, ϕ is the relative phase between the two time bins and the bandwidth σ is assumed the same for each time bin. The performance of the quantum memory is studied for different bandwidths σ of the pulse with $\alpha = \beta$. It is worth mentioning that for our quantum memory setup, we need to know the phase of the input pulse in order to rephase the output pulse using the moving mirror.

In Fig.(5.2), two particular situations are considered, one with photon bandwidth smaller and the other one with photon bandwidth larger than the double of the atomic decay rate $2\gamma_0$. In Fig.(5.2(a)), we set $\sigma = 0.2\gamma_0$. In this case, the quantum memory efficiency reaches its maximal value, $\bar{\eta} = 1$: the amplitude of the output pulse (solid black line) is the same as the input pulse (dashed black line) as can be seen from Fig.(5.2(a)) (i). On the other hand, Fig.(5.2(b)) with $\sigma = 5\gamma_0$ shows a decrease of the efficiency. The optimized decay rates $\bar{\gamma}_w^z(t)$ and $\bar{\gamma}_r^z(t)$ are represented by dashed and solid red lines respectively. The shapes of the optimum coupling decay rates are given by Eqs.(5.25,5.38) and might be qualitatively understood as follows. For write efficiencies $\bar{\eta}_w \approx 1$, the write decay rate $\bar{\gamma}_w^z(t)$ is proportional to the intensity divided by

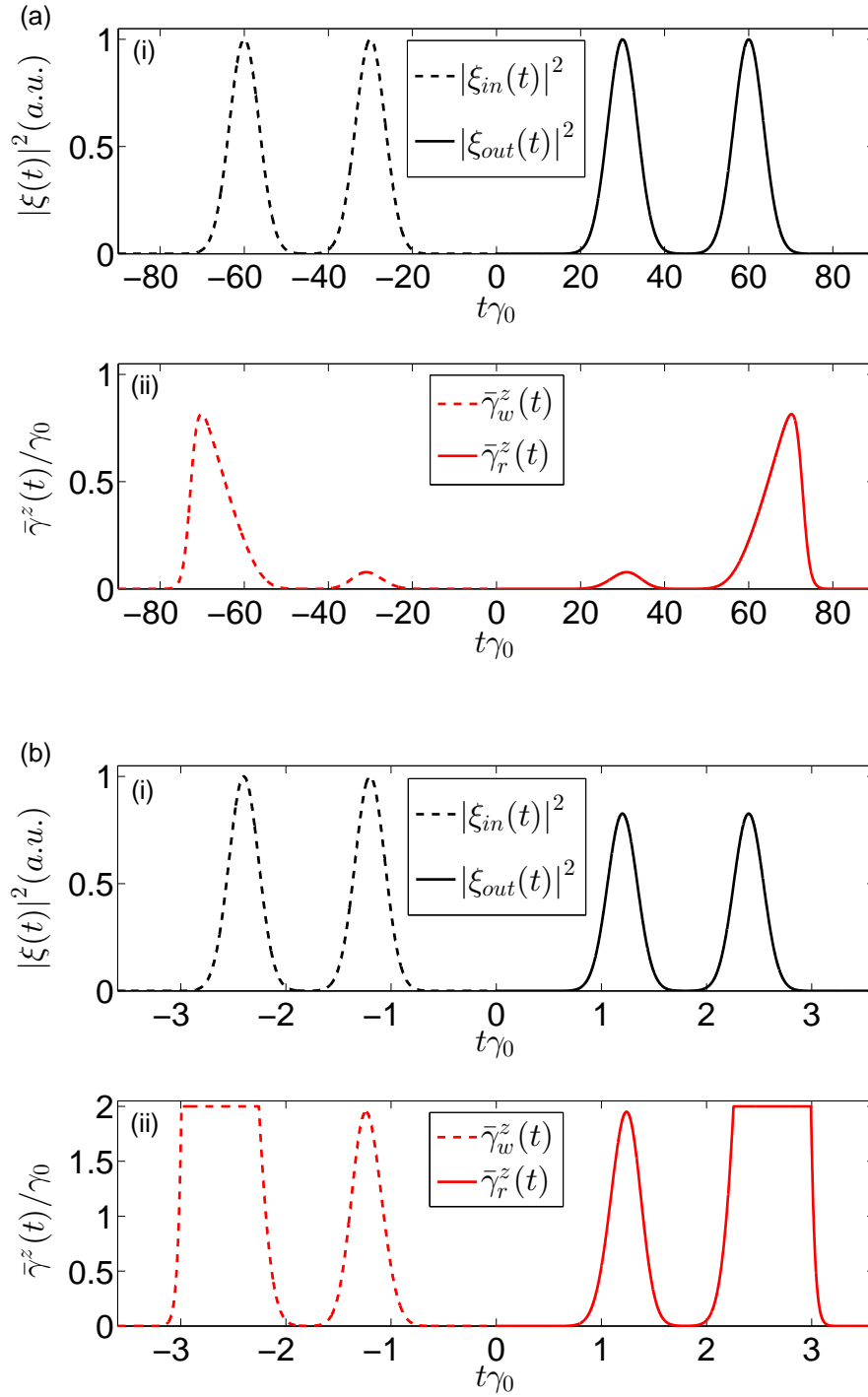


Figure 5.2: Storage ($t < 0$) and retrieval ($t > 0$) of a Gaussian-shaped time-bin single photon pulse for different values of bandwidth: (a) $\sigma = 0.2\gamma_0$; (b) $\sigma = 5\gamma_0$. The input intensity (dashed black line) and the output intensity (solid black line) of the pulse is shown in (i), with the input intensity normalized to amplitude 1. The required optimum write and read decay rate $\bar{\gamma}_w^z(t)$ and $\bar{\gamma}_r^z(t)$ is shown by dashed and solid red line in (ii), respectively. It can be seen that for the smaller bandwidth, case (a), $\text{Max} [\bar{\gamma}_{w,r}^z(t)] < 2\gamma_0$ and the efficiency is close to 1; on the other hand, for the larger bandwidth, case (b), where $\bar{\gamma}^z$ has to be truncated at $2\gamma_0$, the efficiency is less than 1.

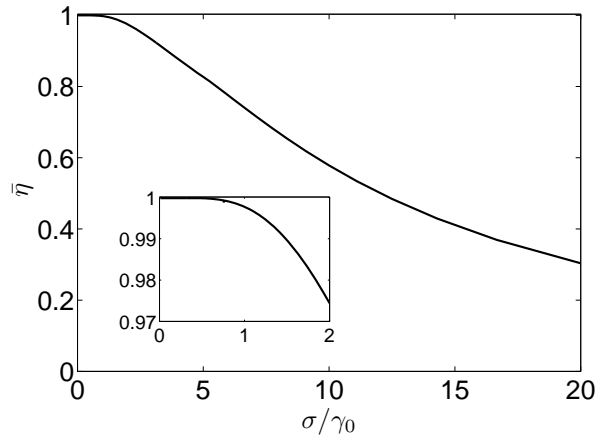


Figure 5.3: Total efficiency of the quantum memory device as a function of the bandwidth σ of the input pulse. The curve was obtained with Gaussian-shaped time-bin single photon wave packet Eq.(5.39) for ideal fidelity $F = 1$. The inset is a zoom of the region of σ/γ_0 between 0 and 2.

the time integral of the intensity. This ratio can be high at the beginning of the write process (first time bin), when the denominator is small, but gets significantly smaller for the second time bin. Similar argument holds for the read coupling decay. It is possible to plot the motion of the mirror $l(t)$ instead of the coupling decay rate $\bar{\gamma}^z(t)$ (see Eq.(5.13)). In the example presented in Fig.(5.2), the motion of the mirror is similar to the coupling decay rate with the $l(t)$ ranging from 0 to $\lambda/4$ (corresponding to $2\gamma_0$ for the decay rate) and we do not plot it explicitly. Finally, one can see that for the photon bandwidth larger than the cutoff frequency of the system $2\gamma_0$, the optimum decay rates $\bar{\gamma}_{w,r}^z(t)$ exceed this cutoff and are thus truncated at $2\gamma_0$. This results in the decrease of the storage efficiency, as shown in Fig.(5.2(b))(i). The storage efficiency as a function of the ratio between the photon bandwidth and the atomic decay rate is shown in Fig.(5.3). The efficiency starts to decrease for $\sigma/\gamma_0 \approx 0.85$ which corresponds to $FWHM = 2\sqrt{2\log 2}\sigma = 2\gamma_0$, as expected.

5.3 Implementations

We will now discuss possible implementations of our protocol. The described quantum memory device requires a single two-level system with a tunable distance to the mirror and a strong coupling to the light field. Strongly coupled two-level systems can be implemented using optical setups with ions and atoms [60, 118], quantum dots [119], superconducting qubits in circuit QED configuration [40, 66] or atoms coupled to surface plasmons on conducting nanowires [120] or to

tapered optical nanofibers [121].

As for the quantum optical implementations, there is a variety of atoms and ions used in trapping experiments, typical examples being e.g. a $^{138}\text{Ba}^+$ ion in a Paul trap [61, 118, 122] or ^{87}Rb atom in a FORT trap [60]. In the case of $^{138}\text{Ba}^+$ ions, the typical two-level transition is between the ground state $|6S_{1/2}, m_F = 1/2\rangle$ and excited state $|6P_{1/2}, m_F = -1/2\rangle$ at $\lambda = 493$ nm with a linewidth $\gamma_0 = 15$ MHz [61]. For this system, as experimental realization with half-cavity an tunable atom-mirror has been reported [123] (an analogous experimental setup with quantum dot has been also realized [119]). This, together with an atom-mirror distance L of order of centimeters, meets very well the assumption required for quantum memory: $\gamma_0\tau \ll 1$. On the other hand, the durations of incoming photon of the order up to $1/\gamma_0$ require the motion of the mirror at the same time scale, which might be hard to achieve by a mechanical motion. One possible solution is to use a long-lived quadrupole transition (for which the lifetime can be seconds (e.g. Ca^+ or Ba^+)) which would allow for slower mechanical motion of the mirror achievable with current technology. Another possibility is to move the atom itself, which can be done very fast in Dipole or Paul traps. The drawback of this approach is that the atom would get slightly out of the focus of the mirror, reducing thus the maximum achievable coupling decay rate [116]. It might be also be possible to use an EOM in the integrated setup to modulate the optical path-length [120, 121].

The spatial overlap of the incident field and the atomic dipole pattern needs to be taken into account in realistic systems, as discussed elsewhere in more detail for hemispherical mirror [116] and for parabolic mirror [55, 124]. The consequence of imperfect spatial overlap is the decay into the environment γ' which would reduce the write efficiency as well as, and more importantly, the storage process (since the storage time T is often required to be much larger than the photon duration, the population of the excited state $\propto \exp(-\gamma'T)$ is more affected during the storage, because $\exp(-\gamma'T) \ll \exp(-\gamma't_p)$, where t_p is the pulse duration). Obviously, the quantum memory scheme works only for single photon Fock states, which are available experimentally [125]. Finally, we would like to mention that the quantum memory works also for the polarization qubits. In this case the required level scheme is a V configuration, standardly available for typical atoms used in the experiments.

The proposed quantum memory device can be also implemented in the fast growing domain

of circuit QED, where the effective two-level system can be realized by different kinds of superconducting qubits [40, 66]. Typical resonant frequencies of a superconducting qubit lay in the microwave region of order of 1-10 GHz with population decay rates of order of 1-10 MHz [64, 126, 127]. Generation of various photonic states, including a single photon Fock state, was demonstrated in several experiments [126, 128, 129] laying thus the ground for potential realization of the presented quantum memory scheme. The configuration of superconducting qubits coupled to a transmission line resonator has the beauty of well defined one-dimensional (1D) mode and perfect spatial overlap, which results in strong atom-light interaction. Moreover, an open transmission line with one side terminated by a SQUID operated with a variable magnetic flux, acts as a mirror with a tunable qubit-mirror distance. This was realized recently in the remarkable demonstration of dynamical Casimir effect by Wilson *et al.* [86], with oscillation frequency of the SQUID mirror of 11 GHz. Currently, schemes and proposals directly linked to quantum memory applications are actively investigated both theoretically [130] and experimentally [82, 131–133]. In one of the realized experiments, a superconducting qubit with a large decoherence rate (order of MHz) was coupled to a transition with a long coherence time (up to 2 ms) in a NV center in a diamond [134]. This technique can be applied also to our proposal to achieve long storage time for the microwave photons.

Part II

Ultrafast gate in circuit QED

Quantum Electrical Circuits

Electrical circuits can be described by the degrees of freedom related to its charge distribution. Conventionally, the dynamical variables related to these degrees of freedom are treated using classical electrodynamics. However, at very low (cryogenic) temperatures, micro- and nanoscale superconducting circuits can have low enough dissipation that the discreteness of their energy levels emerges. Furthermore, a fully quantum mechanical description of the circuit is required when decoherence induced by uncontrolled degrees of freedom is sufficiently reduced [135]. The experimental progress over the last few decades in creating and controlling quantum coherence in superconducting electrical circuits has been truly remarkable.

In this chapter, we introduce the general procedure for the quantization of electrical circuits, which has been thoroughly addressed by B. Yurke and J.S. Denker [136] and M.H. Devoret [137]. The basic idea is similar to the classical description of electrical circuits — is to decompose the circuit into lumped elements and identify the node points that correspond to the degrees of freedom of the circuit. The lumped-element approximation is valid for frequencies corresponding to wavelengths much larger than the size of the elements. Each node point is associated with a generalized coordinate that can be used, together with the corresponding generalized momentum, to express the potential and kinetic energy of that node and thus the Lagrangian of the circuit. Given the Lagrangian, the procedure of canonical quantization can be applied, which results in a quantum mechanical Hamiltonian that describes the circuit.

6.1 Fundamental circuit elements

The most commonly occurring circuit elements — capacitance and inductance, are described using the magnetic flux Φ and charge Q as coordinates, and their contribution to the circuit Lagrangian is also given in the following.

6.1.1 Capacitance

A *capacitance* C describes the energy contained in charges accumulated on an insulating device, in terms of the voltage across the device, e.g., the charge accumulated on two parallel conducting plates with a potential difference. The circuit symbol for a capacitor is shown in Fig.(6.1).

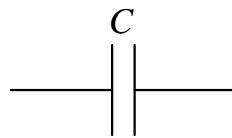


Figure 6.1: Circuit symbol for a capacitor.

The voltage $V(t)$ across the capacitance is proportional to the charge $Q(t)$ stored,

$$V(t) = \frac{Q(t)}{C}. \quad (6.1)$$

The electric current $I(t)$ is represented as the rate at which charge $Q(t)$ flows through a given surface as,

$$I(t) = \frac{dQ(t)}{dt}. \quad (6.2)$$

The charging energy E_C of the capacitor can be expressed in terms of charge

$$E_C = \frac{CV^2}{2} = \frac{Q^2}{2C}. \quad (6.3)$$

6.1.2 Inductance

An *inductor*, shown in Fig.(6.2), is an element which builds up a voltage when you change the current through it according to,

$$V(t) = L \frac{dI(t)}{dt}, \quad (6.4)$$

where inductance L describes its ability to store energy in its magnetic field.



Figure 6.2: Circuit symbol for an inductor.

Equivalently, one can also talk about the magnetic flux,

$$\Phi(t) = \int_0^t dt' V(t'), \quad (6.5)$$

and that the inductance stores a flux $\Phi(t)$ proportional to the current $I(t)$ through the inductance,

$$I(t) = \frac{\Phi(t)}{L}. \quad (6.6)$$

The energy of the inductance stored in the magnetic field is,

$$E_L = \frac{LI^2}{2} = \frac{\Phi^2}{2L}. \quad (6.7)$$

Consequently, the contribution of an inductive element to the circuit Lagrangian is a potential term on the form $\Phi^2/(2L)$.

6.2 Flux quantization and Josephson effect

According to the theory of Bardeen, Cooper and Schrieffer (BCS theory) [138], superconductor all of the Cooper pairs of electrons (which have charge $2e$, mass $2m_e$ and spin zero, and are responsible for carrying a supercurrent) are condensed into a single macroscopic state described by a wavefunction $\Psi(\mathbf{r}, t)$,

$$\Psi(\mathbf{r}, t) = |\Psi(\mathbf{r}, t)| e^{i\varphi(\mathbf{r}, t)}, \quad (6.8)$$

as a product of an amplitude and a factor involving the phase φ .

The macroscopic wave-function leads to two important phenomena, which are *flux quantization* and *Josephson effect*.

6.2.1 Flux quantization

A superconducting loop with loop-inductance L , threaded by an externally applied magnetic flux Φ_{ext} , has an induced flux $\Phi_{ind} = LI$ due to a circulating current I . The induced flux is such that the total magnetic flux through the loop is quantized, $\Phi_{ext} + \Phi_{ind} = n\Phi_0$ [139], where n is an integer and the magnetic flux quantum is

$$\Phi_0 = \frac{h}{2e} = 2.067833636 \times 10^{-15} \text{ Wb}. \quad (6.9)$$

Similarly, the reduced flux quantum can be defined as $\phi_0 = \Phi_0/2\pi = \hbar/2e$.

For superconducting loops that are interrupted by one or more Josephson junctions, the corresponding requirement results in fluxoid quantization [139],

$$\oint_C (\Lambda \mathbf{J}_s) \cdot d\mathbf{l} + \int_S \mathbf{B}_s \cdot d\mathbf{s} = n\Phi_0 \quad (6.10)$$

where \mathbf{J}_s is the current density, $\Lambda = m_*/(n_s q_*^2)$ is the London parameter [139], \mathbf{B}_s is the magnetic field, and the left-hand side is called fluxoid.¹ While the surface integral of the magnetic field in this case is also equal to the total magnetic flux through the loop, the line integral of the current now equals the sum of the phase differences across the Josephson junctions:

$$\frac{\Phi_0}{2\pi} \sum_i^n \varphi_i + \Phi_{ind} + \Phi_{ext} = n\Phi_0. \quad (6.11)$$

Since the Josephson inductance dominates over the self-inductance of the loop, Φ_{ind} can be ignored in the flux quantization, such that

$$\frac{\Phi_0}{2\pi} \sum_i^n \varphi_i + \Phi_{ext} = n\Phi_0. \quad (6.12)$$

6.2.2 Josephson effect

A *Josephson junction* (JJ) is a circuit element made up of a tunnel barrier between two superconductors, as shown in Fig.(6.3). The Josephson effect is due to the quantum mechanical nature of superconductors, whose state can be described by a global wavefunction in Eq.(6.8) with a definite, gauge-invariant

¹Here n_s is the super-fluid density, and q_* the charge and m_* the mass of the superconducting electrons, which appear in Londons equation for the supercurrent.

phase. Two superconductors separated by a weak link can have coupled, i.e., overlapping, wavefunctions that result in tunneling of Cooper pairs between the two superconductors [135].

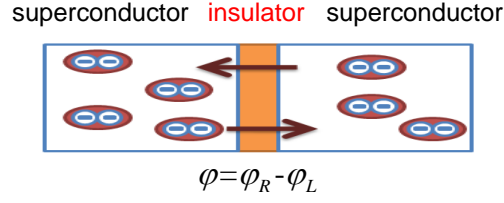


Figure 6.3: A schematic representation of a Josephson Junction, consisting of a thin insulating tunneling barrier that separates two superconducting electrodes.

DC Josephson relation

The rate of tunneling is related to the phase difference φ between the two wavefunctions, and the tunneling results in a dc current

$$I(t) = I_C \sin \varphi(t), \quad (6.13)$$

where critical current I_C is proportional to the Josephson energy E_J

$$I_C = \frac{2e}{\hbar} E_J = \frac{2\pi}{\Phi_0} E_J = \frac{1}{\phi_0} E_J. \quad (6.14)$$

AC Josephson relation

As predicted by B.D. Josephson in his seminal paper in 1962 [140], the phase difference across a voltage-biased junction evolves in time according to

$$\frac{d\varphi(t)}{dt} = \frac{2\pi}{\Phi_0} V(t), \quad (6.15)$$

or equally

$$\varphi(t) = \frac{2\pi}{\Phi_0} \int_0^t dt' V(t') + \varphi(0), \quad (6.16)$$

where $V(t)$ is the voltage across the junction.

The relation between the phase φ and the flux Φ is

$$\varphi = \frac{2e}{\hbar} \Phi = \frac{2\pi}{\Phi_0} \Phi = \frac{1}{\phi_0} \Phi. \quad (6.17)$$

For a constant voltage V , the phase evolves as $\varphi(t) = 2\pi Vt/\Phi_0$, and the current through the junction, $I = I_C \sin(Vt/\phi_0)$ is oscillating with frequency V/Φ_0 .

The energy stored in an ideal Josephson junction can be calculated using the Josephson relations Eq.(6.13) and Eq.(6.15),

$$U_J = \int_0^t dt IV = \frac{\Phi_0}{2\pi} \int_0^t dt I \frac{d\varphi}{dt} = I_C \frac{\Phi_0}{2\pi} \int d\varphi \sin \varphi = E_J (1 - \cos \varphi(t)). \quad (6.18)$$

However, it is also convenient to consider a Josephson junction as an inductor, with an effective inductance L_J that follows

$$L_J = \frac{V(t)}{dI/dt} = \frac{V(t)}{I_C \cos \varphi(t) d\varphi/dt} = \frac{V(t)}{I_C \cos \varphi(t) d\varphi/dt V(t) 2\pi/\Phi_0} = \left(\frac{\Phi_0}{2\pi} \right)^2 \frac{1}{E_J \cos \varphi(t)}. \quad (6.19)$$

Here, the effective inductance L_J has a nonlinear dependence on V and I , through the $\cos \varphi(t)$ factor in the denominator, and a Josephson junction therefore behaves as a *nonlinear* inductor. This nonlinearity of Josephson junctions is unusual among nondissipative circuit elements, and it has been exploited in many applications.

The tunnel barriers required for the Josephson effect to occur can be implemented in physical systems by thin nonconducting oxide layers, typically a few nanometers thick, separating the two superconductors. Such physical Josephson junctions, however, are not identical to the ideal Josephson junctions considered above. In addition to their Josephson junction characteristics, they can also have capacitive and resistive properties. However, here we will only consider Josephson junctions with negligible resistivity, leaving us with a model of a Josephson junction that consist of a capacitance and a nonlinear inductance. The circuit symbol for a Josephson junction is shown in Fig.(6.4(a)), and an equivalent circuit model in Fig.(6.4(b)).

The circuit model of a physical Josephson junction contains both kinetic and potential degrees of freedom. Considering a constant current bias I , Kirchhoff's current law results in an equation of



Figure 6.4: The circuit symbol for a Josephson junction is a diagonal cross, with (a) or without (b) a surrounding box. The cross inside the box represent the whole junction, including the junction capacitance C_J , whereas the cross itself represent the nonlinearity of the ideal Josephson junction.

motion that illustrates this point

$$I = I_C \sin\left(\frac{\Phi}{\phi_0}\right) + C_J \ddot{\Phi}. \quad (6.20)$$

This corresponds to a Lagrangian with a kinetic term

$$K(\Phi) = \frac{C_J \dot{\Phi}^2}{2}, \quad (6.21)$$

and potential term

$$U(\Phi) = -I\Phi + E_J [1 - \cos \varphi(t)], \quad (6.22)$$

which looks like a tilted-washboard. The Lagrangian for the current-biased Josephson junction, corresponding to the lumped-element circuit model in Fig.(6.4(b)), is therefore

$$\mathcal{L} = \frac{C_J}{2} \dot{\Phi}^2 - E_J (1 - \cos \varphi(t)) + I\Phi. \quad (6.23)$$

Small Oscillations

For large effective mass, i.e., large capacitance C_J , the dynamics of the system is confined to one of the wells in the washboard potential, and it is sufficient to consider small oscillations within such a well. The local minimum occur at $dU/d\Phi = 0$, i.e., $I/I_C = \sin(2\pi\Phi/\Phi_0)$, or $\Phi_m = 2\pi/\Phi_0 \arcsin(I/I_C)$. Expanding the potential around this point results in

$$U = U_0 + \frac{1}{2} \left(\frac{2\pi}{\Phi_0}\right)^2 E_J \cos\left(2\pi \frac{\Phi_m}{\Phi_0}\right) (\Phi - \Phi_m)^2, \quad (6.24)$$

and the frequency of small oscillations (the plasma frequency) is given by

$$\omega_p = \frac{1}{C_J} \left. \frac{d^2 U(\Phi)}{d\Phi^2} \right|_{\Phi=\Phi_m} = 2\pi \sqrt{\frac{E_J}{\Phi_0^2 C_J} \cos\left(2\pi \frac{\Phi_m}{\Phi_0}\right)} = 2\pi \sqrt{\frac{E_J}{\Phi_0^2 C_J} (1 - (I/I_C)^2)^{1/4}}. \quad (6.25)$$

6.3 Quantization of electrical circuits

From a lumped-element description of an electrical circuit, it is straightforward to write down its corresponding circuit Lagrangian in terms of the dynamical variables that describe the degrees of freedom of each element in the circuit. The Lagrangian formulation can then be used to derive classical equations of motion for the circuit, and it can also be used as starting point for a fully quantum mechanical description of the circuit. The Hamiltonian \mathcal{H} corresponding to the Lagrangian \mathcal{L} , is obtained by a Legendre transformation

$$\mathcal{H} = \sum_i \frac{\partial \mathcal{L}}{\partial \dot{q}_i} \dot{q}_i - \mathcal{L} = \sum_i p_i \dot{q}_i - \mathcal{L}, \quad (6.26)$$

where the sum is over the generalized coordinates q_i that describes the circuit. From this point we can proceed to write down a quantum mechanical description using the so-called canonical quantization procedure. It states that the two conjugate variables used to write the Hamiltonian satisfies the canonical commutation relation

$$[q_i, p_i] = i\hbar, \quad (6.27)$$

where the q_i is the generalized coordinate operator, and the p_i is the corresponding conjugate momentum operator,

$$p_i = \frac{\partial \mathcal{L}}{\partial \dot{q}_i}. \quad (6.28)$$

This commutation relation is the key point in the quantization procedure, from which all quantum mechanical properties originates.

Moreover, the dynamics of the system is described by the Heisenberg's equation of motion as in Eq.(3.1), which is the quantum analogy of the classical *Euler-Lagrange equation* of motion,

$$\frac{d}{dt} \frac{\partial \mathcal{L}}{\partial \dot{q}_i} - \frac{\partial \mathcal{L}}{\partial q_i} = 0. \quad (6.29)$$

6.3.1 The capacitance-matrix method

Given a set of generalized coordinates $\{q_i\}$, the Lagrangian with kinetic terms on quadratic form (i.e., quadratic in \dot{q}_i) can be written in the matrix form

$$\mathcal{L} = \frac{1}{2} \dot{\mathbf{q}}^T \mathbf{C} \dot{\mathbf{q}} - \mathbf{A}^T \dot{\mathbf{q}} - U(\mathbf{q}), \quad (6.30)$$

where $\mathbf{q} = (q_1, q_2, \dots, q_n)^T$ is the state vector, \mathbf{C} is the capacitance matrix, \mathbf{A} is a displacement vector, and $U(\mathbf{q})$ is the potential. In this formalism (see, i.e., [141]) the generalized momentum vector is $\mathbf{p} = \mathbf{C} \dot{\mathbf{q}} - \mathbf{A}$, and the Hamiltonian given by the Legendre transform of Eq.(6.26) becomes

$$\mathcal{H} = \frac{1}{2} (\mathbf{q} + \mathbf{A})^T \mathbf{C}^{-1} (\mathbf{q} + \mathbf{A}) + U(\mathbf{q}), \quad (6.31)$$

The Hamiltonian \mathcal{H} corresponding to the circuit Lagrangian \mathcal{L} can therefore be found by a systematic procedure, which essentially reduces to inverting the capacitance matrix \mathbf{C} .

When using the phases (fluxes) as generalized coordinates, it is the capacitive circuit elements that provide the kinetic terms containing \dot{q}_i . Since the circuits we are interested in have linear capacitances, but possibly nonlinear inductances, it is most convenient to use the phases as generalized coordinates. This choice of coordinates ensures that the Lagrangian is quadratic in the kinetic terms, and the nonlinearities are contained in the potential.

Strong coupling in QED: The rotating wave approximation and beyond

In this chapter, we discuss the interaction between a single two-level dipole emitter and a single mode of the electromagnetic field in a cavity for different coupling regimes in two different physical systems — cavity QED and circuit QED. The performance of two-qubit quantum controlled phase gate is analysed beyond rotating wave approximation.

7.1 Cavity quantum electrodynamics

Quantum electrodynamics, commonly referred to as QED, is a quantum field theory that describes the interaction at the most fundamental level between matter (electrons, mesons, and other atomic and subatomic particles) and electromagnetic fields. Cavity quantum electrodynamics (cavity QED) studies the interaction between atoms and the quantized discrete electromagnetic modes inside a cavity, where the cavity refers to an optical or microwave resonator. Such systems are of great interest and importance in the study of fundamental quantum mechanics of open systems, the engineering of quantum states for the quantum information processing. The quantum electrodynamics of superconducting microwave circuits has been known as circuit QED by analogy to cavity QED in quantum optics, where the superconducting qubits play the role of artificial atoms and the microwave resonator plays the role of the cavity.

Despite being large enough to be visible to the naked eye, these Josephson junction based

artificial atoms have a very simple discrete set of quantized energy levels which are nearly as well understood as those of the prototypical single-electron atom, hydrogen. Furthermore it has proven possible to put these atoms into coherent superpositions of different quantum states so that they can act as quantum bits. In addition to being a potentially powerful engineering architecture for building a quantum computer, circuit QED opens up for us a novel new regime to study ultrastrong coupling between “atoms” and individual microwave photons.

7.1.1 The general atom-cavity model

The electric field linearly polarized in the x -direction for a cavity resonator of length L is expressed in the normal modes of the cavity as [94, p. 5]

$$\mathbf{E}(z) = \sum_j E_j(z, t) \mathbf{x} = \sum_j \sqrt{\frac{\hbar\omega_k}{\epsilon_0 V}} [a_j + a_j^\dagger] \sin k_j z \mathbf{x}. \quad (7.1)$$

The boundary conditions define the wave vectors to be $k_j = \pi j/L$, with $j = 1, 2, 3, \dots$, so that $E_j(0) = E_j(L) = 0$. The corresponding frequencies are given by the dispersion relation $\omega_j = k_j c$.

For a two-level atom sitting inside a cavity with states $\{|g\rangle, |e\rangle\}$, and energy splitting $\omega_a =$

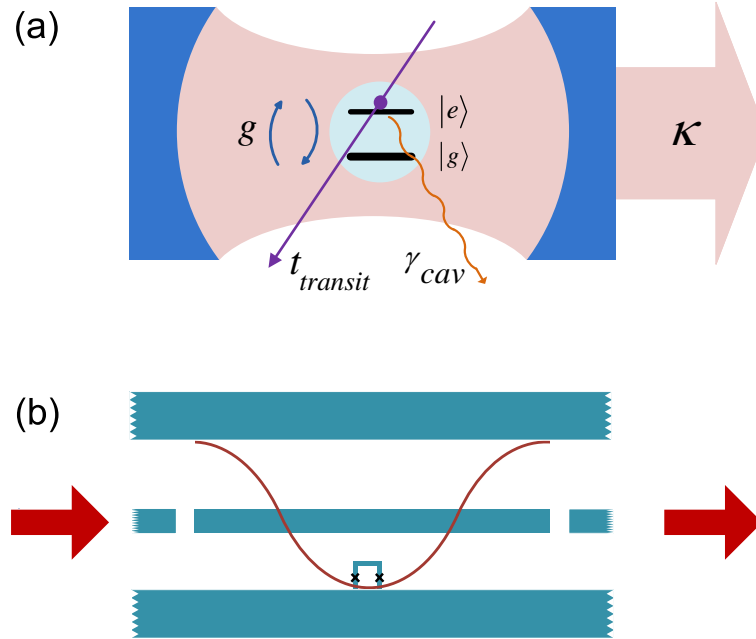


Figure 7.1: Standard representation of a cavity QED (a) and a circuit QED (b) system.

$\omega_e - \omega_g$ close to a particular resonance mode in the cavity $\omega_r \equiv \omega_j$, as schematically shown in Fig.(7.1(a)). The Hamiltonian in the dipole approximation describing the small atom-cavity system is given by the so called Rabi Hamiltonian

$$H_{Rabi} = H_0 + H_{int}, \quad (7.2)$$

$$H_0 = \hbar\omega_r a^\dagger a + \frac{1}{2}\hbar\omega_a \sigma_z, \quad (7.3)$$

$$H_{int} = \hbar g \sigma_x (a + a^\dagger). \quad (7.4)$$

with $g = dE(z_a)/\hbar$ being the coupling strength between the atom and the standing-wave field.

7.1.2 Rotating wave approximation and Jaynes-Cummings Model

In the rotating frame with respect to $U = e^{iH_0 t/\hbar}$, the interaction term in Eq.(7.4) becomes

$$H'_{int} = \hbar g \left(\sigma_+ a e^{i(\omega_a - \omega_r)t} + \sigma_- a^\dagger e^{-i(\omega_a - \omega_r)t} + \sigma_+ a^\dagger e^{i(\omega_a + \omega_r)t} + \sigma_- a e^{-i(\omega_a + \omega_r)t} \right). \quad (7.5)$$

When the atom and the cavity are close to resonance $|\Delta| \ll \min\{\omega_a, \omega_r\}$ with $\Delta = \omega_a - \omega_r$, the first two terms of Eq.(7.5) precess slowly, while the last two terms precess very fast. For a coupling strength that $g \ll \omega_r$, in a period of the interaction time π/g , the last two terms oscillate many times and as a consequence average to a very small value, so that they can be neglected. This is the so called *rotating-wave approximation* (RWA) and the Hamiltonian Eq.(7.4) becomes the well known *Jaynes-Cummings Hamiltonian*,

$$H_{JC} = \hbar\omega_r a^\dagger a + \frac{1}{2}\hbar\omega_a \sigma_z + \hbar g (\sigma_+ a + a^\dagger \sigma_-). \quad (7.6)$$

It can be directly seen from the interaction term that this Hamiltonian conserves the total number of excitations — when the qubit is excited (de-excited) the cavity becomes de-excited (excited). This means that the Jaynes-Cummings model can be reduced to a two-dimensional subspace and

Eq.(7.6) is box-diagonal in the basis $\{|e, n\rangle, |g, n+1\rangle\}$,

$$H_{JC} |e, n\rangle = \left(n\hbar\omega_r + \frac{1}{2}\hbar\omega_a \right) |e, n\rangle + \hbar g \sqrt{n+1} |g, n+1\rangle, \quad (7.7)$$

$$H_{JC} |g, n+1\rangle = \left(\hbar\omega_r(n+1) - \frac{1}{2}\hbar\omega_a \right) |g, n+1\rangle + \hbar g \sqrt{n+1} |e, n\rangle. \quad (7.8)$$

The corresponding matrix representation in the 2×2 subspace spanned by $\{|e, n\rangle, |g, n+1\rangle\}$ is

$$H = \left(n + \frac{1}{2} \right) \hbar\omega_r \begin{pmatrix} 1 & 0 \\ 0 & 1 \end{pmatrix} + \frac{\hbar}{2} \begin{pmatrix} \Delta & 2g\sqrt{n+1} \\ 2g\sqrt{n+1} & -\Delta \end{pmatrix}. \quad (7.9)$$

The eigenvalues and eigenstates turn out to be [63],

$$E_{n,\pm} = \left(n + \frac{1}{2} \right) \hbar\omega_r \pm \frac{\hbar}{2} \sqrt{\Delta^2 + 4g^2(n+1)}, \quad (7.10)$$

$$E_0 = -\frac{\hbar}{2}\Delta, \quad (7.11)$$

and

$$|+, n\rangle = \cos \theta |e, n\rangle + \sin \theta |g, n+1\rangle, \quad (7.12)$$

$$|-, n\rangle = -\sin \theta |e, n\rangle + \cos \theta |g, n+1\rangle, \quad (7.13)$$

with the atom-cavity mixing angle

$$\theta = \frac{1}{2} \arctan \left(\frac{2g\sqrt{n+1}}{\Delta} \right). \quad (7.14)$$

This angle indicates the degree of entanglement between the atom and the cavity states. It is clear that Jaynes-Cummings model describes the coherent exchange of a single excitation between the atom and the cavity mode. When the atom and the cavity are resonant $\Delta = 0$, the two states are split by an energy $2g\sqrt{n+1}$; when the system is very far detuned $\Delta \gg g\sqrt{n}$, the dressed states become the separable atom-cavity eigenstates $|e, n\rangle$ and $|g, n+1\rangle$. This means the detuning is a parameter that can be employed to switch the interaction on and off.

7.2 Circuit quantum electrodynamics

We now consider the realization of cavity QED using the superconducting circuits, where the superconducting qubits considered as artificial atoms interact with the microwave resonators playing the role of cavities, as shown in Fig.(7.1(b)).

7.2.1 Superconducting qubits as artificial atoms

All superconducting qubits are built with one or several Josephson junctions, which acts as nonlinear inductors in a circuit and thus provide an anharmonicity between the energy levels. Two important energy scales determine the quantum mechanical behaviour of a Josephson-junction circuit: namely, the Josephson coupling energy E_J and the electrostatic Coulomb energy $E_c = (2e)^2/2C_J$, where C_J is the junction capacitance. The phase difference of a Josephson junction φ and the number N of Cooper pairs on the island are conjugate variables in analogy to the position and momentum, as expressed by the commutator bracket $[\varphi, N] = i$ in quantum mechanics. Different kinds of superconducting qubits can be implemented according to their relevant degree of freedom in different regimes of E_J/E_c [41]. The charge qubit works in the charge regime $E_c \gg E_J$, where the number of Cooper pair boxes on the island is well defined [67]. The flux [68], phase [70] and transmon [71] qubits operate in the flux regime $E_J \gg E_c$, where the phase φ across the junctions is well defined.

7.2.2 Circuit QED with flux qubit

Within the scope of this thesis, we consider only the flux qubit. In the following, we show the analogy to cavity QED with a three-junction designed flux qubit coupled to a lumped LC resonator. as an example.

The flux qubit, as shown in Fig.(7.2), is consisted of a superconducting loop interrupted with three Josephson junctions, where one of them is α times smaller than the other two. The energy potential of the flux qubit is given by [68, 142]

$$\mathcal{U}_q = - \sum_{j=1}^3 E_{Jj} (1 - \cos \varphi_j) = -E_J [2 + \alpha - \cos \varphi_1 - \cos \varphi_2 - \alpha \cos(2\pi f + \varphi_1 - \varphi_2)] \quad (7.15)$$

given the flux quantization being $\varphi_1 - \varphi_2 + \varphi_3 = 2\pi f$, $f = \Phi/\Phi_0$ being the magnetic frustration.

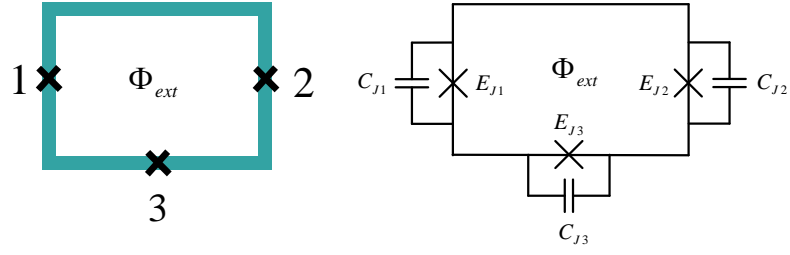


Figure 7.2: The flux qubits consist of a superconducting loop interrupted by three Josephson junctions.

The total Hamiltonian can be written as [142, 143]

$$\mathcal{H}_q = \frac{P_p^2}{2M_p^2} + \frac{P_m^2}{2M_m^2} + E_J \left[2 + \alpha - 2 \cos \varphi_m \cos \varphi_p - \alpha \cos(2\pi f + 2\varphi_m) \right], \quad (7.16)$$

with the phase $\varphi_m = (\varphi_1 - \varphi_2)/2$, $\varphi_p = (\varphi_1 + \varphi_2)/2$, the momenta $P_{p,m} = -i\hbar\partial/\partial\varphi_{p,m}$, and the mass $M_p = 2C_J(\Phi_0/2\pi)^2$, $M_m = (1 + 2\alpha)C_J(\Phi_0/2\pi)^2$.

The properties of the qubit can be obtained from diagonalize Eq.(7.16) numerically and it was observed that around $f = 1/2$, the two lowest energy levels are well separated from the other higher levels and they are approaching each other and thus can be approximated as a two-level system $\{|g\rangle, |e\rangle\}$ [142, 143]. The two lowest lying states are quantum superpositions of two counter-circulating macroscopic persistent current states. So the Hamiltonian of this qubit can be written in the basis of the persistent currents $\{|\cup\rangle, |\bar{\cup}\rangle\}$

$$\mathcal{H}_{qb} = -\frac{\epsilon}{2}\tilde{\sigma}_z - \frac{\Delta}{2}\tilde{\sigma}_x, \quad (7.17)$$

where $\tilde{\sigma}_z = |\cup\rangle\langle\cup| - |\bar{\cup}\rangle\langle\bar{\cup}|$ and $\tilde{\sigma}_x = |\cup\rangle\langle\bar{\cup}| + |\bar{\cup}\rangle\langle\cup|$. The coefficient

$$\epsilon = 2I_p \left(\Phi - \frac{\Phi_0}{2} \right) \quad (7.18)$$

is the magnetic energy of the qubit, with I_p being persistent current.

When the flux qubit is coupled a lumped LC resonator with a resonance mode ω_r at low temperature, the total Hamiltonian of the qubit and resonator system takes the form

$$\mathcal{H} = -\frac{1}{2} \left[2I_p \left(\Phi + \Phi_r - \frac{\Phi_0}{2} \right) \tilde{\sigma}_z + \Delta \tilde{\sigma}_x \right] + \hbar\omega_r a^\dagger a, \quad (7.19)$$

where

$$\Phi_r = M_r I_{rms} (a + a^\dagger) \quad (7.20)$$

is the magnetic flux generated by the resonator at the position of the qubit, M_r is the mutual inductance between the qubit and the resonator. The Hamiltonian Eq.(7.19) can be rewritten as [143]

$$\mathcal{H} = -\frac{1}{2} [\epsilon \tilde{\sigma}_z + \Delta \tilde{\sigma}_x] + \hbar \omega_r a^\dagger a - \hbar \tilde{g} \tilde{\sigma}_z (a + a^\dagger), \quad (7.21)$$

where the coupling strength is defined as $\tilde{g} = I_p I_{rms} M_r / \hbar$. Transforming Eq.(7.21) to the qubit eigenbasis $\{|g\rangle, |e\rangle\}$, we have

$$\mathcal{H} = \frac{\hbar \omega_a}{2} \sigma_z + \hbar \omega_r a^\dagger a + \hbar \tilde{g} (\cos \theta \sigma_z - \sin \theta \sigma_x) (a + a^\dagger), \quad (7.22)$$

with $\omega_a = \sqrt{\Delta^2 + \epsilon^2} / \hbar$, and $\tan \theta = \Delta / \epsilon$.

In rotating wave approximation, the $\sigma_z(a + a^\dagger)$ term in Eq.(7.22) oscillates with $e^{\pm i \omega_r}$ in the rotating frame compared with the slowly rotating terms $e^{\pm i(\omega_q - \omega_r)}$, and can be averaged out for small coupling strength. And we now obtain the Jaynes-Cummings model Eq.(7.6) for a flux qubit coupled to a resonator. However, for large enough coupling strength \tilde{g} , we may need to take into account the $\sigma_z(a + a^\dagger)$ term, and keep the full Hamiltonian Eq.(7.22).

7.3 Different coupling regimes in cavity & circuit QED

7.3.1 The two dissipative processes

In addition to the Jaynes-Cummings Hamiltonian in Eq.(7.6), the small cavity QED system is also influenced by two dissipative processes: the first one is associated with the coupling of the atom to the free-space electromagnetic background, and the second one to the coupling of the cavity mode to the outside world via mirror losses and diffraction, see Fig.(7.1(a)). The first process is particularly important in open cavities, and results in an incoherent decay of the excited atomic state, while mirror losses and diffraction lead to the irreversible escape of cavity photons. The full analysis of such two decay mechanisms can be done in the similar way as described in Sec.(3.1): the small atom-cavity mode system is coupled to two thermal reservoirs that model the electromagnetic background and the mirror losses as continua of harmonic oscillators. At zero

temperature, the dynamics of the small system is described by the *master equation* [98, p.429]

$$\dot{\rho}_s = -\frac{i}{\hbar}[H_{eff}\rho_s - \rho_s H_{eff}^\dagger] + \kappa a \rho_s a^\dagger + \gamma' \sigma_- \rho_s \sigma_+, \quad (7.23)$$

where the effective non-Hermitian Hamiltonian is

$$H_{eff} = H_{JC} + H_{loss}, \quad (7.24)$$

$$H_{loss} = H_\kappa + H_\gamma = -\frac{i\hbar}{2} (\gamma' \sigma_+ \sigma_- + \kappa a^\dagger a). \quad (7.25)$$

H_κ describes the coupling of the cavity to the continuum which produces the cavity decay rate $\kappa = \omega_r/Q$, Q is the quality factor of a cavity resonator. H_γ describes the coupling of the atom to the continuum of modes of the vacuum other than the cavity mode which cause the excited state to decay at rate γ' . In principle, the cavity decay rate κ_j is mode dependent, by which it means a photon in j -mode in the cavity escapes to the continuum of modes of free space which it is coupled to. This causes the resonance lines of the cavity to acquire a certain width $\delta\omega_j \sim \kappa_j$. In order to couple a single mode of the cavity to an atom, the condition $\delta\omega_j < |\omega_j - \omega_{j-1}|$ (modes do not overlap) needs to be fulfilled [143].

The total excitation is conserved in the Jaynes-Cummings model between the atom and the cavity mode, but the coupling to the reservoirs involves an irreversible loss of excitation from the atom-cavity small system. Consequently, for an initially excited atom in an empty cavity, there are only three relevant states involved in its dynamics, the ‘‘one-quantum’’ states $|e, 0\rangle$ and $|g, 1\rangle$, and the ‘‘zero-quanta’’ state $|g, 0\rangle$. Since the coupling between these two manifolds irreversibly populates the zero-quanta subspace, we can introduce the unnormalized ‘‘one-quantum’’ state

$$|\psi(t)\rangle = C_e(t) |e, 0\rangle + C_g(t) |g, 1\rangle, \quad (7.26)$$

whose evolution is governed by the non-hermitian Schrödinger equation

$$i\hbar \frac{\partial |\psi(t)\rangle}{\partial t} = H_{eff} |\psi(t)\rangle. \quad (7.27)$$

The corresponding equations of motion for the probability amplitudes $C_e(t)$ and $C_g(t)$ in the

interaction picture with respect to H_0 are

$$\dot{C}_e(t) = -ig e^{i\Delta t} C_g(t) - \frac{\gamma'}{2} C_e(t), \quad (7.28)$$

$$\dot{C}_g(t) = -ig e^{-i\Delta t} C_e(t) - \frac{\kappa}{2} C_g(t). \quad (7.29)$$

As shown above, the key parameters describing the cavity QED system are the cavity resonance frequency ω_r , the atomic transition frequency ω_a , and the strength of the atom-photon coupling g , the atomic free space decay rate γ' , the cavity decay rate κ . Depending on whether the loss rates κ , γ' or interaction rate g are dominating the system is either in the weak or the strong coupling regime. When either of the two dissipation dominates over the atom-cavity coupling, the system is in traditionally called *weak coupling regime*, or bad cavity regime. In contrast, *the strong coupling regime*, or good cavity regime, is characterized by the fact that the coherent interaction between the atom and the cavity mode dominates over the irreversible decay mechanisms. If the cavity is perfectly closed as often used in microwave experiments, the atom only sees the discrete electromagnetic modes of the cavity and $\gamma' = 0$. Therefore the weak coupling regime corresponds to $g \ll \kappa$ and the strong coupling regime $g \gg \kappa$. In contrast, most optical cavities encompass only a small fraction of the free-space solid angle 4π , so that $\gamma' \simeq \gamma_0$. In this case, the the weak coupling regime corresponds to $g \ll \kappa, \gamma_0$ and the strong coupling regime to $g \gg \kappa, \gamma_0$.

7.3.2 Weak coupling regime: The Purcell effect

The integration of Eq.(7.29) gives

$$C_g(t) = -ig e^{-\frac{1}{2}\kappa t} \int_0^t dt' C_e(t') e^{-(i\Delta - \kappa/2)t'}. \quad (7.30)$$

We can see from Eq.(7.30) that $C_e(t)$ will be a slow variable provided that g and γ' are small compared to $|\Delta| + |\kappa|/2$, and can be evaluated as $C_e(t) \approx C_e(t')$ and brought outside the integral.

The remaining integral gives,

$$C_g(t) = \frac{ig}{i\Delta - \kappa/2} e^{-i\Delta t} C_e(t). \quad (7.31)$$

The substitution of Eq.(7.31) into Eq.(7.28) gives

$$\dot{C}_e(t) = - \left[\frac{\gamma'}{2} + \frac{g^2(\kappa/2 + i\Delta)}{\Delta^2 + \kappa^2/4} \right] C_e(t). \quad (7.32)$$

Therefore, the upper electronic state population $P_e(t)$ undergoes an exponential decay at the rate $\gamma = \gamma' + \gamma_c$, where the cavity contribution to the decay rate is

$$\gamma_c = \left(\frac{4g^2}{\kappa} \right) \frac{1}{1 + 4\Delta^2/\kappa^2}. \quad (7.33)$$

This is known as the Purcell effect [144] and with this expression one finds:

- *Enhanced spontaneous emission* for an atom in resonance with the cavity $\Delta = 0$:

$$\gamma_c^{max} = \frac{3Q}{4\pi^2} \left(\frac{\lambda_r^3}{V} \right) \gamma_0, \quad (7.34)$$

- *Suppressed spontaneous emission* for an atom far detuned from the cavity frequency, i.e.

$|\Delta| = \omega_r$, we have for $Q \ll 1$:

$$\gamma_c \simeq \gamma_c^{max} \left(\frac{1}{4Q^2} \right) \gamma_c^{max} = \frac{3}{16\pi^2 Q} \left(\frac{\lambda_r^3}{V} \right) \gamma_c^{max}. \quad (7.35)$$

$\lambda_r = 2\pi c/\omega_r$ is the wavelength of the cavity field.

The enhancement and suppression of atomic decay have been demonstrated for the first time in experiments by Haroche [145] and Kleppner [146].

7.3.3 Strong coupling regime: Damped Rabi oscillations

The Eqs.(7.28,7.29) can be rewritten as

$$\ddot{C}_e(t) + \left(\frac{\kappa}{2} + \frac{\gamma'}{2} - i\Delta \right) \dot{C}_e(t) + \left(g^2 + \frac{\kappa\gamma'}{4} - i\frac{\gamma'\Delta}{2} \right) C_e(t) = 0, \quad (7.36)$$

$$\ddot{C}_g(t) + \left(\frac{\kappa}{2} + \frac{\gamma'}{2} + i\Delta \right) \dot{C}_g(t) + \left(g^2 + \frac{\kappa\gamma'}{4} - i\frac{\kappa\Delta}{2} \right) C_g(t) = 0, \quad (7.37)$$

and then the general solution of for arbitrary g, γ', κ is of the form

$$C_e(t) = C_{e1} e^{r_{e1}t} + C_{e2} e^{r_{e2}t}, \quad (7.38)$$

$$C_g(t) = C_{g1} e^{r_{g1}t} + C_{g2} e^{r_{g2}t}, \quad (7.39)$$

where

$$r_{e1,e2} = -\frac{1}{2} \left(\frac{\kappa}{2} + \frac{\gamma'}{2} - i\Delta \right) \pm \frac{1}{2} \left[\left(\frac{\kappa}{2} + \frac{\gamma'}{2} - i\Delta \right)^2 - 4 \left(g^2 + \frac{\kappa\gamma'}{4} - i \frac{\gamma'\Delta}{2} \right) \right]^{1/2}, \quad (7.40)$$

$$r_{g1,g2} = -\frac{1}{2} \left(\frac{\kappa}{2} + \frac{\gamma'}{2} + i\Delta \right) \pm \frac{1}{2} \left[\left(\frac{\kappa}{2} + \frac{\gamma'}{2} + i\Delta \right)^2 - 4 \left(g^2 + \frac{\kappa\gamma'}{4} - i \frac{\kappa\Delta}{2} \right) \right]^{1/2}, \quad (7.41)$$

and the constants $C_{e1,e2}, C_{g1,g2}$ are determined from the initial and the normalization conditions.

In the strong coupling regime $g \gg \kappa, \gamma'$ these exponents reduce to

$$r_{e1,e2} = -\frac{1}{2} \left(\frac{\kappa}{2} + \frac{\gamma'}{2} - i\Delta \right) \pm ig, \quad (7.42)$$

$$r_{g1,g2} = -\frac{1}{2} \left(\frac{\kappa}{2} + \frac{\gamma'}{2} + i\Delta \right) \pm ig. \quad (7.43)$$

The amplitude of the imaginary part of the exponents in Eqs.(7.42, 7.43) is much larger than that of the real part, so that the evolution of the atomic population will consist of oscillations at the vacuum Rabi frequency which slowly decay in time. This dependence is illustrated in Fig.(7.3)

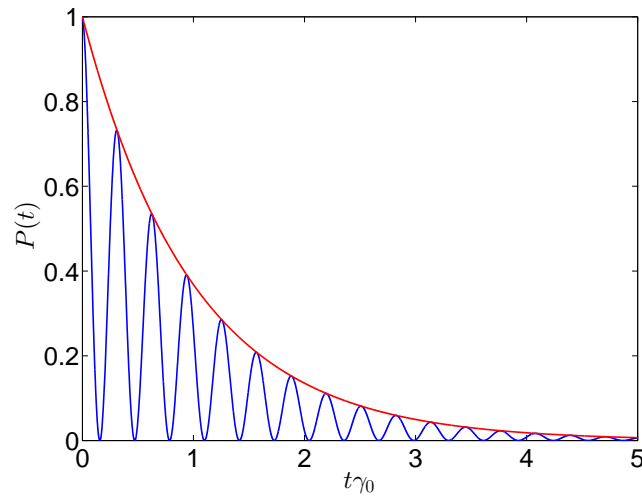


Figure 7.3: Damped oscillation for atomic excited state probability in the strong coupling regime with initially excited state and $g = 10\gamma' = 10\kappa, \gamma' \simeq \gamma_0$. The exponentially decaying red curve correspond to spontaneous emission.

as an example with an initially excited state.

It is clear from the Fig.(7.3) that, in the strong coupling regime when the atom-cavity coupling dominates over the dissipation processes, a photon emitted by the atom into the cavity can be reabsorbed and recovered after a full period π/g . The quantum coherence is preserved within the coherence time $1/\kappa, 1/\gamma_0$.

7.3.4 Beyond rotating wave approximation: The Rabi model

So far the Jaynes-Cummings model has been very successful in cavity QED, since it accurately predicts a wide range of experiments using optical or microwave cavities, where the rotating wave approximation is justified, because the coupling strength between the atom and the field is several orders of magnitude smaller than the frequencies of both the qubit and the cavity [63]. However, nowadays solid-state semiconductor [147] or superconductor systems [88–90, 148–150] have allowed the advent of the *ultrastrong coupling (USC) regime*, where the coupling strength is comparable to or larger than appreciable fractions of the mode frequency: $0.1 \lesssim g/\omega_r \lesssim 1$. Confident of the impressive fast development of current technology, one could explore further regimes where the rate between the coupling strength and oscillator frequency could reach $g/\omega_r \gtrsim 1$, which is called *deep strong coupling (DSC) regime* [151]. This unusual regime, yet to be experimentally explored, is the focus of our current efforts.

In this two regimes, the rotating-wave approximation breaks down and novel phenomena arise. For example, the dropped terms $\sigma^+ a^\dagger, \sigma^- a$ can lead to a noticeable shift in the resonance frequency (the Bloch-Siegert shift [90]) and the interplay of chaotic regimes, among others. The system in this case is described by the Rabi Hamiltonian model as in Eq.(7.4),

$$H_{Rabi} = \hbar\omega_r a^\dagger a + \frac{1}{2}\hbar\omega_a \sigma_z + \hbar g (\sigma_+ + \sigma_-)(a + a^\dagger),$$

which is only analytical solved recently by Braak [152]. Instrumentally, we can understand the system evolves inside the Hilbert space that can be split into two unconnected subspaces or parity

chains [151],

$$|g0_a\rangle \leftrightarrow |e1_a\rangle \leftrightarrow |g2_a\rangle \leftrightarrow |e3_a\rangle \leftrightarrow \dots (p = +1), \quad (7.44)$$

$$|e0_a\rangle \leftrightarrow |g1_a\rangle \leftrightarrow |e2_a\rangle \leftrightarrow |g3_a\rangle \leftrightarrow \dots (p = -1), \quad (7.45)$$

where the neighboring states within each parity chain may be connected via either rotating or counter-rotating terms.

7.4 Validity of controlled-phase gates in the ultrastrong coupling regime

The great achievements in circuit QED in USC and DSC regimes open the possibility to achieve ultrafast gates operating at subnanosecond time scales [153–155]. However, since most of the existing quantum two-qubit gate protocols are based on rotating-wave approximation which breaks down in the USC and DSC regimes, reexamination of those protocols is required. The two-qubit gate protocols in cavity/circuit QED can be divided into two kinds according to their operating regimes: the resonant regime and the dispersive regime. They can be distinguished by comparing the Rabi frequency g (quantized field) or Ω (classical field) to the detuning Δ between the transition frequency of the two-level system and the frequency of light field. For resonant case with $\Delta = 0$, the gate operation time is in general on the order of π/g (π/Ω). For the dispersive regime with $g \ll \Delta$ ($\Omega \ll \Delta$), the corresponding effective coupling strength is $g_{eff} = g^2/\Delta$ ($\Omega_{eff} = \Omega^2/\Delta$), and the gate operation time is on the order of π/g_{eff} (π/Ω_{eff}) [63]. The dispersive condition implies $g_{eff} \ll g$ ($\Omega_{eff} \ll \Omega$), so that in any case, an operation in the dispersive regime is always slower than an operation in the resonant regime. For the purpose of making fast gate operations, here we only consider the behavior of resonant gates with increasing coupling strength.

In this section, we investigate theoretically the performance of two-qubit resonantly controlled phase (CPHASE) gates in the crossover from the strong to the ultrastrong coupling regime of light-matter interaction in circuit QED. Two CPHASE schemes, which work well within the rotating-wave approximation, are analyzed taking into account the effects of counter-rotating

terms appearing in the Hamiltonian.

7.4.1 Two-qubit controlled-phase (CPHASE) gate

In the computational basis of two atomic qubits $\{|g_1, g_2\rangle, |g_1, e_2\rangle, |e_1, g_2\rangle, |e_1, e_2\rangle\}$, a general two-qubit controlled phase gate is described by the unitary transformation

$$U_{CPHASE} = \begin{pmatrix} 1 & 0 & 0 & 0 \\ 0 & 1 & 0 & 0 \\ 0 & 0 & 1 & 0 \\ 0 & 0 & 0 & e^{i\theta} \end{pmatrix}, \quad (7.46)$$

where $|g_i\rangle$ and $|e_i\rangle$ ($i = 1, 2$) are the ground and excited states of the i -th qubit. In particular, when $\theta = \pi$, the above unitary transformation leads to a controlled π -phase gate, that together with single-qubit rotations form a set of universal gates for quantum computation [1, p.188].

7.4.2 Analysis of the CPHASE gate performance for scheme I

In this part, we study the performance of the scheme proposed in Ref. [156] for different values of the interaction strength between qubits and resonator field. The protocol is based on the resonant interaction of three-level superconducting qubits and a single mode of the resonator. Here, we assume that the qubit transition frequency can be tuned in order to switch selectively on and off its coupling to the resonator. The logical qubits are encoded into the two lowest energy levels $|g_i\rangle, |e_i\rangle$, while the third state $|a_i\rangle$ is used as an auxiliary level.

This first protocol is displayed schematically in Fig.(7.4) and Table.(7.1).

Table 7.1: Operation steps of the CPHASE gate protocol I.

Step	Transition	Coupling	Pulse
(i) Mapping	$ e_2, 0\rangle \rightarrow -i g_2, 1\rangle$	g_{g_2, e_2}	$\pi/2$
(ii) CPHASE	$ e_1, 1\rangle \rightarrow - e_1, 1\rangle$	g_{e_1, a_1}	π
(iii) Back Mapping	$ g_2, 1\rangle \rightarrow -i e_2, 0\rangle$	g_{g_2, e_2}	$3\pi/2$

Let us suppose that the initial state of the system reads

$$|\psi_{in}\rangle = (b_1 |g_1, g_2\rangle + b_2 |g_1, e_2\rangle + b_3 |e_1, g_2\rangle + b_4 |e_1, e_2\rangle) \otimes |0\rangle, \quad (7.47)$$

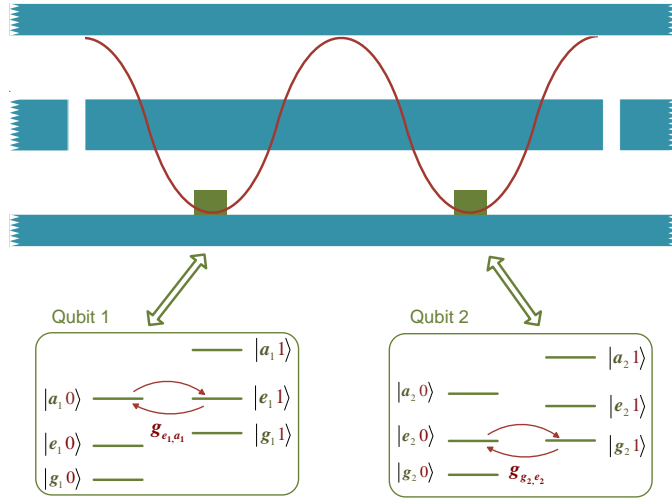


Figure 7.4: Schematic of the protocol I for a resonant CPHASE gate.

where b_i ($i = 1, \dots, 4$) are the arbitrary complex coefficients.

Within the realm of cavity & circuit QED, it is often the case that the interaction between qubits and resonator field can be described using the Jaynes-Cummings model, where the coupling strength is small enough so that the RWA is applicable. In such a case the state evolves to

$$|\psi_{out}\rangle = \left(b_1 |g_1, g_2\rangle + b_2 |g_1, e_2\rangle + b_3 |e_1, g_2\rangle - b_4 |e_1, e_2\rangle \right) \otimes |0\rangle, \quad (7.48)$$

leading to a controlled π -phase gate operation.

A natural question is whether this protocol can be extended to higher values of coupling strength, where the interaction lies in the ultrastrong coupling regime. This is a relevant question for quantum computation, as it would lead to faster gate operations. We have analyzed the fidelity of the above protocol considering the ultrastrong coupling regime, where the RWA breaks down.

In this case, the Hamiltonian of the system reads

$$H_{nrwa}^q = \sum_{j=g,e,a}^{i=1,2} E_{ji} |j_i\rangle\langle j_i| + \hbar\omega_r a^\dagger a + \hbar g_{e_1, a_1} \sigma_{e_1, a_1}^x (a + a^\dagger) + \hbar g_{g_2, e_2} \sigma_{g_2, e_2}^x (a + a^\dagger), \quad (7.49)$$

where $\sigma_{k,l}^x = |l\rangle\langle k| + |k\rangle\langle l|$, E_{ji} is the energy of the j -th level for the i -th qubit, and the g_{e_1, a_1} , g_{g_2, e_2} are the corresponding coupling strengths.

Taking the state Eq.(7.48) as the ideal one to compare with the resulting state of the protocol when including counter-rotating terms in the qubit-resonator interaction, the fidelity can be

computed as

$$F = |\langle \psi_{rwa} | \psi_{nrwa} \rangle|^2 = |\langle \psi_{in} | U_{rwa}^\dagger U_{nrwa} | \psi_{in} \rangle|^2, \quad (7.50)$$

where U_{rwa} , $|\psi_{rwa}\rangle$ and U_{nrwa} , $|\psi_{nrwa}\rangle$ are the evolution operator and final state in RWA and non-RWA cases, respectively.

For the sake of simplicity, we assume the couplings strength between each qubit and the resonator are equal, $g_{e_1, a_1} = g_{g_2, e_2} = g$, and study the case of an initial maximally entangled state

$$|\psi'_{in}\rangle = \frac{1}{\sqrt{2}} (|g_1, g_2\rangle + |g_1, e_2\rangle + |e_1, g_2\rangle + |e_1, e_2\rangle) \otimes |0\rangle. \quad (7.51)$$

The fidelity of the operation as a function of the normalized coupling strength g/ω_r is shown in Fig.(7.5). Our simulation shows that the fidelity of the gate operation decreases fast while increasing the coupling strength. For a ratio $g/\omega_r = 0.065$, the fidelity drops below 0.99, while for $g/\omega_r = 0.12$ —which was reached in recent experiments [89, 90]—the fidelity goes down to $F \approx 0.968$, and for $g/\omega_r = 0.2$, the fidelity is only $F \approx 0.89$. These results mean that, although this protocol could be still used with state-of-the-art circuit QED technology [89, 90], its fidelity drops gently as the coupling strength is increased beyond these values.

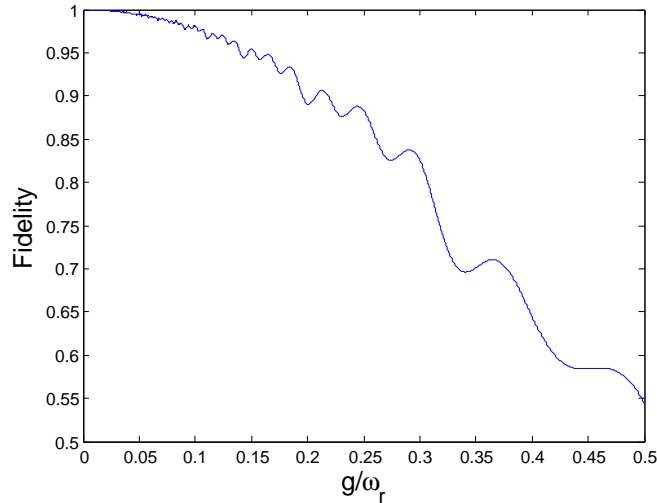


Figure 7.5: Fidelity versus normalized coupling strength g/ω_r for the CPHASE gate in protocol I with maximally entangled initial state.

7.4.3 Analysis of the CPHASE gate performance for scheme II

In this part, we propose an alternative scheme based on a similar configuration, but adding an external microwave field driving the transition $|e_1\rangle \leftrightarrow |a_1\rangle$ of the first qubit, which will assist the gate operation besides the qubit-resonator interaction. The advantage of this modified protocol is that it does not require the accurate adjustment of the qubit transition frequency. The different steps of this scheme are depicted in Fig.(7.6) and Table.(7.2) — where a single subsystem has a three-level structure.

Within the rotating-wave approximation, protocol II produces the final state

$$|\psi_{out}\rangle = (b_1 |g_1, g_2\rangle + b_2 |g_1, e_2\rangle - b_3 |e_1, g_2\rangle + b_4 |e_1, e_2\rangle) \otimes |0\rangle, \quad (7.52)$$

which has a π -phase shift on state $|e_1, g_2\rangle$. To go beyond the rotating-wave approximation in the scheme, we must take into account counter-rotating terms of both qubit-resonator interaction as well as semi-classical model to describe the qubit and classical microwave field interaction.

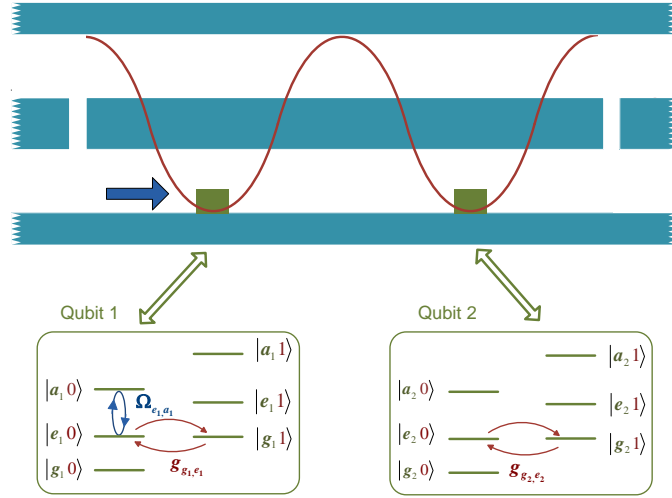


Figure 7.6: Sketch of protocol II for a resonant CPHASE gate.

Table 7.2: Operation steps of the CPHASE gate protocol II.

Step	Transition	Coupling	Pulse
(i) Mapping	$ e_2, 0\rangle \rightarrow -i g_2, 1\rangle$	g_{g_2, e_2}	$\pi/2$
(ii) Rotate qubit 1	$ e_1\rangle \rightarrow -i a_1\rangle$	Ω_{e_1, a_1}	$\pi/2$
(iii) CPHASE	$ g_1, 1\rangle \rightarrow - g_1, 1\rangle$	g_{g_1, e_1}	π
(iv) Back Rotate qubit 1	$ a_1\rangle \rightarrow -i e_1\rangle$	Ω_{e_1, a_1}	$\pi/2$
(v) Back Mapping	$ g_2, 1\rangle \rightarrow -i e_2, 0\rangle$	g_{g_2, e_2}	$\pi/2$

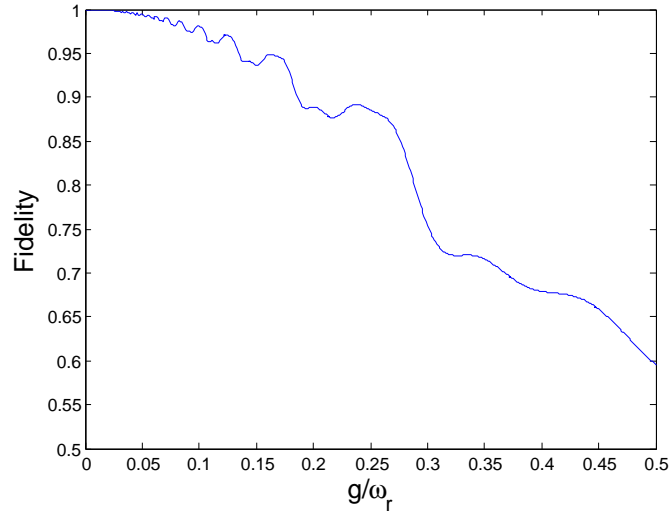


Figure 7.7: Fidelity versus normalized coupling strength g/ω_r for the CPHASE gate in scheme I with maximally entangled initial state.

The Hamiltonian for semi-classical model in the Schrödinger picture and without rotating-wave approximation reads

$$H_{nrwa}^c = E_{e_1} |e_1\rangle\langle e_1| + E_{a_1} |a_1\rangle\langle a_1| + \hbar\Omega_{e_1,a_1} \sigma_{e_1,a_1}^x \left(e^{i\omega_L t} + e^{-i\omega_L t} \right), \quad (7.53)$$

with $\Omega_{e_1,a_1} = d_{e_1,a_1} \xi_0/\hbar$ being the Rabi oscillation frequency, and ω_L, ξ_0 being the frequency and amplitude of the classical driving field respectively. Likewise, the corresponding Hamiltonian in rotating frame with respect to qubit frequency one reads

$$\tilde{H}_{nrwa}^c = \Omega_{e_1,a_1} \sigma_+ \left(e^{-i(\omega_L - \omega_{e_1,a_1})t} + e^{i(\omega_L + \omega_{e_1,a_1})t} \right) + \Omega_{e_1,a_1} \sigma_- \left(e^{i(\omega_L - \omega_{e_1,a_1})t} + e^{-i(\omega_L + \omega_{e_1,a_1})t} \right) \quad (7.54)$$

where $\omega_{e_1,a_1} = E_{a_1} - E_{e_1}$ is the transition frequency between levels $|e_1\rangle$ and $|a_1\rangle$.

The wave function in the rotating frame can be written as

$$|\psi'_{(t)}\rangle = C_{e_1}(t) |e_1\rangle + C_{a_1}(t) |a_1\rangle, \quad (7.55)$$

where $C_{e_1}(t)$ and $C_{a_1}(t)$ are the complex coefficients for the excited state and auxiliary state,

respectively. The corresponding evolution equation for these amplitudes are

$$\dot{C}_{e_1}(t) = -i\Omega_{e_1,a_1} \left(e^{i(\omega_L - \omega_{e_1,a_1})t} + e^{-i(\omega_L + \omega_{e_1,a_1})t} \right) C_{a_1}(t) \quad (7.56)$$

$$\dot{C}_{a_1}(t) = -i\Omega_{e_1,a_1} \left(e^{-i(\omega_L - \omega_{e_1,a_1})t} + e^{i(\omega_L + \omega_{e_1,a_1})t} \right) C_{e_1}(t). \quad (7.57)$$

We have analyzed numerically the protocol fidelity as a function of the ratio g/ω_r . As shown in Fig.(7.7), it is clear that the fidelity decays in a similar fashion as the previous one, as the normalized coupling strength increases, assuming that $\Omega_{e_1,a_1} = g$. Thus this protocol is also unsuitable considering coupling strengths of about $g/\omega_r > 0.15$, well within the ultrastrong coupling regime. Therefore, with the fast experimental developments in achieving larger and larger light-matter coupling strength [151, 152, 157], our numerical analysis suggests a need to develop new protocols for quantum gates beyond the rotating wave approximation, making possible the design of ultrafast quantum gate operations [158] for quantum information processing.

7.4.4 Discussion

Here we discuss the implementation and the complexity of the two CPHASE protocols.

Nowadays, the controllability of superconducting devices made of Josephson junctions, has led to the implementation of different types of superconducting qubits described by phase, charge, or flux degrees of freedom [41], respectively. This fast growing technology now allows the access to the coherent control of these artificial atoms in a three-level configuration, as have shown with transmons [159], the phase qubit [76], and the flux qubit [127], which support the implementation of those protocols in various kinds of superconducting circuits.

Besides, the complexity of the protocols is manifested by the degree of difficulty in manipulation, i.e. the number of the pulse sequences needed to perform. Although in our protocols three or four steps are needed to perform the gate, and an external field is used to assist the operation, we do not require direct qubit-qubit interaction as compared with the two-qubit algorithms demonstrated in Ref. [75]. In that scheme, the qubit-qubit coupling is realized by a virtual excitation of an intra-cavity field and this second-order based coupling results in a slower operation. In another experimental realization, the two-qubit controlled-Z and controlled-NOT gates were realized [76] by making use of an extra capacitor mediating the coupling between qubits.

Ultrafast Quantum Gates in Circuit QED

From chapter 7, we see that the ultrastrong coupling developments in circuit QED [89, 90], not only bring us the opportunity of faster gate operations on sub-nanoseconds, but also the strong demand for new gate protocol. In this chapter, we propose a realistic scheme to realize ultrafast two-qubit controlled phase gates between two newly designed flux qubits [142], coupled galvanically to a single-mode transmission line resonator, as shown in Fig.(8.10), which is valid for the ultrastrong coupling and deep strong coupling regimes of light-matter interaction. Our scheme includes two parts:

- the designed ultrastrongly coupled qubit-resonator system in Sec.(8.1,8.2,8.3), which allows for high controllability on both the qubit transition frequency and the qubit-resonator coupling, in USC [89,90] and potentially the DSC regime [151] of light-matter interaction;
- a two-qubit controlled phase gate protocol in Sec.(8.4), which operates at times proportional to the inverse of the resonator frequency.

8.1 The design of a versatile flux qubit

As already shown both theoretically [88] and experimentally [89, 149], circuit QED architecture with a superconducting flux qubit coupled directly to the center conductor of a coplanar waveguide transmission-line resonator leads to strong and ultrastrong coupling regimes. By inserting a

Josephson junction in the center conductor of the resonator, much stronger couplings can be obtained because of the enhancement of phase bias in the vicinity of the junction.

Our designed flux qubit consists of a six-Josephson-junctions configuration depicted schematically in Fig.(8.1), each one denoted by a cross, coupled galvanically [89,90,149] to a coplanar waveguide resonator. The upper f_1 -loop stands for a three-junction flux qubit [142], while the additional $f_{2,3}$ -loops allow a tunable qubit-resonator coupling strength.

We choose junction 1 and 2 to be same and Junction 4 and 5 to be same, $C_{J1} = C_{J2} = C_J$, $C_{J3} = \alpha C_J$, $C_{J4} = C_{J5} = \alpha_4 C_J$, $E_{J1} = E_{J2} = E_J$, $E_{J3} = \alpha E_J$, $E_{J4} = E_{J5} = \alpha_4 E_J$. In the following, we analyze this qubit design in steps, where the sixth junction is characterized by a phase bias $\Delta\varphi$, and its energy will be include in the description of the transmission line resonator later.

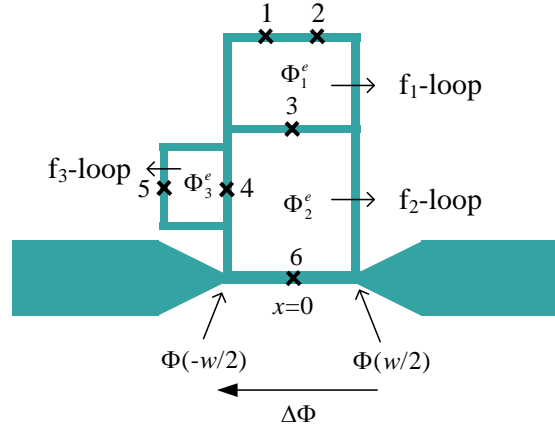


Figure 8.1: Circuit-QED configuration consisting on a six-Josephson-junctions array coupled galvanically to a single-mode resonator (bottom horizontal line).

8.1.1 The potential energy of the qubit

First, we describe the potential energy coming from the inductive terms, which is the dominant contribution and obtained by adding the corresponding Josephson potentials. The flux quantization relation Eq.(6.12) around closed loop gives the phase quantization relations for the corresponding

superconducting loops

$$f_1 - \text{loop:} \quad \varphi_1 - \varphi_2 + \varphi_3 = 2\pi f_1, \quad (8.1)$$

$$f_2 - \text{loop:} \quad \varphi_4 - \Delta\varphi - \varphi_3 = 2\pi f_2, \quad (8.2)$$

$$f_3 - \text{loop:} \quad \varphi_5 - \varphi_4 = 2\pi f_3, \quad (8.3)$$

where the frustration parameter is $f_k = \Phi_k^e/\Phi_0$ ($k = 1, 2, 3$). The time dynamics of those phase operators are

$$\dot{\varphi}_3 = \dot{\varphi}_2 - \dot{\varphi}_1, \quad (8.4)$$

$$\dot{\varphi}_4 = \dot{\varphi}_2 - \dot{\varphi}_1 + \Delta\dot{\varphi}, \quad (8.5)$$

$$\dot{\varphi}_5 = \dot{\varphi}_4. \quad (8.6)$$

The total potential energy of the designed qubit modified by the phase slip from the shared junction reads

$$\begin{aligned} \mathcal{U}'_q &= -\sum_{j=1}^5 E_{Jj} \cos \varphi_j = -E_J (-\cos \varphi_1 + \cos \varphi_2 + \alpha \cos \varphi_3 + \alpha_4 \cos \varphi_4 + \alpha_4 \cos \varphi_5), \\ &= -E_J \left[\cos \varphi_1 + \cos \varphi_2 + \alpha \cos (\varphi_2 - \varphi_1 + 2\pi f_1) + 2\alpha_4(f_3) \cos (\varphi_2 - \varphi_1 + 2\pi \tilde{f} + \Delta\varphi) \right], \end{aligned} \quad (8.7)$$

with $\alpha_4(f_3) \equiv \alpha_4 \cos(\pi f_3)$, $\tilde{f} = f_1 + f_2 + f_3/2$. The last term gives the inductively coupling between the qubit and resonator, and the parameters α , α_4 and f_j can be optimized for a suitable working point.

8.1.2 The kinetic energy of the qubit

The electric energy stored in the circuit comes from the five Josephson junctions in the circuit.

The voltage across each junction is given by the Josephson voltage-phase relation $V_j = \dot{\Phi}_j$.

$$\begin{aligned}\mathcal{T}'_q &= \frac{1}{2} \sum_{j=1}^5 C_{Jj} V_j^2 = \frac{1}{2} \sum_{j=1}^5 C_{Jj} \dot{\Phi}_j^2 \\ &= \frac{C_J}{2} (1 + \alpha + 2\alpha_4) (\dot{\Phi}_1^2 + \dot{\Phi}_2^2) - C_J (\alpha + 2\alpha_4) \dot{\Phi}_1 \dot{\Phi}_2 + 2\alpha_4 C_J \Delta \dot{\Phi} (\dot{\Phi}_2 - \dot{\Phi}_1) + \alpha_4 C_J (\Delta \dot{\Phi})^2,\end{aligned}\tag{8.8}$$

where the last second term gives the capacitive coupling between the qubit and resonator.

The Lagrangian of the qubit modified by the phase slip from the sixth junction reads

$$\mathcal{L}'_q = \mathcal{T}'_q - \mathcal{U}'_q,\tag{8.9}$$

where the qubit-resonator interaction has already been included.

8.2 The inhomogeneous transmission line resonator

In this section, we theoretically investigate the inhomogeneous transmission-line resonator perturbed by the sixth Josephson junction in the center conductor.

8.2.1 The Lagrangian of the interrupted resonator

As shown in Fig.(8.2), the inhomogeneous one-dimensional transmission line resonator is interrupted by the sixth Josephson junction at position $x = 0$. For a transmission line resonator (TLR) of length $2l$, we discretize it into $M = 2N$ equally spaced nodes, and the Lagrangian in discretized modes reads

$$\begin{aligned}\mathcal{L}_r &= \sum_{n=-N}^{n=-2} \left(\Delta x C_0 \frac{\dot{\Phi}_n^2}{2} - \frac{(\Phi_{n+1} - \Phi_n)^2}{2\Delta x L_0} \right) + \sum_{n=+2}^{n=+N} \left(\Delta x C_0 \frac{\dot{\Phi}_n^2}{2} - \frac{((\Phi_{n+1} - \Phi_n))^2}{2\Delta x L_0} \right) + \frac{\Delta x C_0}{2} (\dot{\Phi}_{-1}^2 + \dot{\Phi}_1^2) \\ &\quad + \frac{C_{J6}}{2} (\Phi_a - \Phi_b)^2 + E_{J6} \cos \left(2\pi \frac{\Phi_a - \Phi_b}{\Phi_0} \right) - \frac{(\Phi_a - \Phi_{-1})^2}{2\Delta x L_0} - \frac{(\Phi_{+1} - \Phi_b)^2}{2\Delta x L_0},\end{aligned}\tag{8.10}$$

with C_0 and L_0 being the characteristic capacitance and inductance per unit length, respectively.

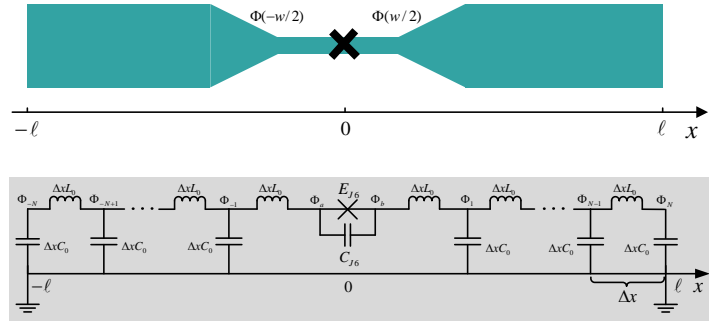


Figure 8.2: Schematics layout and the equivalent discretized circuit representation of a transmission line resonator with a Josephson junction inserted in the center conductor at position $x = 0$. The normal modes of the resonator is dressed by the junction's capacitance and linear inductance.

We can also work with continuous variable approach by defining the position-dependent flux variable as

$$\Phi(x, t) = \int_0^t dt' V(x, t'), \quad (8.11)$$

where $V(x, t) = \partial_t \Phi(x, t)$ is the local voltage on the transmission line at position x and time t . Each segment of the line of length dx has inductance $L_0 dx$, capacitance $C_0 dx$. The voltage drop along it is $-dx \partial_x \partial_t \Phi(x, t)$, the flux through this inductance is thus $-dx \partial_x \Phi(x, t)$ and the local value of the current is given by the constitutive equation

$$I(x, t) = -\frac{1}{L_0} \partial_x \Phi(x, t). \quad (8.12)$$

The Lagrangian for such a system of length $2l$ (ranging from $x = -l$ to $x = l$) is

$$\begin{aligned} \mathcal{L}_r = & \int_{-l}^{0^-} \left[\frac{C_0}{2} (\partial_t \Phi(x, t))^2 - \frac{1}{2L_0} (\partial_x \Phi(x, t))^2 \right] + \int_{0^+}^l \left[\frac{C_0}{2} (\partial_t \Phi(x, t))^2 - \frac{1}{2L_0} (\partial_x \Phi(x, t))^2 \right] \\ & + \frac{C_{J6}}{2} (\Delta \Phi)^2 + E_{J6} \cos \left(\frac{\Delta \Phi}{\phi_0} \right), \end{aligned} \quad (8.13)$$

where $\Delta \Phi = \Phi_b - \Phi_a$ is the flux bias across the sixth junction, and the corresponding phase slip reads $\Delta \varphi = \Delta \Phi / \phi_0$.

The momentum conjugate to $\Phi(x, t)$ is simply the charge density

$$Q(x, t) \equiv \frac{\partial \mathcal{L}_r}{\partial \dot{\Phi}(x, t)} = C_0 \dot{\Phi}(x, t) = C_0 V(x, t). \quad (8.14)$$

8.2.2 Normal modes decomposition

In this part, we are interested in finding the orthogonal basis of normal modes of oscillations of the transmission-line resonator dressed with the sixth junction. This is done by applying the Euler-Lagrange equation of motion Eq.(6.29) to the Lagrangian with respect to flux coordinate $\Phi(x, t)$, which results in the (massless) Klein-Gordon wave equation

$$\frac{\partial^2 \Phi(x, t)}{\partial t^2} - v_p^2 \frac{\partial^2 \Phi(x, t)}{\partial x^2} = 0 \quad (8.15)$$

where $v_p = 1/\sqrt{L_0 C_0}$ is the wave propagation velocity.

This can be solved by first decomposing the flux $\Phi(x, t)$ over (unitless) normal spatial modes

$$\Phi(x, t) = \sum_n \phi_n(t) u_n(x). \quad (8.16)$$

where $\phi_n(t)$ is the flux amplitude of eigenmode n oscillating at mode frequency $\omega_n = k_n v_p$ and $u_n(x)$ is the spatial mode function.

Substitute Eq.(8.16) back into the Klein-Gordon wave equation Eq.(8.15), we have

$$\frac{\partial^2 \phi_n(t)}{\partial t^2} + \omega_n^2 \phi_n(t) = 0, \quad (8.17)$$

$$\frac{\partial^2 u_n(x)}{\partial x^2} + k_n^2 u_n(x) = 0, \quad (8.18)$$

whose solutions $\{u_n(x), \omega_n\}$ form an orthogonal basis, and $k_n = \omega_n/v_p$ is the wave vector.

A general solution evolution for Eq.(8.18) can be written as

$$u_n(x) = A_n e^{ik_n x} + B_n e^{-ik_n x}, \quad (8.19)$$

with A_n, B_n being the normalization constants.

A special choice of decomposition of the flux $\Phi(x, t)$ in Eq.(8.16) subject to Eq.(8.17) would be the sinusoidal function $\phi_n(t) = e^{-i\omega_n t}$.

8.2.3 The enhanced phase biasing

For a qubit sharing a length of w with the resonator, the phase slip can be expressed as

$$\begin{aligned}\Delta\varphi &= \frac{\Delta\Phi}{\phi_0} = \frac{1}{\phi_0} [\Phi(x = w/2) - \Phi(x = -w/2)], \\ &= \frac{1}{\phi_0} \sum_n \delta_n \phi_n(t), \\ &\approx \frac{w}{\phi_0} L'_0(x = 0) I(x = 0)\end{aligned}\quad (8.20)$$

with the dimensionless spatial mode gap, evaluated at parts shared by the resonator and the f_2 -loop

$$\delta_n = u_n(x = w/2) - u_n(x = -w/2). \quad (8.21)$$

In general, the shared length is much smaller than the total resonator length $w \ll 2\ell$, such that the approximation $w \rightarrow 0$ is made for the characterization of the transmission line resonator. For the convenience of later use, we define $\delta_n^- = u_n(x = 0^+) - u_n(x = 0^-)$.

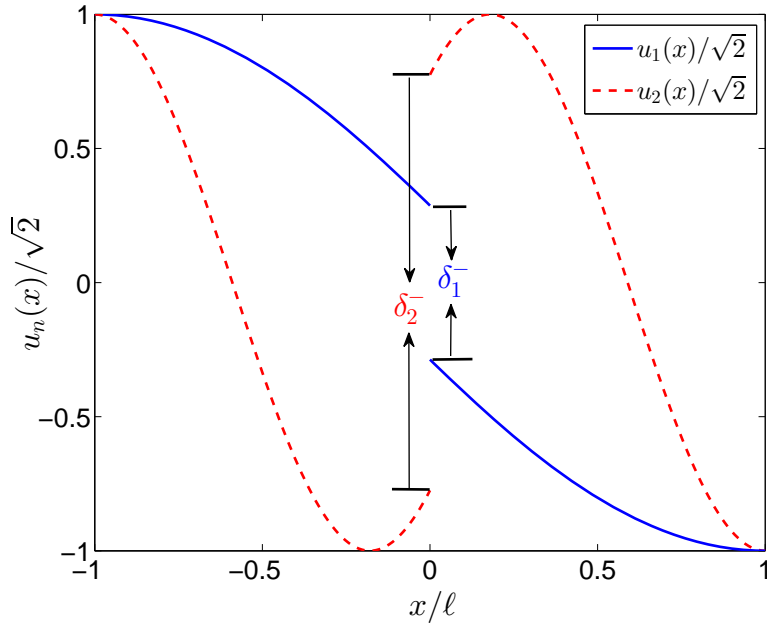


Figure 8.3: The normalised first and seconde normal mode envelopes for the interrupted resonator with a Josephson junction inserted in the center line at $x = 0$.

And $L'_0(x = 0)$ and $I(x = 0) = -\partial_x \Phi(x) / L'_0(x)|_{x=0}$ are, the inductance per unit length and the current in the resonator at the location $x = 0$ of the qubit, respectively. As the constriction

in the center conductor of the resonator is made narrower, and thus the local inductance made larger, especially a Josephson junction inserted in the center line will further increase the local inductance thus result in an abrupt change in the spatial mode $u_n(x)$, as seen in Fig.(8.3). A flux qubit connected on either side of the constriction, as illustrated in Fig.(8.1), will thus be strongly phase biased. As a result of the inhomogeneity in the resonator, the qubit-resonator coupling can be increased and thus making the ultrastrong coupling regime possible.

8.2.4 Effect of boundary conditions

In particular, the boundary conditions of the resonator that strongly influence the mode basis is determined by the two ends $x = \pm l$ and the sixth junction's position $x = 0$.

A, *The open boundary (zero-current) condition: $I(x = \pm l, t) = 0$*

Assuming a large quality factor Q for the resonator, the open boundary (zero-current) conditions $I(x = \pm l, t) = 0$ tell us that the eigenfunctions have vanishing derivative at the boundaries.

$$\begin{aligned} \left. \frac{\partial \Phi}{\partial x} \right|_{x=\pm l} &= 0, \\ \partial_x u_n(x = \pm l) &= 0, \end{aligned} \quad (8.22)$$

which leads to

$$u_n(x) = \begin{cases} A_n \cos [k_n(x + l)] : & x < 0 \\ C_n \cos [k_n(x - l)] : & x > 0. \end{cases} \quad (8.23)$$

B, *Continuous current condition: $I(x = 0^+, t) = I(x = 0^-, t)$*

Moreover, the current on either side of the junction is equal $I(x = 0^+, t) = I(x = 0^-, t)$, which imposes

$$\begin{aligned} \frac{1}{L_0} \left. \frac{\partial \Phi}{\partial x} \right|_{x=0^-} &= \frac{1}{L_0} \left. \frac{\partial \Phi}{\partial x} \right|_{x=0^+}, \\ \partial_x u_n(x = 0^-) &= \partial_x u_n(x = 0^+). \end{aligned} \quad (8.24)$$

This gives us $A_n = -C_n$, and thus the spatial mode function can be simplified to

$$u_n(x) = A_n \begin{cases} \cos [k_n(x + l)] : & x < 0, \\ -\cos [k_n(x - l)] : & x > 0. \end{cases} \quad (8.25)$$

C, Orthogonality conditions:

The inner product of the spatial mode function $u_n(x)$ obeys

$$\begin{aligned} \langle u_m \cdot u_n \rangle &\equiv C_0 \int_{-\ell}^{0^-} dx u_n(x) u_m(x) + C_0 \int_{0^-}^{+\ell} dx u_n(x) u_m(x) + C_{J6} \delta_m^- \delta_n^-, \\ &= \tilde{C}_r \delta_{m,n}, \end{aligned} \quad (8.26)$$

where the total capacitance $\tilde{C}_r = C_r + C_{J6} = 2\ell C_0 + C_{J6}$ is modified by the sixth junction.

The normalization constant A_n can be fixed according to Eq.(8.26) as

$$A_n = \sqrt{\frac{\tilde{C}_r}{4C_J \cos^2 k_n \ell + C_r \left[\frac{1}{2} + \frac{\sin 2k_n \ell}{4k_n \ell} \right]}}. \quad (8.27)$$

It is also useful to define the inner product of spatial mode derivatives as they are found to obey a similar orthogonality condition

$$\begin{aligned} \langle \partial_x u_m \cdot \partial_x u_n \rangle &\equiv \frac{1}{L_0} \left(\int_{-\ell}^{0^-} dx [\partial_x u_n(x)] [\partial_x u_m(x)] + \int_{0^+}^{+\ell} dx [\partial_x u_n(x)] [\partial_x u_m(x)] \right) + \frac{1}{L_{J6}} \delta_m^- \delta_n^-, \\ &= \frac{1}{\tilde{L}_n} \delta_{m,n}, \end{aligned} \quad (8.28)$$

with the inductance $L_{J6} = \phi_0^2 / E_{J6}$. Here, we have defined the mode inductance $\tilde{L}_n^{-1} \equiv \tilde{C}_r \omega_n^2$ corresponding to the effective inductance of the resonator mode n taking into account the inductance provided by the sixth Josephson junction L_{J6} .

8.2.5 Quantization of transmission line resonator

It is clear that by using the normal mode decomposition Eq.(8.16) and the orthogonality relation Eqs.(8.26, 8.28), the Lagrangian Eq.(8.13) can be diagonalized by these spatial normal modes as

$$\mathcal{L}_r = \sum_n \frac{\tilde{C}_r}{2} (\dot{\phi}_n^2 - \omega_n^2 \phi_n^2), \quad (8.29)$$

where the second-order approximation has been made since the phase slip is small in general $|\Delta\varphi| \ll 1$.

The momentum conjugate to the normal mode amplitude ϕ_n is the charge

$$q_n = \frac{\partial \mathcal{L}}{\partial \dot{\phi}_n} = \tilde{C}_r \dot{\phi}_n, \quad (8.30)$$

and the corresponding Hamiltonian is

$$\mathcal{H}_r = \sum_n \left(\frac{q_n^2}{2\tilde{C}_r} + \frac{\tilde{C}_r}{2} \omega_n^2 \phi_n^2 \right). \quad (8.31)$$

From Eq.(8.31), we see that each normal mode becomes an independent simple harmonic oscillator.

By quantifying and introducing the operators

$$\phi_n = \sqrt{\frac{\hbar}{2\omega_n \tilde{C}_r}} (a_n^\dagger + a_n), \quad (8.32)$$

$$q_n = i \sqrt{\frac{\hbar \omega_n \tilde{C}_r}{2}} (a_n^\dagger - a_n), \quad (8.33)$$

with $[a_n, a_m^\dagger] = \delta_{nm}$, we arrive at the standard form Hamiltonian for harmonic oscillators,

$$\mathcal{H}_r = \sum_n \hbar \omega_n (a_n^\dagger a_n + 1/2), \quad (8.34)$$

completing the mapping of the inhomogeneous resonator to a sum of harmonic oscillators.

The quantized phase slip can be achieved by substituting Eq.(8.32) into Eq.(8.20),

$$\Delta\varphi = \sum_n \Delta\bar{\varphi}_n (a_n^\dagger + a_n), \quad (8.35)$$

with the magnitude of the phase slip being

$$\Delta\bar{\varphi}_n = \frac{\delta_n}{\phi_0} \sqrt{\frac{\hbar}{2\omega_n\tilde{C}_r}}. \quad (8.36)$$

8.2.6 Dispersion relation

Unlike the homogeneous resonators, the mode frequencies of this inhomogeneous resonator is unharmonically distributed such that $\omega_n \neq n\omega_0$. The dispersion relation of the wave factor k_n can be achieved from the continuous condition of the current flowing through the junction

$$\frac{1}{L_0} \frac{\partial\Phi}{\partial x} \Big|_{x=0^-} = \frac{1}{L_0} \frac{\partial\Phi}{\partial x} \Big|_{x=0^+} = C_{J6}\Delta\ddot{\Phi} + \Delta\varphi I_{c6}, \quad (8.37)$$

where the linear approximation $\sin \Delta\varphi \simeq \Delta\varphi$ has been made and $I_{c6} = E_{J6}/\phi_0$ being the critical current of the sixth junction.

Following the decomposition of the flux variable Eq.(8.16), we have

$$\left(-C_{J6}\omega_n^2 + \frac{1}{L_{J6}}\right) [u_n(x=0^+) - u_n(x=0^-)] = \frac{1}{L_0} \frac{\partial u_n(x)}{\partial x} \Big|_{x=0^-}, \quad (8.38)$$

$$2 \cos k_n \ell \times \left(-C_{J6}\omega_n^2 + \frac{1}{L_{J6}}\right) = \frac{k_n}{L_0} \sin k_n \ell. \quad (8.39)$$

This gives rise to the dispersion relation

$$k_n = \frac{2L_0}{L_{J6}} \left(1 - \frac{\omega_n^2}{\omega_{J6}^2}\right) \cot k_n \ell, \quad (8.40)$$

or write in another way as

$$k_n \ell \tan k_n \ell = \frac{L_r}{L_{J6}} \left(1 - \frac{4k_n^2 \ell^2}{C_r/C_{J6}}\right), \quad (8.41)$$

where $\omega_{J6} = 1/\sqrt{L_{J6}C_{J6}}$ is the plasma frequency and $\omega_n = k_n v_p = k_n/\sqrt{L_0 C_0}$.

8.3 The total qubit-resonator system

In this part, we analyze the total qubit-resonator system as shown in Fig.(8.4).

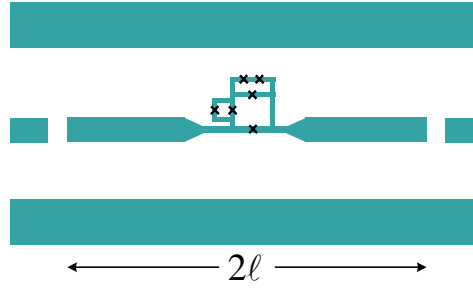


Figure 8.4: Circuit-QED configuration consisting of a six-Josephson-junctions array coupled galvanically to a single-mode resonator (bottom horizontal line).

8.3.1 The Hamiltonian of the qubit-resonator system

The Lagrangian of the total system (single qubit + resonator) is given by

$$\mathcal{L}_{tot} = \mathcal{L}'_q + \mathcal{L}_r. \quad (8.42)$$

In obtaining the Hamiltonian, we assume that the qubit does not significantly perturb the resonator such that the mode decomposition for $\Phi(x, t)$ found in Sec.(8.2) is a good approximation even in the presence of the qubit. This approximation is accurate for small qubit capacitances such that the capacitive terms in Eq.(8.42) do not induce large frequency shifts of the resonator, and if the inductance of the center line of the resonator of length w where the qubit is connected is smaller than the total inductance of the qubit. So that most of the current is flowing through the resonator. Both of these assumptions can safely be satisfied in practice with small junctions.

In the following, we assume only the first eigenmode of the resonator interacts the qubit, thus

$$\mathcal{L}_r \equiv \frac{\tilde{C}_r}{2} (\dot{\phi}^2 - \omega_r^2 \phi^2), \quad (8.43)$$

$$\Delta\Phi = \sum_n \delta_n \phi_n \equiv \delta\phi, \quad (8.44)$$

$$\mathcal{T}'_q = \frac{C_J(1 + \alpha + 2\alpha_4)}{2} (\dot{\Phi}_1^2 + \dot{\Phi}_2^2) - C_J(\alpha + 2\alpha_4)\dot{\Phi}_1\dot{\Phi}_2 + 2\alpha_4 C_J (\dot{\Phi}_2 - \dot{\Phi}_1)\delta\phi + \alpha_4 C_J \delta^2 \dot{\phi}^2, \quad (8.45)$$

and the corresponding quantized operators

$$\mathcal{H}_r \equiv \hbar\omega_r(a^\dagger a + 1/2), \quad (8.46)$$

$$\Delta\varphi = \frac{1}{\phi_0}\Delta\Phi = \Delta\tilde{\varphi}(a^\dagger + a), \quad (8.47)$$

with $\omega_r \equiv \omega_1, a^\dagger \equiv a_1^\dagger, a \equiv a_1, \delta \equiv \delta_1, \phi \equiv \phi_1, \Delta\bar{\varphi} = \Delta\bar{\varphi}_1$.

We choose charge densities as canonical momenta

$$Q_i = \frac{\partial \mathcal{L}_{tot}}{\partial \dot{\Phi}_i} \quad (i = 1, 2), \quad q = \frac{\partial \mathcal{L}_{tot}}{\partial \dot{\phi}} \quad (8.48)$$

and write in the matrix form as

$$\mathbf{Q} = \begin{pmatrix} Q_1 \\ Q_2 \\ q \end{pmatrix}, \quad \mathbf{\Phi} = \begin{pmatrix} \Phi_1 \\ \Phi_2 \\ \phi \end{pmatrix}, \quad \mathbf{C} = C_J \begin{pmatrix} 1 + \alpha + 2\alpha_4 & -(\alpha + 2\alpha_4) & -2\alpha_4\delta \\ -(\alpha + 2\alpha_4) & 1 + \alpha + 2\alpha_4 & 2\alpha_4\delta \\ -2\alpha_4\delta & 2\alpha_4\delta & 2\alpha_4\delta^2 + C_r/C_J \end{pmatrix}. \quad (8.49)$$

The Lagrangian of the total system can then be written in the vector form as

$$\mathcal{L}_{tot} = \frac{1}{2} \dot{\mathbf{\Phi}}^T \mathbf{C} \dot{\mathbf{\Phi}} - \frac{\tilde{C}_r}{2} \omega_r^2 \phi^2 - \mathcal{U}'_q. \quad (8.50)$$

The Hamiltonian \mathcal{H}_{tot} corresponding to the Lagrangian \mathcal{L}_{tot} , is obtained by a Legendre transformation

$$\begin{aligned} \mathcal{H}_{tot} &= \sum_{i=1,2} \frac{\partial \mathcal{L}_{tot}}{\partial \dot{\Phi}_i} \dot{\Phi}_i + \frac{\partial \mathcal{L}_{tot}}{\partial \dot{\phi}} \dot{\phi} - \mathcal{L}_{tot}, \\ &= \sum_{i=1,2} Q_i \dot{\Phi}_i + q \dot{\phi} - \mathcal{L}_{tot}, \\ &= \dot{\mathbf{\Phi}}^T \mathbf{Q} - \mathcal{L}_{tot} = \mathbf{Q}^T \mathbf{C} \mathbf{Q} - \mathcal{L}_{tot}, \\ &= \frac{1}{2} \mathbf{Q}^T \mathbf{C}^{-1} \mathbf{Q} + \frac{\tilde{C}_r}{2} \omega_r^2 \phi^2 + \mathcal{U}'_q. \end{aligned} \quad (8.51)$$

So that the total Hamiltonian reads

$$\mathcal{H}_{tot} = \frac{A}{2C_J} (Q_1^2 + Q_2^2) + \frac{B}{C_J} Q_1 Q_2 + \frac{C}{C_r} q \delta (Q_1 - Q_2) + \frac{D}{2C_r} q^2 + \frac{\tilde{C}_r}{2} \omega_r^2 \phi^2 + \mathcal{U}'_q, \quad (8.52)$$

with the geometrical parameters A, B, C, D being

$$A = \frac{\tilde{C}_r(1 + \alpha + 2\alpha_4) + 2\alpha_4 \delta^2 C_J(1 + \alpha)}{\tilde{C}_r(1 + 2\alpha + 4\alpha_4) + 2\alpha_4 \delta^2 C_J(1 + 2\alpha)}, \quad (8.53)$$

$$B = \frac{2\alpha\alpha_4 C_J \delta^2 + \tilde{C}_r(\alpha + 2\alpha_4)}{\tilde{C}_r(1 + 2\alpha + 4\alpha_4) + 2\alpha_4 \delta^2 C_J(1 + 2\alpha)}, \quad (8.54)$$

$$C = \frac{2\tilde{C}_r \alpha_4}{\tilde{C}_r(1 + 2\alpha + 4\alpha_4) + 2\alpha_4 \delta^2 C_J(1 + 2\alpha)}, \quad (8.55)$$

$$D = \frac{\tilde{C}_r(1 + 2(\alpha + 2\alpha_4))}{\tilde{C}_r(1 + 2\alpha + 4\alpha_4) + 2\alpha_4 \delta^2 C_J(1 + 2\alpha)}. \quad (8.56)$$

Expand Eq.(8.7) to the second order of $\Delta\varphi$, we have

$$\begin{aligned} \mathcal{U}'_q = & -E_J \left[\cos \varphi_1 + \cos \varphi_2 + \alpha \cos(\varphi_2 - \varphi_1 + 2\pi f_1) + 2\alpha_4(f_3) \cos(\varphi_2 - \varphi_1 + 2\pi \tilde{f}) \right] \\ & + E_J \alpha_4(f_3) \left[2\Delta\varphi \sin(\varphi_2 - \varphi_1 + 2\pi \tilde{f}) + (\Delta\varphi)^2 \cos(\varphi_2 - \varphi_1 + 2\pi \tilde{f}) \right], \end{aligned} \quad (8.57)$$

where the last term corresponds to the first-order and second-order qubit-resonator inductively coupling.

The degrees of freedom of the junction architecture are φ_j ($j = 1, 2$) and their conjugate momenta, which are the numbers n_j of Cooper pairs, which satisfy the commutation relation $[\varphi_j, n_{j'}] = i \delta_{j,j'}$. The total Hamiltonian can then be rewritten as

$$\mathcal{H}_{tot} = \mathcal{H}_q + \mathcal{H}_r + \mathcal{H}_{int}^c + \mathcal{H}_{int}^f. \quad (8.58)$$

The qubit Hamiltonian is

$$\begin{aligned} \mathcal{H}_q = & 4AE_c(n_1^2 + n_2^2) + 8BE_c n_1 n_2 - E_J [\cos \varphi_1 + \cos \varphi_2 + \alpha \cos(\varphi_2 - \varphi_1 + 2\pi f_1)] \\ & - E_J 2\alpha_4(f_3) \cos(\varphi_2 - \varphi_1 + 2\pi \tilde{f}), \end{aligned} \quad (8.59)$$

where we have used the charging energy $E_c = e^2/2C_J$ and $Q_i = 2e n_i$.

The resonator Hamiltonian is

$$\mathcal{H}_r = \frac{D}{2\tilde{C}_r} q^2 + \frac{\tilde{C}_r}{2} \omega_r^2 \phi^2. \quad (8.60)$$

The total interaction between the qubit and the resonator has two parts

$$\mathcal{H}_{int} = \mathcal{H}_{int}^c + \mathcal{H}_{int}^f, \quad (8.61)$$

with the qubit-resonator capacitive coupling Hamiltonian

$$\mathcal{H}_{int}^c = 2e \frac{C}{C_r} q \delta (n_1 - n_2), \quad (8.62)$$

and the qubit-resonator inductive coupling Hamiltonian

$$\mathcal{H}_{int}^f = E_J \alpha_4(f_3) \left[2\Delta\varphi \sin(\varphi_2 - \varphi_1 + 2\pi\tilde{f}) + (\Delta\varphi)^2 \cos(\varphi_2 - \varphi_1 + 2\pi\tilde{f}) \right]. \quad (8.63)$$

Projecting on the eigenstates $\{|k\rangle\}$ of frequencies $\{\Omega_k\}$ of the qubit Hamiltonian \mathcal{H}_q , the capacitive coupling \mathcal{H}_{int}^c reads

$$\mathcal{H}_{int}^c = \sum_{k,l} \hbar g_{c1}^{k,l} |k\rangle \langle l| (a^\dagger - a), \quad (8.64)$$

with the first-order capacitive-coupling strength being

$$g_{c1}^{k,l} = ieC\delta \sqrt{\frac{2\omega_r}{\hbar C_r}} \langle k| (n_1 - n_2) |l\rangle. \quad (8.65)$$

Similarly, the inductively coupling Hamiltonian \mathcal{H}_{int}^f can be expressed as

$$\mathcal{H}_{int}^f = \sum_{k,l} \hbar g_{f1}^{k,l} |k\rangle \langle l| (a^\dagger + a) + \sum_{k,l} \hbar g_{f2}^{k,l} |k\rangle \langle l| (a^\dagger + a)^2, \quad (8.66)$$

with the first- and second-order inductive-coupling strength being

$$\hbar g_{f1}^{k,l} = 2E_J \alpha_4(f_3) \Delta\bar{\varphi} \langle k| \sin(\varphi_2 - \varphi_1 + 2\pi\tilde{f}) |l\rangle, \quad (8.67)$$

$$\hbar g_{f2}^{k,l} = E_J \alpha_4(f_3) (\Delta\bar{\varphi})^2 \langle k| \cos(\varphi_2 - \varphi_1 + 2\pi\tilde{f}) |l\rangle. \quad (8.68)$$

Comparing $g_{f1}^{k,l}$ to $g_{c1}^{k,l}$ we get

$$\begin{aligned} \left| \frac{g_{f1}^{k,l}}{g_{c1}^{k,l}} \right| &= \frac{2\alpha_4(f_3)E_J}{\hbar\omega_r C} \left| \frac{\langle k | \sin(\varphi_2 - \varphi_1 + 2\pi\tilde{f}) | l \rangle}{\langle k | (n_1 - n_2) | l \rangle} \right|, \\ &> \frac{2\alpha_4(f_3)E_J}{\hbar\omega_r C} \left| \frac{\langle k | \sin(\varphi_2 - \varphi_1 + 2\pi\tilde{f}) | l \rangle}{\langle k | (n_1 - n_2) | l \rangle} \right|. \end{aligned} \quad (8.69)$$

Since in practice $E_J \gg \hbar\omega_r$ for flux qubit, the charge matrix elements are at best a fraction of unity in the vicinity of flux degeneracy point, we find $\left| g_{f1}^{k,l}/g_{c1}^{k,l} \right| \geq 10^2 - 10^3$. Unsurprisingly, charge coupling is negligible.

These matrix elements can be easily evaluated after diagonalizing qubit Hamiltonian H_q numerically to find the exact qubit eigenstates $\{|k\rangle\}$. Since the lowest two energy levels $(k, l) = (1, 2)$ are well separated from other higher energy levels, we can use them to construct the qubit and label them as the eigenstates of σ_z . Finally, after projecting the interaction terms into this truncated qubit basis, the full quantum Hamiltonian reads

$$\mathcal{H}_{tot} = \frac{\hbar\omega_q}{2} \sigma_z + \hbar\omega_r a^\dagger a + \mathcal{H}_{int}, \quad (8.70)$$

with the effective interaction Hamiltonian

$$\begin{aligned} \mathcal{H}_{int} &= 2E_J\alpha_4(f_3)\Delta\tilde{\varphi} \sum_{\mu=1}^3 c_\mu^1(\alpha, \alpha_4, f_1, f_2) \sigma_\mu (a^\dagger + a), \\ &+ E_J\alpha_4(f_3) (\Delta\tilde{\varphi})^2 \sum_{\mu=1}^3 c_\mu^2(\alpha, \alpha_4, f_1, f_2) \sigma_\mu (a^\dagger + a)^2. \end{aligned} \quad (8.71)$$

The pauli matrix for the two-level qubit is labeled as $\{\sigma_0, \sigma_1, \sigma_2, \sigma_3\} = \{I, \sigma_x, \sigma_y, \sigma_z\}$.

The normalized controllable magnitudes of the longitudinal and transverse coupling strengths $c_\mu^m(\alpha, \alpha_4, f_1, f_2)$ for m -th order interaction is given by

$$c_\mu^1 = \frac{\text{Tr}[\sigma_\mu \sin(\varphi_2 - \varphi_1 + 2\pi\tilde{f})]}{\sum_{k=0}^3 \text{Tr}[\sigma_k \sin(\varphi_2 - \varphi_1 + 2\pi\tilde{f})]}, \quad (8.72)$$

$$c_\mu^2 = \frac{\text{Tr}[\sigma_\mu \cos(\varphi_2 - \varphi_1 + 2\pi\tilde{f})]}{\sum_{k=0}^3 \text{Tr}[\sigma_k \cos(\varphi_2 - \varphi_1 + 2\pi\tilde{f})]}. \quad (8.73)$$

Note that we have ignored the capacitive coupling due to the fact that it is orders of magnitude

smaller than the inductively coupling.

8.3.2 Numerical analysis of the circuit

We provide *ab initio* numerical simulations to show the functionality of our circuit. Firstly, we numerically study the properties of the inhomogeneous transmission line resonator: the eigenfrequencies ω_n , the eigenmodes $u_n(x)$, and the phase slip $\Delta\bar{\varphi}_n$ [88]. Secondly, we perform the numerical study of the total Hamiltonian, and thus get the corresponding qubit frequency and coupling strengths to assist our ultrafast controlled phase gate scheme.

8.3.3 Characteristics of inhomogeneous transmission line resonator

Appropriate modeling of the inhomogeneous transmission-line electrical characteristics is needed to compute eigenmodes, frequencies and ultimately the coupling between the qubit and the resonator. In this part, we give details on the geometry of the inhomogeneous resonators that will be used for numerical simulations [88]. The capacitance per unit length C_0 , the inductance per unit length L_0 and the impedance Z_0 of the coplanar transmission-line resonator depend on the ratio between the width of the center electrode S and the distance between the two ground planes $S + 2W$, with W being the distance between the ground plane and the edge of the central line [160, 161]:

$$C_0 = 2\epsilon_0(\epsilon_r + 1) \frac{K(k_0)}{K(k'_0)}, \quad (8.74)$$

$$L_0^{geo} = \frac{\mu_0}{4} \frac{K(k'_0)}{K(k_0)}, \quad L_0 = L_0^{geo} + L_0^{kin} \quad (8.75)$$

$$Z_0 = \sqrt{\frac{L_0}{C_0}}, \quad (8.76)$$



Figure 8.5: Geometry of the inhomogeneous transmission line used in numerical simulations, with central-line width S and ground-plane spacing W for the total length of the line 2ℓ .

where ϵ_r is the dielectric constant of the substrate, and $K(x)$ is the complete elliptic integral of the first kind with the arguments

$$k_0 = \frac{S}{S + 2W}, \quad (8.77)$$

$$k'_0 = \sqrt{1 - k_0^2}. \quad (8.78)$$

By decreasing the aspect ratio k_0 along the line, the inductance and impedance of the line are locally increased while the capacitance is decreased.

For a superconducting resonators, the kinetic inductance can be expressed as [162]

$$L_0^{kin} = \mu_0 \lambda_L(T) \frac{C}{4A'D'K(k_0)} \left[\frac{1.7}{\sinh(t/2\lambda_L(T))} + \frac{0.4}{\sqrt{[(B'/A')^2 - 1][1 - (B'/D')^2]}} \right], \quad (8.79)$$

where $\lambda_L(T)$ is the London penetration depth of the superconductor at temperature T , t is the thickness, and

$$A' = -\frac{t}{\pi} + \frac{1}{2} \sqrt{\left(\frac{2t}{\pi}\right)^2 + S^2}, \quad B' = \frac{S^2}{4A'}, \quad (8.80)$$

$$C' = B' - \frac{t}{\pi} + \sqrt{\left(\frac{t}{\pi}\right)^2 + W^2}, \quad D' = \frac{2t}{\pi} + C'. \quad (8.81)$$

As for the geometrical inductance, a decrease of the aspect ratio will increase the kinetic inductance of the line but the effect is rather marginal unless the dimensions of the cross section of the central electrode become of the order of λ_L .

We consider a regular, initially homogeneous transmission line resonator made of Aluminum ($\epsilon_r = 11$) with a total length of $2\ell = 5$ mm. The central electrode is $t = 200$ nm thick and $S = 5$ μm wide. The ground planes are $W = 2.5$ μm away from the edge of the central-line. This gives the aspect ratios $k_0 = 0.5$ and $k'_0 = 0.866$, which give $K(k_0) = 1.8541$, $K(k'_0) = 2.4413$ and thus we have

$$L_0^{geo} = 4.1367 \times 10^{-7} \frac{\text{H}}{\text{m}}, \quad L_0^{kic} = 1.5373 \times 10^{-9} \frac{\text{H}}{\text{m}}, \quad (8.82)$$

$$L_0 = 4.152 \times 10^{-7} \frac{\text{H}}{\text{m}}, \quad L_r = 2\ell L_0 = 2.076 \text{ nH}, \quad (8.83)$$

$$C_0 = 161.38 \frac{\text{pF}}{\text{m}}, \quad C_r \sim 807 \text{ fF}, \quad (8.84)$$

$$Z_0 = 50.72\Omega. \quad (8.85)$$

The corresponding phase velocity for electromagnetic waves propagating along this transmission line resonator is

$$v_p = \frac{1}{\sqrt{L_0 C_0}} = 1.22 \times 10^8 \text{ m s}^{-1}. \quad (8.86)$$

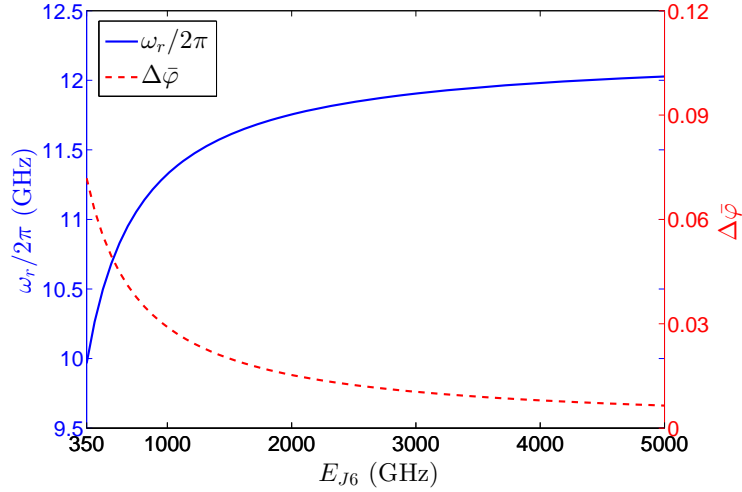


Figure 8.6: The resonator frequency ω_r and the magnitude of phase slip $\Delta\bar{\varphi}$ as a function of the sixth Josephson energy E_{J6} .

As seen from Fig.(8.6), the presence of the sixth Josephson junction can locally change the inductance and thus modifies the resonator frequency as well as increase the phase slip, which gives rise to much stronger coupling.

8.3.4 Numerical simulation of the total Hamiltonian

For junctions with Josephson energy $E_J/h = 221$ GHz, the simulation shows that when external fluxes satisfies $f_2 + f_3/2 = 0.5$, both c_y^1 and the second-order coupling are negligible. This reduces the interaction Hamiltonian to

$$\mathcal{H}_{int} = \hbar\bar{g}(a + a^\dagger)(c_z\sigma_z + c_x\sigma_x), \quad (8.87)$$

with $\bar{g} = 2E_J\alpha_4(f_3)\Delta\bar{\varphi}/\hbar$ and the effective coupling strength $g_{z,x} = c_{z,x}\bar{g}$, $c_{z,x} \equiv c_{x,z}^1$. The normalized coupling constant with respect to the resonator frequency \bar{g}/ω_r is shown in Fig.(8.7).

The coupling coefficients c_z and c_x as a function of the qubit junction size α and the frustration

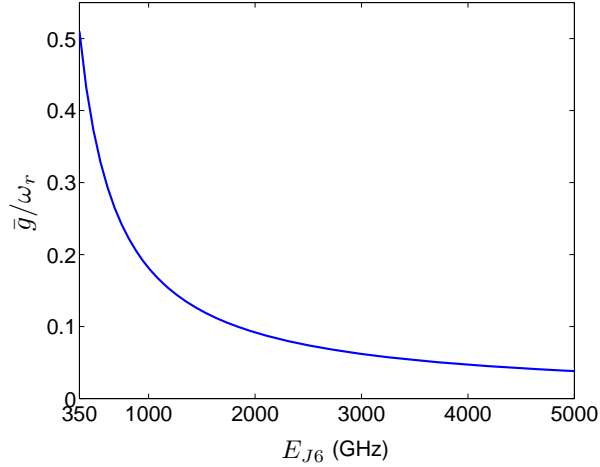


Figure 8.7: The ratio between the coupling constant and the resonator frequency \bar{g}/ω_r , as a function of the sixth Josephson energy E_{J_6} .

parameter f_1 are shown in Fig.(8.8). These two figures show clearly another characteristic of the setup, that is, the switching from transversal to longitudinal couplings depending on the external flux Φ_1 [142]. In particular, when selecting a qubit junction size $\alpha = 1.3$ and $f_1 = 0.505$, we have a large (small) contribution of longitudinal (transversal) coupling — see Fig.(8.9(a)) where we plot c_z and c_x for a parameter $f_3 = \{1, 0.5, 0\}$.

From the diagonalization of qubit Hamiltonian for different values of the frustration parameter $f_3 = \{1, 0.5, 0\}$, we estimate a qubit frequency $\omega_q/2\pi \sim \{11.5, 11.2, 10.5\}$ GHz, as seen in Fig.(8.9(b)). Furthermore, considering a junction size $\alpha_4 = 0.16$ we estimate a qubit-resonator coupling constant as $\bar{g}/\omega_r = \{0.513, 0, -0.513\}$ that goes into the USC regime of light-matter interaction [88] as well as very small transversal coupling coefficients $c_x = \{0.17, 0.095, 0.035\}$. It is noteworthy to mention that our setup allows us turning on and off the coupling $g_{z,x}$ as well as to change the sign of it, operations that may be carried out in times about 0.1 ns [142].

The tunability of parameters involved could also increase the ratio \bar{g}/ω_r , without affecting the characteristics of the setup. For instance, for the sixth Josephson junction with capacitance $C_{J_6} \sim 17.8$ fF, and inductance $L_{J_6} \sim 0.47$ nH, we estimate the first mode of the resonator with frequency $\omega_r/2\pi \sim 9.96$ GHz and a phase slip magnitude $\Delta\bar{\varphi} = 0.072$. This leads to a qubit-resonator coupling strength constant of $\bar{g}/\omega_r = 0.513$. Moreover, the ratio of the transversal to longitudinal coupling can be tuned with other choices of parameters.

These examples and particularly the model introduced by Eq.(8.87), will be the support to

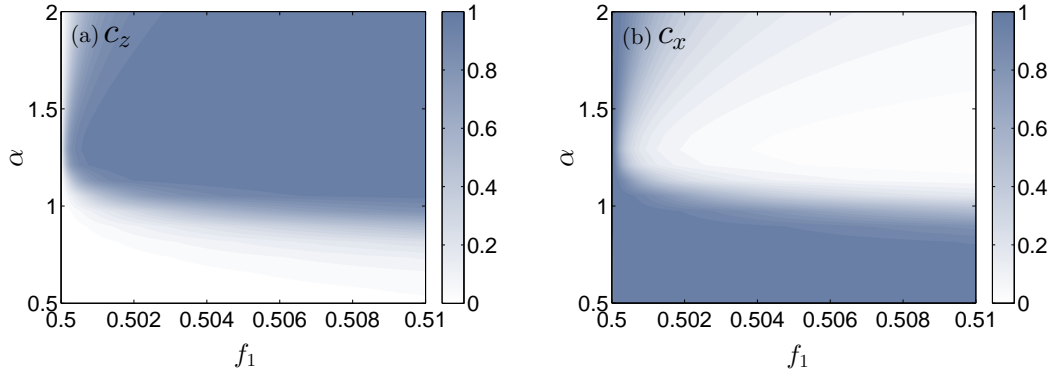


Figure 8.8: Couplings strength coefficients c_z (a) and c_x (b) as a function of the qubit junction size $\alpha = E_{J3}/E_J$, and the external frustration parameter f_1 with $f_3 = 0$. In this simulation we use the parameters $E_J/h = 221$ GHz, $E_J/E_c = 32$, $E_{J6}/h = 348$ GHz and $\alpha_4 = 0.16$.

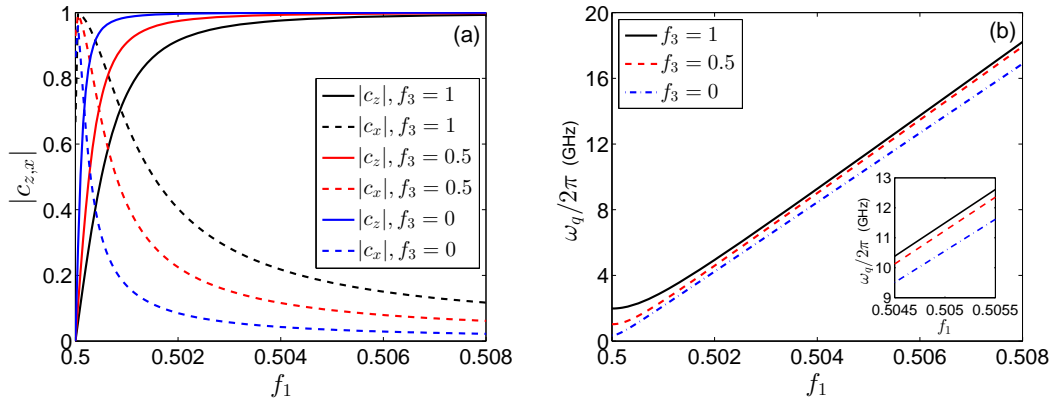


Figure 8.9: Couplings strength coefficients $c_{z,x}$ (a) and qubit spectrum ω_q (b) for different frustration parameters $f_3 = \{1, 0.5, 0\}$ with junction size $\alpha = 1.3$.

develop protocols for two-qubit gates in the USC regime of light-matter interaction.

8.4 The ultrafast two-qubit gate scheme

The external tunability of the previous circuit is now exploited to propose an ultrafast two-qubit gate protocol [153, 154] by putting two designed flux qubits into the inhomogeneous transmission line resonator as shown in Fig.(8.10).

An interesting example of such a gate in circuit QED system was introduced in Ref. [163]: a two-qubit controlled phase gate is produced by alternating between positive and negative values of the coupling strength g_x for each qubit. In our architecture, this can be done simply by

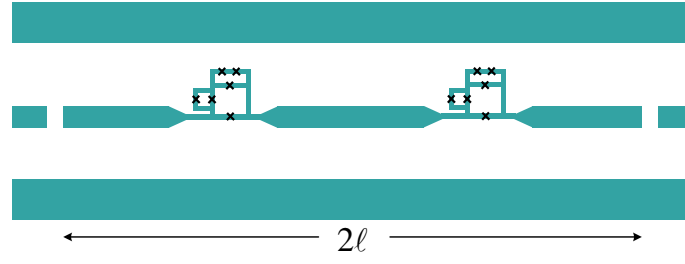


Figure 8.10: Schematics of ultrastrongly-coupled flux qubits in the circuit QED design for the ultrafast two-qubit gate.

changing the flux f_3 from 0 to 1; however, this action will also affect the value of the undesired transversal coupling in Hamiltonian Eq. (8.87). For instance, in case of a junction size $\alpha_4 = 0.16$, we find $g/\omega_r = \{0.513, -0.513\}$ and $c_x = \{0.035, 0.17\}$ for $f_3 = \{0, 1\}$. This noticeable mismatch in the values of the coefficient c_x makes the scheme in Ref. [163] less attractive for the circuit designed above.

Hence, a more suitable protocol for our architecture, based on a four-step sequential displacement operations of the intracavity field consists of the following:

Step 1 — The coupling g_{z1} is maximized ($f_3^{(1)} = 0$), whereas g_{z2} made exactly zero by tuning $f_3^{(2)} = 0.5$. The system evolves for a period $\omega_r t_1 \in (0, \pi/2]$.

Step 2 — The coupling g_{z2} is maximized ($f_3^{(2)} = 0$), whereas g_{z1} made exactly zero by tuning $f_3^{(1)} = 0.5$. The system evolves for a period $\omega_r t_2 = \pi - \omega_r t_1$.

Step 3 — Repeat Step 1.

Step 4 — Repeat Step 2.

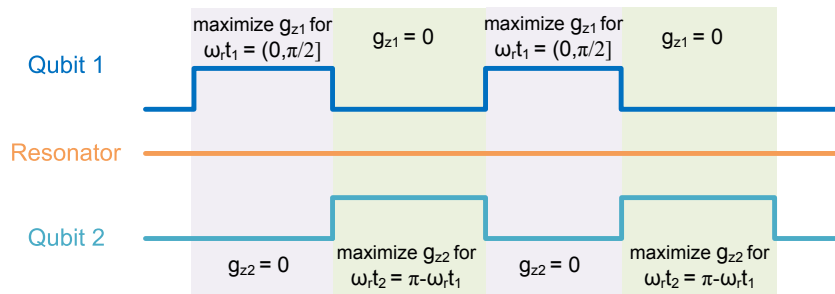


Figure 8.11: The ultrafast two-qubit gate scheme as a sequence of displacement operations.

We study first the ideal case, in which the transversal component of the coupling in Eq.(8.87) is negligible, which could be achieved by tuning the fluxes $f_1 = 0.505$ of each qubit. Then, the

two-qubit Hamiltonian is

$$\mathcal{H} = \frac{1}{2} \sum_{i=1,2} \hbar \omega_{q_i} \sigma_z^{(i)} + \hbar \omega_r a^\dagger a - \sum_{i=1,2} \hbar g_{zi} (a + a^\dagger) \sigma_z^i. \quad (8.88)$$

Under this Hamiltonian, the unitary evolution operator U_i corresponding to each step is

$$\begin{aligned} U_{1,3} &= e^{-i\mathcal{H}_{1,3}t_1}, \\ &= e^{-i\frac{\omega_{q_{1\uparrow}}\sigma_{z1} + \omega_{q_{2\downarrow}}\sigma_{z2}}{2}t_1} \mathcal{D}\left(\frac{g_{z1}}{\omega_r}\sigma_{z1}\right) e^{-i\omega_r t_1 a^\dagger a} \mathcal{D}\left(-\frac{g_{z1}}{\omega_r}\sigma_{z1}\right), \\ &= e^{-i\frac{\omega_{q_{1\uparrow}}\sigma_{z1} + \omega_{q_{2\downarrow}}\sigma_{z2}}{2}t_1} e^{-i\omega_r t_1 a^\dagger a} \mathcal{D}\left(\frac{g_{z1}}{\omega_r}(e^{i\omega_r t_1} - 1)\sigma_{z1}\right), \end{aligned} \quad (8.89)$$

up to a constant phase, with $\omega_{q_{i\uparrow}}$, $\omega_{q_{i\downarrow}}$ stands for the value of the qubit frequency when g_{zi} is maximum, zero, respectively. The controlled coherent displacement of the field is

$$\mathcal{D}(\beta\sigma_z) = \exp(\{\beta a^\dagger - \beta^* a\}\sigma_z), \quad (8.90)$$

and we have used the property that

$$\mathcal{D}(\beta)\mathcal{D}(\gamma) = e^{i\text{Im}(\beta\gamma^*)} \mathcal{D}(\beta + \gamma), \quad (8.91)$$

$$e^{-i\theta a^\dagger a} \mathcal{D}(\beta) e^{i\theta a^\dagger a} = \mathcal{D}(\beta e^{-i\theta}), \quad (8.92)$$

$$\mathcal{D}^{-1}(\beta\sigma_z) a^\pm \mathcal{D}(\beta\sigma_z) = a^\pm + \beta\sigma_z, \quad (8.93)$$

$$\mathcal{D}^{-1}(\beta\sigma_z) e^{-i\omega t_1 a^\dagger a} \mathcal{D}(\beta\sigma_z) = e^{-i\omega t_1 (a^\dagger + \beta\sigma_z)(a + \beta\sigma_z)}. \quad (8.94)$$

Similarly, the evolution operator $U_{2,4}$ reads

$$U_{2,4} = e^{-i\frac{\omega_{q_{1\downarrow}}\sigma_{z1} + \omega_{q_{2\uparrow}}\sigma_{z2}}{2}t_2} e^{-i\omega_r t_2 a^\dagger a} \mathcal{D}\left(\frac{g_{z2}}{\omega_r}(e^{i\omega_r t_2} - 1)\sigma_{z2}\right). \quad (8.95)$$

The total evolution operator can then be written as

$$U_{gate} = \prod_{i=1}^4 U_i = e^{-i(\omega_{q_{1\uparrow}}t_1 + \omega_{q_{1\downarrow}}t_2)\sigma_{z1}} e^{-i(\omega_{q_{2\downarrow}}t_1 + \omega_{q_{2\uparrow}}t_2)\sigma_{z2}} e^{4i \sin \omega_r t_1 \frac{g_{z1} g_{z2}}{\omega_r^2} \sigma_{z1} \sigma_{z2}}. \quad (8.96)$$

This gate U_{gate} is equivalent to a controlled phase gate [1] up to local unitary operations, provided

that

$$4 \sin \omega_r t_1 \frac{g_{z1} g_{z2}}{\omega_r^2} = \frac{\pi}{4}, \quad (8.97)$$

which requires g_{zi}/ω_r to be in the ultrastrong regime for this gate proposal.

In the case of junction size $\alpha_4^{(1,2)} = 0.16$, for which the coupling strength takes a value of $g_{z1}/\omega_r = g_{z2}/\omega_r = 0.513$ and resonator frequency of $\omega_r/2\pi \sim 9.96$ GHz, and thus the total gate time will be

$$t_{gate} = 2\pi/\omega_r \sim 0.11\text{ns}. \quad (8.98)$$

Therefore, this protocol may lead to a significant improvement in the operating time scale of circuit QED, as well as microwave cavity QED and optical systems.

8.5 Discussion

Given the controlled phase gate we proposed based on the tunable qubit-resonator coupling in USC, we may consider the following extensions. (i) Multi-qubit entanglement and gate operations, such as realization of a faster three-qubit Toffoli gate in USC regime than the other schemes works in strong coupling regime [83,84]; (ii) With the advantage of switchable coupling in both strength and orientation, we may think of the generation of Ising-type Hamiltonian for qubit arrays; (iii) By controlling the geometry-related flux values, we can increase the higher-order couplings and thus study the non-linear dynamics in USC regime; (iv) The adjustable coupling also allows us to couple to slower measurement devices.

Deviations from perfect fidelity are expected if one accounts for undesired transverse coupling in Eq.(8.87). For an initial state where both qubits are in state $|+\rangle = (|g\rangle + |e\rangle)/\sqrt{2}$ and the resonator is in the vacuum state, we can compute the fidelity of the state generated assuming that $c_x^{(i)} = 0.035$ for each qubit at $f_3^{(i)} = 0$. The fidelity of this state, with reduced density matrix ρ , as compared to the ideal $|\psi\rangle\langle\psi|$, for which transverse coupling is neglected, amounts to $\mathcal{F} = \langle\psi|\rho|\psi\rangle \geq 0.996$. This result is unchanged even if we include up to the third cavity mode in our *ab initio* calculation. For the sake of simplicity, we have considered instantaneous changes in the value of the fluxes f_3 . In this sense, the scheme can be easily adapted to account for smooth time-dependent profiles in the value of the coupling strength of both qubits, provided the adequate interaction time and number of iterations, and that no overlap between the pulses occurs.

Indeed, switching frequencies of about 10–80 GHz are already available [86]. This should allow the experimental realization of a high-fidelity fast CPHASE gate with sub-nanosecond operation time.

Conclusion

As the two parts of the thesis work are the atom-pulses interaction and the quantum gate operations in circuit QED, our results are also summarized into this two categories.

In Part I, firstly we introduced the general quantized model of atom-pulses interaction in the propagating modes using time-dependent Heisenberg-Langevin equations.

Secondly, with the help of the developed formalism we study the dependence of atomic excitation probability on the following properties of the pulses as:

- The spatial overlap between the pulse and the dipole pattern of the atomic emission.
- The temporal and the spectral distributions of the pulses.
- The quantum state of the pulse field.

The spatial overlap parameter $\Lambda \in [0, 8\pi/3]$ is obtained by weighting the pulse spatial mode function and the polarization distribution with the the atomic dipole pattern. We provide detailed solutions for both single-photon Fock state and coherent states pulses with various temporal shapes. We give the optimal bandwidth and the corresponding maximal excitation probability for different single photon Fock state as well as coherent state pulses.

Thirdly, we have theoretically investigated the atomic dynamics due to the interaction with two spatial-mode multi-photon propagating pulses in the one-dimensional geometry. We have shown the following properties:

- *Single-photon excitation:* the atomic excitation probability is upper bounded by 0.5, when the atom is excited by a single-photon from a single spatial-mode. Full atomic excitation

by single-photon is possible only with a rising-exponentially shaped Fock state pulse in the even-parity mode — a balanced superposition of the right and left spatial-modes.

- *Multi-photon excitation:* for coherent state pulse, the maximum excitation probability P_{max} is ordered by average photon number \bar{n} in the even-mode for all bandwidths at few photon level. Higher power always gives higher atomic excitation before saturation. On the other hand, for Fock state pulses with intermediate bandwidths $\Omega \sim \gamma_0$, P_{max} is not ordered by photon number n .
- *Two spatial-mode pulses interference:* in general, there is no first-order interference between two Fock state pulses. On the other hand, for two coherent state pulses, the atomic dynamics can be well controlled by the relative phase ϕ between the two pulses and by the average photon number in both pulses.

These results are relevant for applications in integrated quantum optical devices, such as quantum switch for light [120, 164]. In addition, the presented formalism can be used to further study the atom and propagating light pulses dynamics in one dimensional frequency-continuum. It can also be generalized to 3D cases when accounting for the details of the spatial mode-matching.

Fourthly, we compare the theory to the experiment where a single trapped ⁸⁷Rb atom interacts with optical pulses temporally engineered in rising exponential and rectangular shapes. We showed that the atomic excited state population is sensitive to the envelope of the excitation pulses. The rising exponential pulse yields higher excitation probability than the rectangular pulses with smaller average photon number and the same bandwidth. Rabi oscillations of a single atom are observed with about 1000 photons in a pulse. However, the spatial overlap between the pulse mode and the atomic emission mode should be significantly enhanced to observe interaction between two light pulses at few photon level. The possibility of using Fock states instead of weak coherent pulses is also advantageous, since all the effects observed in this thesis should be more profound.

Fifthly, we showed by a fully quantized calculation that a single-photon Fock state pulse with various temporal shapes can be efficiently stored and retrieved from a quantum memory device consisting of a single two-level atom in a half cavity. The principle is that the time-dependent atomic decay rate can be dynamically tuned between zero and the maximum $2\gamma_0$ by changing

the distance between the atom and the mirror. The cutoff frequency of the system, given by the double of the free space decay rate of the atom, imposes the limits on the input photon bandwidth for which the photon can be efficiently stored. We analyzed the dependence of the storage efficiency as a function of the photon bandwidth. We also gave possible implementations of the proposed quantum memory scheme, such as single atoms or ions in a half cavity or a superconducting qubit coupled to a 1D transmission line terminated by a SQUID.

In Part II, we firstly present the quantized electrical circuits.

Secondly, we introduce the general atom-photon interaction model in cavity/circuit QED, and discuss the dynamics within and beyond rotating wave approximation for different coupling regimes.

Thirdly, we analyse numerically the performance of two quantum controlled phase gate schemes in the crossover from the strong to the ultrastrong coupling regime while taking into account the effects of counter-rotating terms appearing in the Hamiltonian. These schemes are designed to work ideally in the normal strong coupling regime. Our numerical results show that the gate fidelity is reducing fast with the increasing normalized coupling strength g/ω_r .

Finally, we propose a new two-qubit quantum controlled-phase gate scheme that works in the ultrastrong coupling regime. Our scheme includes a tunable ultrastrongly coupled qubit-resonator architecture as well as a two-qubit controlled phase gate protocol that works in this ultrastrong coupling regime. In our system, the versatile flux qubits are galvanically coupled to the constricted center conductor line of a transmission line resonator which is interrupted by a small Josephson junction. Our two-qubit gate proposal is based on a four-step sequential displacement of the intracavity field, and operates at a time proportional to the inverse of the resonator frequency. Our controlled-phase quantum gate scheme may work at subnanosecond time scales with fidelity $F \approx 0.996$ considering the state-of-the-art circuit QED technology. Our scheme may lead to a significant improvement in the operating time with respect to the standard circuit QED scenarios, as well as microwave or optical cavity QED systems, together with the reduction of the large resource requirement for fault-tolerant quantum computing.

Bibliography

- [1] M. A. Nielsen and I. L. Chuang. *Quantum Computation and Quantum Information: 10th Anniversary Edition*. Cambridge University Press, 2011.
- [2] V. Scarani, H. Bechmann-Pasquinucci, N. J. Cerf, M. Dušek, N. Lütkenhaus, and M. Peev. The security of practical quantum key distribution. *Reviews of Modern Physics*, 81(3):1301–1350, 2009.
- [3] H. J. Kimble. The quantum internet. *Nature*, 453(7198):1023–1030, 2008.
- [4] R. Feynman. Simulating physics with computers. *International Journal of Theoretical Physics*, 21(6):467–488, 1982.
- [5] D. Deutsch. Quantum theory, the church-turing principle and the universal quantum computer. *Proceedings of the Royal Society of London. A. Mathematical and Physical Sciences*, 400(1818):97–117, 1985.
- [6] D. Deutsch and R. Jozsa. Rapid solution of problems by quantum computation. *Proceedings of the Royal Society of London. Series A: Mathematical and Physical Sciences*, 439(1907):553–558, 1992.
- [7] P. W. Shor. Polynomial-time algorithms for prime factorization and discrete logarithms on a quantum computer. *SIAM J. Comput.*, 26(5):1484–1509, 1997.

- [8] L. K. Grover. A fast quantum mechanical algorithm for database search. In *Proceedings of the twenty-eighth annual ACM symposium on Theory of computing*, STOC '96, pages 212–219, New York, USA, 1996. ACM.
- [9] D. Gottesman. An introduction to quantum error correction and fault-tolerant quantum computation. *arXiv:0904.2557*, 2009.
- [10] A. G. Fowler, D. S. Wang, C. D. Hill, T. D. Ladd, R. Van Meter, and L. C. L. Hollenberg. Surface code quantum communication. *Physical Review Letters*, 104(18):180503, 2010.
- [11] C. H. Bennett and G. Brassard. Quantum cryptography: Public key distribution and coin tossing. In *Proceedings of the IEEE International Conference on Computers, Systems and Signal Processing*, pages 175–179, Bangalore, India, 1984. IEEE.
- [12] A. K. Ekert. Quantum cryptography based on bells theorem. *Physical Review Letters*, 67(6):661–663, 1991.
- [13] C.-Z. Peng, J. Zhang, D. Yang, W.-B. Gao, H.-X. Ma, H. Yin, H.-P. Zeng, T. Yang, X.-B. Wang, and J.-W. Pan. Experimental long-distance decoy-state quantum key distribution based on polarization encoding. *Physical Review Letters*, 98(1):010505, 2007.
- [14] T. Schmitt-Manderbach, H. Weier, M. Fürst, R. Ursin, F. Tiefenbacher, T. Scheidl, J. Perdigues, Z. Sodnik, C. Kurtsiefer, J. G. Rarity, A. Zeilinger, and H. Weinfurter. Experimental demonstration of free-space decoy-state quantum key distribution over 144 km. *Physical Review Letters*, 98(1):010504, 2007.
- [15] D. Stucki, N. Walenta, F. Vannel, R. T. Thew, N. Gisin, H. Zbinden, S. Gray, C. R. Towery, and S. Ten. High rate, long-distance quantum key distribution over 250 km of ultra low loss fibres. *New Journal of Physics*, 11(7):075003, July 2009.
- [16] R. Ursin, F. Tiefenbacher, T. Schmitt-Manderbach, H. Weier, T. Scheidl, M. Lindenthal, B. Blauensteiner, T. Jennewein, J. Perdigues, P. Trojek, B. Ömer, M. Fürst, M. Meyenburg, J. Rarity, Z. Sodnik, C. Barbieri, H. Weinfurter, and A. Zeilinger. Entanglement-based quantum communication over 144km. *Nature Physics*, 3(7):481–486, 2007.

- [17] J. I. Cirac, P. Zoller, H. J. Kimble, and H. Mabuchi. Quantum state transfer and entanglement distribution among distant nodes in a quantum network. *Physical Review Letters*, 78(16):3221–3224, 1997.
- [18] L.-M. Duan, M. D. Lukin, J. I. Cirac, and P. Zoller. Long-distance quantum communication with atomic ensembles and linear optics. *Nature*, 414(6862):413–418, 2001.
- [19] W. K. Wootters and W. H. Zurek. A single quantum cannot be cloned. *Nature*, 299(5886):802–803, 1982.
- [20] H.-J. Briegel, W. Dür, J. I. Cirac, and P. Zoller. Quantum repeaters: The role of imperfect local operations in quantum communication. *Physical Review Letters*, 81(26):5932–5935, 1998.
- [21] N. Sangouard, C. Simon, H. de Riedmatten, and N. Gisin. Quantum repeaters based on atomic ensembles and linear optics. *Reviews of Modern Physics*, 83(1):33–80, 2011.
- [22] L.-M. Duan and H. J. Kimble. Efficient engineering of multiatom entanglement through single-photon detections. *Physical Review Letters*, 90(25):253601, 2003.
- [23] B. Zhao, Z. B. Chen, Y. A. Chen, J. Schmiedmayer, and J.-W. Pan. Robust creation of entanglement between remote memory qubits. *Physical Review Letters*, 98(24):240502, 2007.
- [24] Z. B. Chen, B. Zhao, Y. A. Chen, J. Schmiedmayer, and J.-W. Pan. Fault-tolerant quantum repeater with atomic ensembles and linear optics. *Physical Review A*, 76(2):022329, August 2007.
- [25] N. Sangouard, C. Simon, B. Zhao, Y. A. Chen, H. de Riedmatten, J.-W. Pan, and N. Gisin. Robust and efficient quantum repeaters with atomic ensembles and linear optics. *Physical Review A*, 77(6):062301, 2008.
- [26] K. Hammerer, A. S. Sørensen, and E. S. Polzik. Quantum interface between light and atomic ensembles. *Reviews of Modern Physics*, 82(2):1041–1093, 2010.

- [27] A. Kuzmich, W. P. Bowen, A. D. Boozer, A. Boca, C. W. Chou, L.-M. Duan, and H. J. Kimble. Generation of nonclassical photon pairs for scalable quantum communication with atomic ensembles. *Nature*, 423(6941):731–734, 2003.
- [28] D. N. Matsukevich and A. Kuzmich. Quantum state transfer between matter and light. *Science*, 306(5696):663–666, 2004.
- [29] C. W. Chou, J. Laurat, H. Deng, K. S. Choi, H. de Riedmatten, D. Felinto, and H. J. Kimble. Functional quantum nodes for entanglement distribution over scalable quantum networks. *Science*, 316(5829):1316–1320, 2007.
- [30] H. P. Specht, C. Nölleke, A. Reiserer, M. Uphoff, E. Figueroa, S. Ritter, and G. Rempe. A single-atom quantum memory. *Nature*, 473(7346):190–193, 2011.
- [31] S. Ritter, C. Nölleke, C. Hahn, A. Reiserer, A. and Neuzner, M. Uphoff, M. Mücke, E. Figueroa, J. Bochmann, and G. Rempe. An elementary quantum network of single atoms in optical cavities. *Nature*, 484(7393):195–200, 2012.
- [32] W. J. Munro, A. M. Stephens, S. J. Devitt, K. A. Harrison, and Kae Nemoto. Quantum communication without the necessity of quantum memories. *Nature Photonics*, 6(11):777–781, 2012.
- [33] D. P. DiVincenzo. The physical implementation of quantum computation. *Fortschritte der Physik*, 48(9-11):771783, 2000.
- [34] P. Kok, W. J. Munro, K. Nemoto, T. C. Ralph, J.P. Dowling, and G. J. Milburn. Linear optical quantum computing with photonic qubits. *Reviews of Modern Physics*, 79(1):135–174, 2007.
- [35] J.-W. Pan, Z.-B. Chen, C.-Y. Lu, H. Weinfurter, A. Zeilinger, and M. Żukowski. Multiphoton entanglement and interferometry. *Reviews of Modern Physics*, 84(2):777–838, 2012.
- [36] J. I. Cirac and P. Zoller. Quantum computations with cold trapped ions. *Physical Review Letters*, 74(20):4091–4094, 1995.

- [37] R. Blatt and D. Wineland. Entangled states of trapped atomic ions. *Nature*, 453(7198):1008–1015, 2008.
- [38] I. Bloch. Quantum coherence and entanglement with ultracold atoms in optical lattices. *Nature*, 453(7198):1016–1022, 2008.
- [39] K.-A. B. Soderberg, N. Gemelke, and C. Chin. Ultracold molecules: vehicles to scalable quantum information processing. *New Journal of Physics*, 11(5):055022, 2009.
- [40] M. H. Devoret, A. Wallraff, and J. M. Martinis. Superconducting qubits: A short review. *arXiv:cond-mat/0411174*, 2004.
- [41] J. Clarke and F. K. Wilhelm. Superconducting quantum bits. *Nature*, 453(7198):1031–1042, 2008.
- [42] P. Neumann, N. Mizuochi, F. Rempp, P. Hemmer, H. Watanabe, S. Yamasaki, V. Jacques, T. Gaebel, F. Jelezko, and J. Wrachtrup. Multipartite entanglement among single spins in diamond. *Science*, 320(5881):1326–1329, 2008.
- [43] D. Loss and D. P. DiVincenzo. Quantum computation with quantum dots. *Physical Review A*, 57(1):120–126, 1998.
- [44] N. P. de Leon, M. D. Lukin, and H. Park. Quantum plasmonic circuits. *IEEE Journal of Selected Topics in Quantum Electronics*, 18(6):1781–1791, 2012.
- [45] A. Morello, J. J. Pla, F. A. Zwanenburg, K. W. Chan, K. Y. Tan, H. Huebl, M. Möttönen, C. D. Nugroho, C. Yang, J. A. van Donkelaar, A. D. C. Alves, D. N. Jamieson, C. C. Escott, L. C. L. Hollenberg, R. G. Clark, and A. S. Dzurak. Single-shot readout of an electron spin in silicon. *Nature*, 467(7316):687–691, 2010.
- [46] S. Simmons, R. M. Brown, H. Riemann, N. V. Abrosimov, P. Becker, H.-J. Pohl, M. L. W. Thewalt, K. M. Itoh, and J. J. L. Morton. Entanglement in a solid-state spin ensemble. *Nature*, 470(7332):69–72, 2011.
- [47] J. J. Pla, K. Y. Tan, J. P. Dehollain, W. H. Lim, J. J. L. Morton, D. N. Jamieson, A. S. Dzurak, and A. Morello. A single-atom electron spin qubit in silicon. *Nature*, 489(7417):541–545, 2012.

- [48] M. Wallquist, K. Hammerer, P. Rabl, M. Lukin, and P. Zoller. Hybrid quantum devices and quantum engineering. *Physica Scripta*, T137:014001, 2009.
- [49] P. Rabl, S. J. Kolkowitz, F. H. L. Koppens, J. G. E. Harris, P. Zoller, and M. D. Lukin. A quantum spin transducer based on nanoelectromechanical resonator arrays. *Nature Physics*, 6(8):602–608, 2010.
- [50] O. Arcizet, V. Jacques, A. Siria, P. Poncharal, P. Vincent, and S. Seidelin. A single nitrogen-vacancy defect coupled to a nanomechanical oscillator. *Nature Physics*, 7(11):879–883, 2011.
- [51] G. Zumofen, N. M. Mojarad, V. Sandoghdar, and M. Agio. Perfect reflection of light by an oscillating dipole. *Physical Review Letters*, 101(18):180404, 2008.
- [52] G. Wrigge, I. Gerhardt, J. Hwang, G. Zumofen, and V. Sandoghdar. Efficient coupling of photons to a single molecule and the observation of its resonance fluorescence. *Nature Physics*, 4(1):60–66, 2008.
- [53] S. Heugel, A. Villar, M. Sondermann, U. Peschel, and G. Leuchs. On the analogy between a single atom and an optical resonator. *Laser Physics*, 20(1):100–106, 2010.
- [54] D. Pinotsi and A. Imamoglu. Single photon absorption by a single quantum emitter. *Physical Review Letters*, 100(9):093603, 2008.
- [55] M. Stobinska, G. Alber, and G. Leuchs. Perfect excitation of a matter qubit by a single photon in free space. *Europhysics Letters*, 86(1):14007, 2009.
- [56] Y. M. Wang, J. Minář, L. Sheridan, and V. Scarani. Efficient excitation of a two-level atom by a single photon in a propagating mode. *Physical Review A*, 83(6):063842, 2011.
- [57] S. Haroche and D. Kleppner. Cavity quantum electrodynamics. *Physics Today*, 42(1):24–30, 1989.
- [58] S Haroche and J. M. Raimond. *Exploring the Quantum: Atoms, Cavities, and Photons*. Oxford University Press, USA, 2006.

- [59] A. D. Boozer, A. Boca, R. Miller, T. E. Northup, and H. J. Kimble. Reversible state transfer between light and a single trapped atom. *Physical Review Letters*, 98(19):193601, 2007.
- [60] M. K. Tey, Z. Chen, S. A. Aljunid, B. Chng, F. Huber, G. Maslennikov, and C. Kurtsiefer. Strong interaction between light and a single trapped atom without the need for a cavity. *Nature Physics*, 4(12):924–927, 2008.
- [61] L. Slodicka, G. Hetet, S. Gerber, M. Hennrich, and R. Blatt. Electromagnetically induced transparency from a single atom in free space. *Physical Review Letters*, 105(15):153604, 2010.
- [62] C. Schuck, F. Rohde, N. Piro, M. Almendros, J. Huwer, M. W. Mitchell, M. Hennrich, A. Haase, F. Dubin, and J. Eschner. Resonant interaction of a single atom with single photons from a down-conversion source. *Physical Review A*, 81(1):011802, 2010.
- [63] A. Blais, R.-S. Huang, A. Wallraff, S. M. Girvin, and R. J. Schoelkopf. Cavity quantum electrodynamics for superconducting electrical circuits: An architecture for quantum computation. *Physical Review A*, 69(6):062320, 2004.
- [64] A. Wallraff, D. I. Schuster, A. Blais, L. Frunzio, R.-S. Huang, J. Majer, S. Kumar, S. M. Girvin, and R. J. Schoelkopf. Strong coupling of a single photon to a superconducting qubit using circuit quantum electrodynamics. *Nature*, 431(7005):162–167, 2004.
- [65] I. Chiorescu, P. Bertet, K. Semba, Y. Nakamura, C. J. P. M. Harmans, and J. E. Mooij. Coherent dynamics of a flux qubit coupled to a harmonic oscillator. *Nature*, 431(7005):159–162, 2004.
- [66] J. Q. You and F. Nori. Atomic physics and quantum optics using superconducting circuits. *Nature*, 474(7353):589–597, 2011.
- [67] Y. Nakamura, Y. A. Pashkin, and J. S. Tsai. Coherent control of macroscopic quantum states in a single-cooper-pair box. *Nature*, 398(6730):786–788, 1999.
- [68] J. E. Mooij, T. P. Orlando, L. Levitov, L. Tian, C. H. van der Wal, and S. Lloyd. Josephson persistent-current qubit. *Science*, 285(5430):1036–1039, August 1999. PMID: 10446043.

- [69] Y. Yu, S. Y. Han, X. Chu, S.-I. Chu, and Z. Wang. Coherent temporal oscillations of macroscopic quantum states in a josephson junction. *Science*, 296(5569):889–892, 2002.
- [70] J. M. Martinis, S. Nam, J. Aumentado, and C. Urbina. Rabi oscillations in a large josephson-junction qubit. *Physical Review Letters*, 89(11):117901, 2002.
- [71] J. Koch, T. M. Yu, J. Gambetta, A. A. Houck, D. I. Schuster, J. Majer, A. Blais, M. H. Devoret, S. M. Girvin, and R. J. Schoelkopf. Charge-insensitive qubit design derived from the cooper pair box. *Physical Review A*, 76(4):042319, 2007.
- [72] H. Paik, D. I. Schuster, L. S. Bishop, G. Kirchmair, G. Catelani, A. P. Sears, B. R. Johnson, M. J. Reagor, L. Frunzio, L. I. Glazman, S. M. Girvin, M. H. Devoret, and R. J. Schoelkopf. Observation of high coherence in josephson junction qubits measured in a three-dimensional circuit QED architecture. *Physical Review Letters*, 107(24):240501, 2011.
- [73] V. E. Manucharyan, J. Koch, L. I. Glazman, and M. H. Devoret. Fluxonium: Single cooper-pair circuit free of charge offsets. *Science*, 326(5949):113–116, 2009.
- [74] J. H. Plantenberg, P. C. de Groot, C. J. P. M. Harmans, and J. E. Mooij. Demonstration of controlled-NOT quantum gates on a pair of superconducting quantum bits. *Nature*, 447(7146):836–839, 2007.
- [75] L. DiCarlo, J. M. Chow, J. M. Gambetta, Lev S. Bishop, B. R. Johnson, D. I. Schuster, J. Majer, A. Blais, L. Frunzio, S. M. Girvin, and R. J. Schoelkopf. Demonstration of two-qubit algorithms with a superconducting quantum processor. *Nature*, 460(7252):240–244, 2009.
- [76] T. Yamamoto, M. Neeley, E. Lucero, R. C. Bialczak, J. Kelly, M. Lenander, Matteo Mariantoni, A. D. O’Connell, D. Sank, H. Wang, M. Weides, J. Wenner, Y. Yin, A. N. Cleland, and J. M. Martinis. Quantum process tomography of two-qubit controlled-z and controlled-NOT gates using superconducting phase qubits. *Physical Review B*, 82(18):184515, 2010.
- [77] R. C. Bialczak, M. Ansmann, M. Hofheinz, E. Lucero, M. Neeley, A. D. O’Connell, D. Sank, H. Wang, J. Wenner, M. Steffen, A. N. Cleland, and J. M. Martinis. Quantum

- process tomography of a universal entangling gate implemented with josephson phase qubits. *Nature Physics*, 6(6):409–413, 2010.
- [78] M. R. Geller, E. J. Pritchett, A. Galiutdinov, and J. M. Martinis. Quantum logic with weakly coupled qubits. *Physical Review A*, 81(1):012320, 2010.
- [79] J. M. Fink, R. Bianchetti, M. Baur, M. Göppl, L. Steffen, S. Filipp, P. J. Leek, A. Blais, and A. Wallraff. Dressed collective qubit states and the tavis-cummings model in circuit QED. *Physical Review Letters*, 103(8):083601, 2009.
- [80] M. Neeley, R. C. Bialczak, M. Lenander, E. Lucero, M. Mariantoni, A. D. O’Connell, D. Sank, H. Wang, M. Weides, J. Wenner, Y. Yin, T. Yamamoto, A. N. Cleland, and J. M. Martinis. Generation of three-qubit entangled states using superconducting phase qubits. *Nature*, 467(7315):570–573, 2010.
- [81] L. DiCarlo, M. D. Reed, L. Sun, B. R. Johnson, J. M. Chow, J. M. Gambetta, L. Frunzio, S. M. Girvin, M. H. Devoret, and R. J. Schoelkopf. Preparation and measurement of three-qubit entanglement in a superconducting circuit. *Nature*, 467(7315):574–578, 2010.
- [82] M. Mariantoni, H. Wang, R. C. Bialczak, M. Lenander, E. Lucero, M. Neeley, A. D. O’Connell, D. Sank, M. Weides, J. Wenner, T. Yamamoto, Y. Yin, J. Zhao, J. M. Martinis, and A. N. Cleland. Photon shell game in three-resonator circuit quantum electrodynamics. *Nature Physics*, 7(4):287–293, 2011.
- [83] V. M. Stojanović, A. Fedorov, A. Wallraff, and C. Bruder. Quantum-control approach to realizing a toffoli gate in circuit QED. *Physical Review B*, 85(5):054504, 2012.
- [84] A. Fedorov, L. Steffen, M. Baur, M. P. da Silva, and A. Wallraff. Implementation of a toffoli gate with superconducting circuits. *Nature*, 481(7380):170–172, 2012.
- [85] M. D. Reed, L. DiCarlo, S. E. Nigg, L. Sun, L. Frunzio, S. M. Girvin, and R. J. Schoelkopf. Realization of three-qubit quantum error correction with superconducting circuits. *Nature*, 482(7385):382–385, 2012.

- [86] C. M. Wilson, G. Johansson, A. Pourkabirian, M. Simoen, J. R. Johansson, T. Duty, F. Nori, and P. Delsing. Observation of the dynamical casimir effect in a superconducting circuit. *Nature*, 479(7373):376–379, 2011.
- [87] C. Ciuti, G. Bastard, and I. Carusotto. Quantum vacuum properties of the intersubband cavity polariton field. *Physical Review B*, 72(11):115303, 2005.
- [88] J. Bourassa, J. M. Gambetta, A. A. Abdumalikov, O. Astafiev, Y. Nakamura, and A. Blais. Ultrastrong coupling regime of cavity QED with phase-biased flux qubits. *Physical Review A*, 80(3):032109, 2009.
- [89] T. Niemczyk, F. Deppe, H. Huebl, E. P. Menzel, F. Hocke, M. J. Schwarz, J. J. Garcia-Ripoll, D. Zueco, T. Hümmer, E. Solano, A. Marx, and R. Gross. Circuit quantum electrodynamics in the ultrastrong-coupling regime. *Nature Physics*, 6(10):772–776, 2010.
- [90] P. Forn-Díaz, J. Lisenfeld, D. Marcos, J. J. García-Ripoll, E. Solano, C. J. P. M. Harmans, and J. E. Mooij. Observation of the bloch-siegert shift in a qubit-oscillator system in the ultrastrong coupling regime. *Physical Review Letters*, 105(23):237001, 2010.
- [91] P. Nataf and C. Ciuti. Protected quantum computation with multiple resonators in ultrastrong coupling circuit QED. *Physical Review Letters*, 107(19):190402, 2011.
- [92] B. J. Smith and M. G. Raymer. Photon wave functions, wave-packet quantization of light, and coherence theory. *New Journal of Physics*, 9(11):414–414, 2007.
- [93] J. Garrison and R. Chiao. *Quantum Optics*. Oxford University Press, 2008.
- [94] M. O. Scully and M. S. Zubairy. *Quantum Optics*. Cambridge University Press, 1997.
- [95] K. J. Blow, R. Loudon, S. J. D. Phoenix, and T. J. Shepherd. Continuum fields in quantum optics. *Physical Review A*, 42(7):4102–4114, 1990.
- [96] R. Loudon. *The Quantum Theory of Light*. Oxford University Press, USA, 3rd edition, 2000.

- [97] A. W. Glaetzle, K. Hammerer, A. J. Daley, R. Blatt, and P. Zoller. A single trapped atom in front of an oscillating mirror. *Optics Communications*, 283(5):758–765, 2010.
- [98] P. Meystre and M. Sargent. *Elements of Quantum Optics*. Springer, 4th edition, 2007.
- [99] V. Weisskopf and E. Wigner. Berechnung der natrlichen linienbreite auf grund der diracschen lichttheorie. *Zeitschrift fr Physik A Hadrons and Nuclei*, 63(1):54–73, 1930.
- [100] P. W. Milonni. *The Quantum Vacuum: An Introduction to Quantum Electrodynamics*. Academic Press, 1 edition, 1993.
- [101] H. A. Bethe. The electromagnetic shift of energy levels. *Physical Review*, 72(4):339–341, August 1947.
- [102] C. Cohen-Tannoudji, J. Dupont-Roc, and G. Grynberg. *Atom-Photon Interactions*. Wiley-VCH, 2004.
- [103] A. Silberfarb and I. H. Deutsch. Entanglement generated between a single atom and a laser pulse. *Physical Review A*, 69(4):042308, 2004.
- [104] P. Domokos, P. Horak, and H. Ritsch. Quantum description of light-pulse scattering on a single atom in waveguides. *Physical Review A*, 65(3):033832, 2002.
- [105] N. Lindlein, R. Maiwald, H. Konermann, M. Sondermann, U. Peschel, and G. Leuchs. A new 4 geometry optimized for focusing on an atom with a dipole-like radiation pattern. *Laser Physics*, 17(7):927–934, 2007.
- [106] M. Sondermann, R. Maiwald, H. Konermann, N. Lindlein, U. Peschel, and G. Leuchs. Design of a mode converter for efficient light-atom coupling in free space. *Applied Physics B: Lasers and Optics*, 89(4):489–492, 2007.
- [107] M. K. Tey, G. Maslennikov, T. Liew, S. A. Aljunid, F. Huber, B. Chng, Z. Chen, V. Scarani, and C. Kurtsiefer. Interfacing light and single atoms with a lens. *New Journal of Physics*, 11(4):043011, 2009.
- [108] T. Legero, T. Wilk, A. Kuhn, and G. Rempe. Time-resolved two-photon quantum interference. *Applied Physics B: Lasers and Optics*, 77(8):797–802, 2003.

- [109] H. A. Bachor and T. C. Ralph. *A Guide to Experiments in Quantum Optics*. Wiley-VCH, 2nd edition, 2004.
- [110] S. A. Aljunid. *Interaction of a strongly focused light beam with single atoms*. PHD Thesis, 2012.
- [111] S. A. Aljunid, G. Maslennikov, Y. M. Wang, H. L. Dao, V. Scarani, and C. Kurtsiefer. Excitation of a single atom with exponentially rising light pulses. *In Preparation*, 2013.
- [112] N. Schlosser, G. Reymond, I. Protsenko, and P. Grangier. Sub-poissonian loading of single atoms in a microscopic dipole trap. *Nature*, 411(6841):1024–1027, 2001.
- [113] S. A. Aljunid, M. K. Tey, B. Chng, T. Liew, G. Maslennikov, V. Scarani, and C. Kurtsiefer. Phase shift of a weak coherent beam induced by a single atom. *Physical Review Letters*, 103(15):153601, 2009.
- [114] H. L. Dao, S. A. Aljunid, G. Maslennikov, and C. Kurtsiefer. Preparation of an exponentially rising optical pulse for efficient excitation of single atoms in free space. *Review of Scientific Instruments*, 83(8):083104, 2012.
- [115] U. Dorner and P. Zoller. Laser-driven atoms in half-cavities. *Physical Review A*, 66(2):023816, 2002.
- [116] G. Hetet, L. Slodicka, A. Glatzle, M. Hennrich, and R. Blatt. QED with a spherical mirror. *Physical Review A*, 82(6):063812, 2010.
- [117] K. F. Riley, M. P. Hobson, and S. J. Bence. *Mathematical Methods for Physics and Engineering: A Comprehensive Guide*. Cambridge University Press, 2nd edition, 2006.
- [118] J. Eschner, C. Raab, F. Schmidt-Kaler, and R. Blatt. Light interference from single atoms and their mirror images. *Nature*, 413(6855):495–498, 2001.
- [119] Y. Zhang, V. K. Komarala, C. Rodriguez, and M. Xiao. Controlling fluorescence intermittency of a single colloidal CdSe/ZnS quantum dot in a half cavity. *Physical Review B*, 78(24):241301, 2008.

- [120] D. E. Chang, A. S. Sørensen, E. A. Demler, and M. D. Lukin. A single-photon transistor using nanoscale surface plasmons. *Nature Physics*, 3(11):807–812, 2007.
- [121] K. P. Nayak and K. Hakuta. Single atoms on an optical nanofibre. *New Journal of Physics*, 10(5):053003, 2008.
- [122] G. Hétet, L. Slodička, M. Hennrich, and R. Blatt. Single atom as a mirror of an optical cavity. *Physical Review Letters*, 107(13):133002, 2011.
- [123] F. Dubin, D. Rotter, M. Mukherjee, C. Russo, J. Eschner, and R. Blatt. Photon correlation versus interference of single-atom fluorescence in a half-cavity. *Physical Review Letters*, 98(18):183003, 2007.
- [124] M. Sondermann, N. Lindlein, and G. Leuchs. Maximizing the electric field strength in the foci of high numerical aperture optics. *arXiv:0811.2098*, 2008.
- [125] A. Kuhn, M. Hennrich, and G. Rempe. Deterministic single-photon source for distributed quantum networking. *Physical Review Letters*, 89(6):067901, 2002.
- [126] A. A. Houck, D. I. Schuster, J. M. Gambetta, J. A. Schreier, B. R. Johnson, J. M. Chow, L. Frunzio, J. Majer, M. H. Devoret, S. M. Girvin, and R. J. Schoelkopf. Generating single microwave photons in a circuit. *Nature*, 449(7160):328–331, 2007.
- [127] A. A. Abdumalikov, O. Astafiev, A. M. Zagoskin, Yu. A. Pashkin, Y. Nakamura, and J. S. Tsai. Electromagnetically induced transparency on a single artificial atom. *Physical Review Letters*, 104(19):193601, 2010.
- [128] M. Hofheinz, E. M. Weig, M. Ansmann, R. C. Bialczak, E. Lucero, M. Neeley, A. D. O’Connell, H. Wang, J. M. Martinis, and A. N. Cleland. Generation of fock states in a superconducting quantum circuit. *Nature*, 454(7202):310–314, 2008.
- [129] M. Hofheinz, H. Wang, M. Ansmann, R. C. Bialczak, E. Lucero, M. Neeley, A. D. O’Connell, D. Sank, J. Wenner, J. M. Martinis, and A. N. Cleland. Synthesizing arbitrary quantum states in a superconducting resonator. *Nature*, 459(7246):546–549, 2009.

- [130] D. Marcos, M. Wubs, J. M. Taylor, R. Aguado, M. D. Lukin, and A. S. Sørensen. Coupling nitrogen-vacancy centers in diamond to superconducting flux qubits. *Physical Review Letters*, 105(21):210501, 2010.
- [131] D. I. Schuster, A. P. Sears, E. Ginossar, L. DiCarlo, L. Frunzio, J. J. L. Morton, H. Wu, G. A. D. Briggs, B. B. Buckley, D. D. Awschalom, and R. J. Schoelkopf. High-cooperativity coupling of electron-spin ensembles to superconducting cavities. *Physical Review Letters*, 105(14):140501, 2010.
- [132] H. Wu, R. E. George, J. H. Wesenberg, K. Mølmer, D. I. Schuster, R. J. Schoelkopf, K. M. Itoh, A. Ardavan, J. J. L. Morton, and G. A. D. Briggs. Storage of multiple coherent microwave excitations in an electron spin ensemble. *Physical Review Letters*, 105(14):140503, 2010.
- [133] M. Mariantoni, H. Wang, T. Yamamoto, M. Neeley, R. C. Bialczak, Y. Chen, M. Lenander, E. Lucero, A. D. OConnell, D. Sank, M. Weides, J. Wenner, Y. Yin, J. Zhao, A. N. Korotkov, A. N. Cleland, and J. M. Martinis. Implementing the quantum von neumann architecture with superconducting circuits. *Science*, 334(6052):61–65, 2011.
- [134] Y. Kubo, F. R. Ong, P. Bertet, D. Vion, V. Jacques, D. Zheng, A. Drau, J.-F. Roch, A. Auffeves, F. Jelezko, J. Wrachtrup, M. F. Barthe, P. Bergonzo, and D. Esteve. Strong coupling of a spin ensemble to a superconducting resonator. *Physical Review Letters*, 105(14):140502, 2010.
- [135] J. R. Johansson. *Quantum Mechanics in Superconducting Circuits and Nanomechanical Devices*. Applied Quantum Physics Laboratory, Chalmers University of Technology, 2009.
- [136] B. Yurke and J. S. Denker. Quantum network theory. *Physical Review A*, 29(3):1419–1437, 1984.
- [137] M. H. Devoret. Quantum fluctuations in electrical circuits. In *Les Houches Session LXIII, Quantum Fluctuations*, pages 351–386, 1995.
- [138] J. Bardeen, L. N. Cooper, and J. R. Schrieffer. Theory of superconductivity. *Physical Review*, 108(5):1175–1204, 1957.

- [139] M. Tinkham. *Introduction to Superconductivity: Second Edition (Dover Books on Physics)*. Dover Publications, 2nd edition, 2004.
- [140] B. D. Josephson. Possible new effects in superconductive tunnelling. *Physics Letters*, 1(7):251–253, 1962.
- [141] L. Tornberg and G. Johansson. Dispersive charge and flux qubit readout as a quantum measurement process. *Journal of Low Temperature Physics*, 146(1):227–252, 2007.
- [142] T. P. Orlando, J. E. Mooij, Lin Tian, Caspar H. van der Wal, L. S. Levitov, Seth Lloyd, and J. J. Mazo. Superconducting persistent-current qubit. *Physical Review B*, 60(22):15398–15413, December 1999.
- [143] P. Forn-Díaz and J. E. Mooij. Superconducting qubits and quantum resonators, 2010.
- [144] E. Purcell. Spontaneous emission probabilities at radio frequencies. *Physical Review*, 69(11):681–681, 1946.
- [145] P. Goy, J. M. Raimond, M. Gross, and S. Haroche. Observation of cavity-enhanced single-atom spontaneous emission. *Physical Review Letters*, 50(24):1903–1906, 1983.
- [146] D. Kleppner. Inhibited spontaneous emission. *Physical Review Letters*, 47(4):233–236, 1981.
- [147] G. Gúnter, A. A. Anappara, J. Hees, A. Sell, G. Biasiol, L. Sorba, S. De Liberato, C. Ciuti, A. Tredicucci, A. Leitenstorfer, and R. Huber. Sub-cycle switch-on of ultrastrong light-matter interaction. *Nature*, 458(7235):178–181, 2009.
- [148] A. T. Sornborger, A. N. Cleland, and M. R. Geller. Superconducting phase qubit coupled to a nanomechanical resonator: Beyond the rotating-wave approximation. *Physical Review A*, 70(5):052315, 2004.
- [149] A. A. Abdumalikov, O. Astafiev, Y. Nakamura, Y. A. Pashkin, and J. S. Tsai. Vacuum rabi splitting due to strong coupling of a flux qubit and a coplanar-waveguide resonator. *Physical Review B*, 78(18):180502, 2008.

- [150] B. Peropadre, P. Forn-Díaz, E. Solano, and J. J. García-Ripoll. Switchable ultrastrong coupling in circuit QED. *Physical Review Letters*, 105(2):023601, 2010.
- [151] J. Casanova, G. Romero, I. Lizuain, J. J. García-Ripoll, and E. Solano. Deep strong coupling regime of the jaynes-cummings model. *Physical Review Letters*, 105(26):263603, 2010.
- [152] D. Braak. Integrability of the rabi model. *Physical Review Letters*, 107(10):100401, 2011.
- [153] J. J. García-Ripoll, P. Zoller, and J. I. Cirac. Speed optimized two-qubit gates with laser coherent control techniques for ion trap quantum computing. *Physical Review Letters*, 91(15):157901, 2003.
- [154] J. J. García-Ripoll, P. Zoller, and J. I. Cirac. Coherent control of trapped ions using off-resonant lasers. *Physical Review A*, 71(6):062309, 2005.
- [155] W. C. Campbell, J. Mizrahi, Q. Quraishi, C. Senko, D. Hayes, D. Hucul, D. N. Matsukevich, P. Maunz, and C. Monroe. Ultrafast gates for single atomic qubits. *Physical Review Letters*, 105(9):090502, 2010.
- [156] G. Haack, F. Helmer, M. Mariani, F. Marquardt, and E. Solano. Resonant quantum gates in circuit quantum electrodynamics. *Physical Review B*, 82(2):024514, 2010.
- [157] D. Ballester, G. Romero, J. J. García-Ripoll, F. Deppe, and E. Solano. Quantum simulation of the ultrastrong-coupling dynamics in circuit quantum electrodynamics. *Physical Review X*, 2(2):021007, 2012.
- [158] G. Romero, D. Ballester, Y. M. Wang, V. Scarani, and E. Solano. Ultrafast quantum gates in circuit QED. *Physical Review Letters*, 108(12):120501, 2012.
- [159] R. Bianchetti, S. Filipp, M. Baur, J. M. Fink, C. Lang, L. Steffen, M. Boissonneault, A. Blais, and A. Wallraff. Control and tomography of a three level superconducting artificial atom. *Physical Review Letters*, 105(22):223601, 2010.
- [160] R. N. Simons. *Coplanar Waveguide Circuits Components & Systems*. Wiley-IEEE Press, 2001.

-
- [161] M. Göppl, A. Fragner, M. Baur, R. Bianchetti, S. Filipp, J. M. Fink, P. J. Leek, G. Puebla, L. Steffen, and A. Wallraff. Coplanar waveguide resonators for circuit quantum electrodynamics. *Journal of Applied Physics*, 104(11):113904–113904–8, 2008.
- [162] K. Watanabe, K. Yoshida, T. Aoki, and S. Kohjiro. Kinetic inductance of superconducting coplanar waveguides. *Japanese Journal of Applied Physics*, 33:5708–5712, 1994.
- [163] Y. D. Wang, P. Zhang, D. L. Zhou, and C. P. Sun. Fast entanglement of two charge-phase qubits through nonadiabatic coupling to a large josephson junction. *Physical Review B*, 70(22):224515, 2004.
- [164] M. Mariani, F. Deppe, A. Marx, R. Gross, F. K. Wilhelm, and E. Solano. Two-resonator circuit quantum electrodynamics: A superconducting quantum switch. *Physical Review B*, 78(10):104508, 2008.

List of Publications

- [1] Syed Abdullah Aljunid, Gleb Maslennikov, **Yimin Wang**, Dao Hoang Lan, Valerio Scarani, and Christian Kurtsiefer, *Excitation of a single atom with exponentially rising light pulses*, arXiv:1304.3761 (2013).
- [2] **Yimin Wang**, Jiří Minář, and Valerio Scarani, , *State-dependent atomic excitation by multiphoton pulses propagating along two spatial modes*, Phys. Rev. A, **86**, 023811 (2012).
- [3] G. Romero, D. Ballester, **Yimin Wang**, V. Scarani, and E. Solano, *Ultrafast Quantum Gates in Circuit QED*, Phys. Rev. Lett., **108**, 120501 (2012).
- [4] **Yimin Wang**, D. Ballester, G. Romero, V. Scarani, and E. Solano, *Validity of resonant two-qubit gates in the ultrastrong coupling regime of circuit quantum electrodynamics*, Physica Scripta, **T147**, 014031 (2012).
- [5] **Yimin Wang**, Jiří Minář, Gabriel Hétet, and Valerio Scarani, *Quantum memory with a single two-level atom in a half cavity*, Phys. Rev. A, **85**, 013823 (2012).
- [6] **Yimin Wang**, Jiří Minář, Lana Sheridan, and Valerio Scarani, *Efficient excitation of a two-level atom by a single photon in a propagating mode*, Phys. Rev. A, **83**, 063842 (2011).
- [7] Yan-Li Zhou, **Yimin Wang**, Linmei Liang, and Chengzu Li, *Quantum state transfer between distant nodes of a quantum network via adiabatic passage*, Phys. Rev. A, **79**, 044304 (2009).